AQUIFER CONTAMINANT SOURCE ZONE
CHARACTERIZATION WITH PARTITIONING TRACERS AND
REMEDIATION WITH SINGLE-PHASE MICROEMULSION FLUSHING

By

JAMES WILLIAM JAWITZ

A DISSERTATION PRESENTED TO THE GRADUATE SCHOOL
OF THE UNIVERSITY OF FLORIDA IN PARTIAL FULFILLMENT
OF THE REQUIREMENTS FOR THE DEGREE OF
DOCTOR OF PHILOSOPHY

UNIVERSITY OF FLORIDA

1999

ACKNOWLEDGMENTS

Primary thanks for guiding me to this point go to my advisory committee chair and co-chair, Drs. Michael Annable and Suresh Rao, both of whom have provided me with inspiration and opportunity in all avenues of academic inquiry. I also thank my other committee members–Drs. Dean Rhue, Kirk Hatfield and William Wise–for their substantial contributions to this endeavor.

The particle tracking simulation results described in Chapter 2 were provided by George Demmy. Our daily discussions were inspirational for much of this work.

The field study described in Chapter 3 benefitted from the contributions of many students, professors, and U.S. EPA personnel. However, I wish to specifically acknowledge the invaluable assistance of Dr. Randall K. Sillan. Also, Gloria Sillan, Bill Reve, and Drs. Dongping Dai, Heonki Kim, Meifang Zhou, and Dean Rhue performed virtually all of the laboratory analyses associated with the field study; none of this work would have been possible without their efforts.

Lastly, I thank my mother and father for their pride and support.

TABLE OF CONTENTS

v

LIST OF TABLES

LIST OF FIGURES

AQUIFER CONTAMINANT SOURCE ZONE
CHARACTERIZATION WITH PARTITIONING TRACERS AND
REMEDIATION WITH SINGLE-PHASE MICROEMULSION FLUSHING

By

James William Jawitz

August 1999

Chairperson: Michael D. Annable
Co-chairperson: P. Suresh C. Rao
Major Department: Environmental Engineering Sciences

Two fundamental issues related to the remediation of aquifers contaminated with nonaqueous phase liquids (NAPLs) are addressed. First, the difficulty of ascertaining the amount and spatial distribution of the contaminants at a given site has been a limiting factor in the cleanup of many sites. Here, a technique is presented for the estimation of NAPL spatial distributions using the higher moments of partitioning tracer breakthrough curves (BTCs) measured at a single well or monitoring location. The method is validated with numerical simulations and further evaluated with laboratory and field experimental data.

A second constraint on the cleanup of contaminated sites has been the absence of technologies which have been proven to effectively and efficiently remove NAPL contaminants from the subsurface. Here, the results of a field test at Hill Air Force Base,

Utah, are described wherein a Winsor Type I surfactant/alcohol mixture was used as an in situ flushing agent to solubilize a multi-component non-aqueous phase liquid (NAPL) as a single-phase microemulsion (SPME). The surfactant (polyoxyethylene (10) oleyl ether) and alcohol (*n*-pentanol) together comprised 5.5 percent by weight of the flushing solution. The NAPL was extremely complex, containing more than 200 constituents and a 'pitch' fraction which was not solvent-extractable. The NAPL removal effectiveness of the SPME flood is evaluated here using information from soil cores, partitioning tracer tests, and NAPL constituent breakthrough curves (BTCs) measured at extraction wells and multilevel samplers. Quantitative measures of remediation efficiency are developed for each of these characterization methods and the efficiency of the SPME flood is determined for each. In addition, the remediation efficiency of an alcohol flushing study, conducted earlier under similar conditions, was determined using the same measures. The remediation efficiencies of both studies were comparable, removing relatively insoluble contaminants 10^6 times more efficiently than would have been expected for pump-and-treat.

Finally, the effect of rate-limited NAPL microemulsification is investigated through field-scale flow interruption techniques, correlations between NAPL remediation efficiency and local flux, and numerical simulations. The field data show evidence of mass-transfer rate limitations, but also suggest that these effects were relatively localized. Numerical modeling of laboratory and field data from both the alcohol and SPME flushing studies indicates that microemulsification is less subject to rate-limitations than cosolvent-enhanced solubilization of a complex NAPL.

CHAPTER 1
INTRODUCTION

A major impediment to the remediation of aquifers contaminated with nonaqueous

phase liquid (NAPL) wastes has been the difficulty of ascertaining the amount and spatial

distribution of the contaminants at a given site. An additional constraint on the cleanup of

contaminated sites has been the absence of technologies which have been proven to

effectively and efficiently remove NAPL contaminants from the subsurface. Thus, the focus

of this work is on the dual problems of contaminated aquifer characterization and

remediation.

Aquifer Contaminant Source Zone Characterization

Interwell partitioning tracers have been used at both the laboratory and field scales

to detect and quantify residual NAPL contaminants in the subsurface (Jin et al., 1995; Nelson

and Brusseau, 1996; Annable et al., 1998a, b). To date, however, the interpretation of

partitioning tracer data has been restricted to first temporal moment analyses for the

characterization of average NAPL saturations. The determination of the spatial distribution

of the NAPL mass within the flow domain has required partitioning tracer characterization

at multiple sampling locations. For example, Sillan et al. (1998) used partitioning tracer data

1

collected from a network of multilevel samplers to create NAPL spatial distribution maps at a field site both before and after cosolvent flushing.

In Chapter 2, a method is described for the use of partitioning tracers and the method of moments to characterize the spatial distribution of NAPL contaminants in porous media using only one sampling location. In this approach, it is assumed that some fraction of the streamlines within a domain are uncontaminated and that the NAPL saturation in the remainder of the streamlines can be represented either as a homogeneous value, or as a distribution of saturations. Equations are derived that facilitate the description of the NAPL spatial distribution based on the temporal moments of tracer breakthrough curves. Numerical simulations were conducted both to validate the equations and to demonstrate their utility. The numerical simulations were also used to investigate the impact of a correlation between NAPL saturation and media properties, and how these correlations may affect our ability to describe the NAPL saturation distribution. The method was then applied to controlled laboratory experiments and two recent field-scale tracer tests. The NAPL distributions that were predicted from the field data were compared to information gleaned from more traditional methods (i.e., soil cores).

Aquifer Contaminant Source Zone Remediation

Many investigators have recently demonstrated that in situ flushing techniques show promise for the remediation of aquifers contaminated with NAPLs such as fuels and chlorinated solvents in time frames much smaller than would be expected for traditional pump-and-treat methods (Falta et al., 1996; Fountain et al., 1996; Rao et al., 1997). Similar

to enhanced oil recovery (EOR) (e.g., Shah, 1981; Lake, 1989), these flushing technologies generally involve the addition of chemical agents to an injection fluid during either miscible or immiscible displacements to accelerate the dissolution or displacement of NAPLs from contaminated aquifers. Two classes of chemical agents used for in situ flushing which have been the focus of much study are cosolvents (Peters and Luthy, 1993; Brandes and Farley, 1993; Augustijn et al., 1994; Imhoff et al., 1995) and surfactants (Abdul et al., 1992; West and Harwell, 1992; Pennell et al., 1993; Fountain et al., 1996; Shiau et al., 1996).

Both cosolvent and surfactant solutions can be used to accelerate the removal of residually-trapped NAPLs from porous media through either mobilization or enhanced solubilization. Mobilization of NAPL trapped within the porous media by capillary forces is facilitated by a reduction in the interfacial tension between the NAPL and the flushing solution as either a cosolvent or surfactant solution displaces the resident groundwater and contacts NAPL ganglia. Similarly, solubilization of the NAPL is enhanced due to the reduced polarity of the flushing solution, compared to that of the resident groundwater.

Several laboratory and field studies on NAPL mobilization have shown that a large percentage of the NAPL trapped in contaminated porous media, often > 95%, can be removed after injecting a small number of pore volumes of flushing fluid (Pennell et al., 1996; Sabatini et al., 1996). However, mobilization technologies are limited to sites where the flow of the mobilized NAPL can be controlled and the potential for migration of NAPL through layers that previously acted as capillary barriers can be assured. Remediation technologies which rely on solubilization generally do not remove the NAPL as efficiently as mobilization technologies. However, solubilization technologies generally pose less risk

with regard to uncontrolled migration of the mobilized NAPLs and are less complex to design, particularly with regard to the number of parameters requiring optimization. It is for these reasons that the focus of researchers at the University of Florida (UF) has been on developing aquifer remediation strategies which solubilize NAPLs without inducing mobilization (Rao et al., 1991; Augustijn et al., 1994; Ouyang et al., 1996; Rhue et al., 1999).

In Chapter 3, the results are reported from a field-scale, in situ flushing aquifer remediation study conducted within a surficial aquifer contaminated with a complex NAPL waste mixture, wherein NAPL solubilization without mobilization was the goal. This study was one of eight pilot-scale tests funded by the Strategic Environmental Research and Development Program (SERDP) and the Advanced Applied Technology Demonstration Facility (AATDF), and conducted side-by-side at Hill Air Force Base (AFB), Utah, for the purpose of evaluating in situ flushing remediation technologies for the removal of NAPLs from subsurface environments. In 1995, UF and the U.S. Environmental Protection Agency (EPA) conducted a field-scale evaluation of in situ cosolvent flushing within the same contaminant source zone at Hill AFB (Rao et al., 1997; Annable et al., 1998b; Sillan et al., 1998), wherein the flushing solution (70% ethanol, 12% *n*-pentanol, and 18% water by volume) was designed to solubilize the NAPL. In this second solubilization study, the objective was to achieve high NAPL solubilization efficiencies with a lower concentration of chemical additives in the flushing solution than was required in the cosolvent flushing experiment. A surfactant/alcohol mixture was used to generate a Winsor Type I system, where the NAPL was solubilized and transported as a single-phase microemulsion (SPME).

For the SPME process, only 5.5 wt % of the flushing solution was comprised of chemical additives.

The SPME flushing study was conducted in a hydraulically-isolated test cell (2.8 m × 4.6 m), similar in design to that described by Rao et al. (1997). The amount and spatial distribution of residual NAPL within the test cell were determined both before and after SPME flushing using soil cores and interwell partitioning tracer tests. Also, fluid samples collected from extraction wells and multilevel samplers at regular intervals during the SPME flood were analyzed for target NAPL constituents. Each of these data sets was used to evaluate the performance of the SPME flushing experiment in terms of both the NAPL removal effectiveness, defined as the fraction of the initial amount of contaminants present that was removed by the remediation technology, and the NAPL removal efficiency, defined as the amount of NAPL removed divided by a measure of the volume of flushing fluid applied. Also, the performance of the SPME flood was compared to that of the 1995 cosolvent flood using the same performance measures.

In Chapter 4, the impact of rate-limited mass transfer on both the cosolvent and SPME flushing studies was investigated. Nonequilibrium effects observed during NAPL dissolution generally result from diffusion caused by either large-scale heterogeneities in media properties and NAPL distribution or local-scale mass transfer constraints. At local scales, mass transfer across fluid-solid or fluid-fluid interfaces within porous media is often diffusion-limited. At larger scales, hydraulic conductivity variability results in heterogeneous pore water velocity distributions. High-velocity streamlines are likely to exhibit lower solute concentrations than low-velocity streamlines because of rate-limited

mass transfer. Solute concentrations will similarly vary among streamlines that contain either different amounts of NAPL, or NAPLs of different compositions. All of these factors contribute to solute concentration gradients between streamlines, which result in solute diffusion. These diffusion effects are mechanistically similar to those described for rate-limited sorption processes (e.g., Brusseau et al., 1991). Augustijn (1993) noted that aqueous dissolution of multi-component NAPLs can be modeled as desorption because both processes involve solute diffusion through an organic phase (NAPLs for dissolution and soil organic matter for desorption). Large-scale diffusion limitations are also equivalent for both process. Augustijn (1993) also noted that the similarity between dissolution and desorption is particularly acute when the NAPL contains a substantial fraction of insoluble pitch, as was the case for both the coal tar examined by Augustijn and the Hill AFB NAPL.

In Chapter 4, the one-dimensional flow, cosolvent-enhanced desorption code of Augustijn et al. (1994) was adapted to model both cosolvent-enhanced dissolution and single-phase microemulsification of NAPLs. This model was applied to both laboratory and field data from both the cosolvent and SPME flushing studies. Transport of the flushing agents was described with a one-dimensional advection-dispersion equation. For the field experiment simulations, the superposition of two solute transport equations was used to characterize the more complex heterogeneities encountered at the field scale. Nonequilibrium dissolution/desorption was described using the bicontinuum approach, wherein a fraction of the dissolution/desorption occurs instantaneously, and the remainder is characterized by a first-order mass transfer model.

Finally, it should be noted that preliminary, or less comprehensive, versions of some of the material presented here have been published elsewhere: a preliminary version of the homogeneous binary NAPL distribution model in Chapter 2 can be found in Jawitz et al. (1998b), the NAPL removal effectiveness of the SPME flood, detailed in Chapter 3, was presented in a more limited form in Jawitz et al. (1998c), the control-plane approach to characterizing the performance of the cosolvent and SPME field studies was described in Jawitz et al. (1999), and the NAPL removal efficiency measures defined in Chapter 3 were presented in Jawitz et al. (1997b).

CHAPTER 2
CHARACTERIZATION OF THE SPATIAL DISTRIBUTION OF AQUIFER -
CONTAMINANTS USING PARTITIONING TRACER HIGHER MOMENTS

A method is described for the use of partitioning tracer breakthrough curve moments to characterize the spatial distribution of NAPL contaminants within the swept volume of a given sampling location. The approach is based on a binary model, wherein contaminated and uncontaminated fractions of the swept zone are distinguished. Two models based upon this approach are presented below: (1) the homogeneous binary model in which the NAPL saturation within the contaminated zone is assumed to be homogeneous, and (2) the distributed binary model in which the contaminated zone is characterized by a distribution of NAPL saturations (the lognormal distribution is used here). The applicability of both models is explored using numerical simulations as well as laboratory and field experiments.

Background Theory

Transport Models

Equilibrium advection-dispersion equation. Solute transport through porous media can be described as an advective-dispersive process wherein solutes are advected at the average porewater velocity, v, and the variability in velocities through different sized pores is described by a dispersion coefficient, D. The partial differential equation governing this

process during one-dimensional, saturated, steady flow is known as the advection-dispersion equation (ADE) and is commonly written as follows:

$$R \frac{\partial c}{\partial t} = D \frac{\partial^2 c}{\partial x^2} - v \frac{\partial c}{\partial x} \qquad (2\text{-}1)$$

where t is time, x is distance, c is the aqueous solute concentration, and R is the retardation factor for an instantaneously absorbed solute following a linear isotherm. For a partitioning tracer, the retardation is a function of the average NAPL saturation in the system, S_N, and the NAPL-water partitioning coefficient, K_N (Jin et al, 1995):

$$R = 1 + \frac{K_N S_N}{1 - S_N} \qquad (2\text{-}2)$$

The retardation factor is determined from the ratio of the mean arrival times of the partitioning tracer, t_p, and the nonpartitioning tracer, t_{np}, both corrected for the solute pulse injection duration, t_0:

$$R = \frac{t_p - \dfrac{t_0}{2}}{t_{np} - \dfrac{t_0}{2}} \qquad (2\text{-}3)$$

Equation 2-1 can be simplified to the following nondimensional form:

$$R \frac{\partial C}{\partial T} = \frac{1}{P} \frac{\partial^2 C}{\partial X^2} - \frac{\partial C}{\partial X} \qquad (2\text{-}4)$$

where the following dimensionless variables are defined:

$$P = \frac{vL}{D} \tag{2-5}$$

$$T = \frac{vt}{L} \tag{2-6}$$

$$X = \frac{x}{L} \tag{2-7}$$

$$C = \frac{c}{c_0} \tag{2-8}$$

where P is the Peclet number, L is the system length, T is the number of pore volumes (PV), and c_0 is the solute input concentration.

Nonequilibrium advection-dispersion equation. When solute sorption, or partitioning, is kinetic rather than instantaneous, a nonequilibrium transport model is required. The nonequilibrium model used here is the two-site model where solute partitioning is assumed to be instantaneous into some fraction of the NAPL, F, and kinetically limited by a first-order process into the remaining fraction. Nkedi-Kizza et al. (1984) demonstrated that this model is mathematically equivalent to the two-region model, wherein the nonequilibrium transport is caused by rate-limited mass transfer between a mobile and immobile zone. The governing partial differential equations for the two-site model can be written in dimensionless form as follows:

$$\beta R \frac{\partial C_1}{\partial T} + \frac{\partial C_2}{\partial T} = \frac{1}{P} \frac{\partial^2 C_1}{\partial X^2} - \frac{\partial C_1}{\partial X} \tag{2-9}$$

$$\frac{\partial C_2}{\partial T} = \omega\big[(1 - F)(R - 1)C_1 - C_2\big] \tag{2-10}$$

where the subscripts 1 and 2 refer to the instantaneous and rate-limited fractions, respectively, and

$$R_1 = 1 + \frac{F K_N S_N}{1 - S_N} \tag{2-11}$$

$$\beta = \frac{R_1}{R} \tag{2-12}$$

$$\omega = \frac{k_2 L}{v} \tag{2-13}$$

where k_2 is a first-order kinetic rate coefficient. Note that this form of the two-site nonequilibrium model, adapted from Augustijn et al. (1994), differs from the more commonly presented versions (e.g., Nkedi-Kizza et al., 1984; Valocchi, 1985) in that the Damkohler number, ω, is independent of β and R.

Lognormal distribution (transfer function approach). Jury (1982) proposed modeling solute breakthrough curves (BTCs) as lognormal travel time distributions as an alternative to the ADE. An advantage of this strategy is that parameters affecting solute travel time can be estimated without the constraint of describing the transport processes. A lognormal random variable X is one for which $Y = \ln X$ is normally distributed with mean μ and standard deviation σ. If solute arrival time, t, is considered as a random variable, then the

lognormal probability density function (PDF), $f(t)$, for a pulse input of duration t_0 is described by the following equation:

$$f(t) = \frac{t_0}{\sqrt{2\pi}\,\sigma t} \exp\left(-\frac{(\ln(t) - \mu)^2}{2\sigma^2} \right)$$
(2-14)

Method of Moments

The method of moments is an effective technique for determining model parameters from measured data. The Nth temporal moment, m_N, of a distribution, $f(t)$, is defined:

$$m_N = \int_0^\infty t^N f(t)\, dt$$
(2-15)

The absolute moments of measured BTCs are calculated by replacing $f(t)$ in (2-15) with measured solute concentration values, $C(t)$. Normalized moments are Nth absolute moments scaled to the zeroth moment. Model parameters are determined by equating measured moments, determined through numerical integration of measured data (e.g., Haas, 1996), with derived moment expressions, generating a system of N equations that can be solved for N model parameters. The first three pulse-corrected, normalized temporal moment equations for the equilibrium ADE, nonequilibrium ADE, and lognormal distribution models are presented in Table 2-1 (adapted from Valocchi, 1985; Helms et al., 1999; and Aitchison and Brown, 1957). The dimensionless units of these moment equations, m_N, are PV^N.

Table 2-1. Normalized, pulse-corrected temporal moment equations for equilibrium ADE, nonequilibrium ADE, and lognormal models.

Moment	ADE[1]	Nonequilibrium ADE[1]	Lognormal[2]
m_1	$XR + \dfrac{t_0}{2}$	$XR + \dfrac{t_0}{2}$	$\exp\!\left(\mu + \dfrac{\sigma^2}{2}\right)$
m_2	$\dfrac{2XR^2}{P} + m_1^2 + \dfrac{t_0^2}{12}$	$\dfrac{2XR^2}{P} + \dfrac{2X(1-\beta)^2 R^2}{\omega} + m_1^2 + \dfrac{t_0^2}{12}$	$\exp(2\mu + 2\sigma^2)$
m_3	$\dfrac{12XR^3}{P^2} + 3m_1 m_2 - 2m_1^3$	$\dfrac{12XR^3}{P^2} + \dfrac{12X(1-\beta)^2 R^3}{P\omega} + \dfrac{6X(1-\beta)^3 R^3}{\omega^2} + 3m_1 m_2 - 2m_1^3$	$\exp\!\left(3\mu + \dfrac{9}{2}\sigma^2\right)$

[1] Adapted from Valocchi (1985) and Helms et al. (1999)
[2] Aitchison and Brown (1957)

NAPL Distribution Models

Excess Spreading of Tracer BTCs

Consider the two-dimensional porous medium of Figure 2-1a, wherein the entire domain is contaminated with NAPL at a homogeneous saturation. The media properties, such as porosity, η, and intrinsic permeability, k, are not necessarily homogeneous, but are assumed to be stationary (i.e., the statistics describing the variability of these properties are constant in space). A BTC measured from the transport of a nonpartitioning tracer through the domain will exhibit some degree of spreading, characterized by the second moment, that is representative of the degree of heterogeneity of the media. The transport of a partitioning tracer through the same domain will be retarded according to (2-2) and the measured BTC will exhibit a greater degree of spreading than that of the nonpartitioning tracer. Assuming that transport is adequately described by the ADE and that partitioning is both instantaneous and linear, the partitioning tracer second moment, m_2^p, can be expressed in terms of the nonpartitioning tracer second moment, m_2^{np}, and R (see Table 2-1). Any BTC spreading beyond that expected based on m_2^{np} and R can be considered as 'excess' spreading.

A nonhomogeneous NAPL distribution can contribute to excess spreading of a partitioning tracer BTC that is manifested in the higher moments (i.e., $N > 1$). Here, the nonpartitioning and partitioning tracer moments are used to infer the NAPL spatial distribution based on the concept of excess spreading. However, the following factors can also lead to excess spreading of a partitioning tracer BTC: nonequilibrium partitioning,
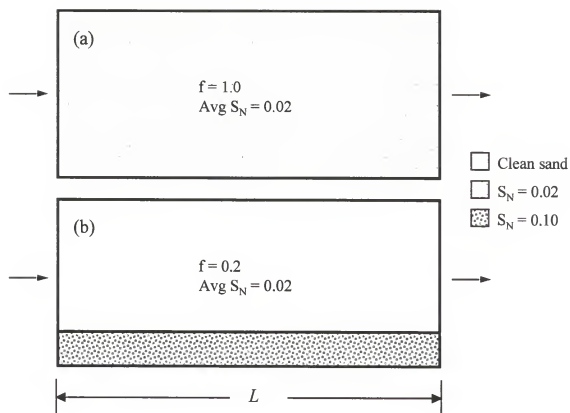
Figure 2-1. Schematic representation of a two-dimensional domain with (a) uniformly distributed NAPL, and (b) the same volume of NAPL distributed over only 20% of the domain.

nonlinear partitioning and a correlation between S_N and hydraulic conductivity, K. The applicability of each of these factors is discussed below.

Nonequilibrium partitioning. The effects of nonequilibrium sorption, or partitioning, on tracer higher moments were described by Valocchi (1985). Inspection of the nonequilibrium ADE moment equations in Table 2-1 reveals that nonequilibrium effects lead to enhanced spreading (i.e., larger second and third moments) relative to equilibrium conditions. Jin et al. (1995) found that pore water velocities of 0.5 to 1.5 m/d were slow enough to approximate equilibrium conditions for partitioning of alcohol tracers into tetrachloroethylene. The models developed here are based on the assumption that partitioning tracer residence times are sufficient to ensure equilibrium partitioning. However, the velocities suggested by Jin et al. (1995) are quite low and may be impractical for field-scale experiments. Thus, the impact of using higher velocities was investigated in the laboratory experiments reported below.

Nonlinear partitioning. Wise et al. (1999) demonstrated that the partitioning of alcohol tracers into NAPLs is nonlinear over broad concentration ranges. Wise (1999) provided an example case of an alcohol tracer partitioning into TCE and calculated the expected partitioning tracer first moment for different degrees of isotherm nonlinearity, demonstrating that significant errors may result from assuming linear partitioning. Because of the exponential nature of higher moments (see Equation 2-15), the errors for higher moments will be proportionately higher. However, Wise et al. (1999) demonstrated that the common practice of using a suite of partitioning tracers (e.g., Jin et al., 1995; Annable et al., 1998) may cause the partitioning behavior to approach linearity. Also, Wise (1999)

suggested that consideration of isotherm linearity should be made during tracer selection and that by using low tracer injection concentrations, nonlinear effects can be minimized. Thus, for this work linear partitioning was assumed. The effect of varying tracer injection concentrations, and thus, the degree of nonlinearity, was investigated in the laboratory experiments described below.

Correlation between S_N and K. Many investigators have studied the effects of a correlation between hydraulic conductivity, or media permeability, and sorption coefficient, K_d, on solute transport through the use of numerical or analytical models (Valocchi, 1989; Cvetkovic and Shapiro, 1990; Robin et al., 1991; Bellin et al., 1993; Tompson, 1993). Because the sorption coefficient is related to the amount of organic matter present (e.g., Schwarzenbach et al., 1993), K_d will here be considered to be analogous to S_N. All of the studies cited above have shown that a negative correlation between K_d and K leads to enhanced spreading relative to the uncorrelated case, while a positive correlation leads to less spreading. For the negatively correlated case, reactive tracers traveling along low velocity (i.e., low permeability) streamlines will experience high K_d values and be more retarded, leading to longer travel times and more-elongated BTCs. For the positively correlated case, reactive solutes traveling along high velocity streamlines will be more highly retarded, allowing the solutes traveling along the low velocity, and low retardation, streamlines to catch up, resulting in more-compressed BTCs.

Similar effects would be expected for correlations between S_N and K, however, little experimental evidence exists to support a general model for a correlation between these parameters. Intuitive arguments can be made for both positive and negative correlations.

For example, following a contamination event at the surface, NAPLs migrate downwards due to gravitational forces and NAPL ganglia become trapped in the pore spaces by capillary forces. Large-pore, and thus high conductivity, portions of the media will likely have lower amounts of trapped NAPL than smaller-pore portions (e.g., Powers et al., 1992), indicating a negative correlation between S_N and K. However, as migrating NAPLs encounter low-permeability regions, high entry pressures prevent NAPLs from entering very small pore spaces, resulting in the accumulation of NAPLs as thin lenses or pools on top of low permeability zones at many sites (e.g., Frind and Keuper, 1991). Thus, low permeability zones would exhibit the lowest NAPL saturations, indicating a positive correlation between S_N and K. These conflicting arguments allude to the complex nature of the distribution of NAPLs in the subsurface, and the inadequacy of a simple model for the presumption of a correlation between S_N and K.

Also, because media properties and model parameters are often inferred from tracer arrival time distributions (i.e., BTCs), as will be done here, any correlation between S_N and K may be of secondary importance to the correlation between S_N and nonpartitioning tracer travel time. The specific discharge, q, through a one-dimensional porous medium is described by Darcy's law:

$$q = -K \frac{dh}{dx} \tag{2-16}$$

where

$$q = \frac{Q}{A} = v\eta \tag{2-17}$$

and h is the hydraulic head, Q is the fluid flow rate, A is the media cross-sectional area, and η is the media porosity. Nonpartitioning solute travel time is inversely proportional to the average velocity:

$$t = \frac{L}{v} \tag{2-18}$$

Therefore, travel time and K can be related by combining (2-16)-(2-18) and integrating:

$$t = -\frac{L^2 \eta}{K_m(h_{x=L} - h_{x=0})} \tag{2-19}$$

where K_m is representative of the mean hydraulic conductivity along the streamline. If L, η, and h are assumed to be equal for each streamline, then the solute arrival time, t, for a given streamline is strictly inversely proportional to K. Correlations between S_N and K can then be transformed to correlations between S_N and t. However, for three dimensional, heterogeneous fields, L is not likely to be equal for each streamline. Also, for domains that are more complex than simple linear flow systems, solute travel time may be affected by other factors. In doublet well patterns, for example, a wide distribution of streamline lengths is produced by the flow system geometry even in homogeneous media, and solute travel times and hydraulic conductivity are not directly proportional. Therefore, any correlations that may exist between S_N and K may be only weakly manifested in measured BTCs.

However, for comparison with the extensive literature on the correlation between K_d and K, moment equations were derived that account for correlations between S_N and nonpartitioning solute travel time. Correlations between S_N and K were included in the

numerical simulations presented below and the effect of these correlations on solute travel times is discussed.

<u>Binary Model Framework and Assumptions</u>

Consider a two-dimensional domain wherein a fraction, f, of the total number of streamtubes in the domain are contaminated with NAPL at an average saturation S_N (Figure 2-1b). A tracer BTC representing transport through the entire domain, T, can be obtained through the superposition of BTCs representing transport through the contaminated and uncontaminated fractions of the domain. The normalized moments of a tracer BTC from T can be similarly obtained through superposition of the normalized moments of BTCs from both portions of the domain:

$$m_{N_T} = (1 - f)m_{N_{uc}} + fm_{N_c} \qquad (2\text{-}20)$$

where the subscripts uc and c refer to the uncontaminated and contaminated fractions, respectively.

Note that because BTCs measured at extraction wells are flux-averaged, f in (2-20) represents the flux-averaged contaminated fraction of the domain. However, it is the volume-averaged contaminated fraction that is likely to be of more interest to contaminant hydrologists. If the porous media properties are assumed to be stationary, as will be done here, the mean permeabilities in the contaminated and uncontaminated fractions will be equivalent and the flux through each zone will be related to f. Thus, for stationary fields, f is representative of both the flux-averaged and volume-averaged contaminated fractions.

Two binary models of NAPL distribution are explored here: (1) the homogeneous binary model, wherein a fraction of the streamtubes are assumed to be homogeneously contaminated, and (2) the distributed binary model, wherein the streamtubes within the contaminated fraction are characterized by a distribution of NAPL saturations. The binary approach is advantageous because tracer test swept volumes may include relatively large portions of an aquifer that do not contain NAPL. The ability to differentiate these zones is important for the design of efficient remediation strategies.

Effect of NAPL on media properties. Because the media properties are assumed to be stationary, the only difference between the contaminated and uncontaminated zones is the presence of the NAPL. Partitioning into the NAPL will cause the transport of a partitioning tracer through the contaminated zone to be retarded relative to the uncontaminated zone, but nonpartitioning tracer transport should be unretarded in both zones (assuming no adsorption to the media). However, the transport behavior of a nonpartitioning tracer through the two zones may differ in other ways because of the effects of the NAPL on media permeability and porosity. The nature of these effects may be influenced by the wetting characteristics of the NAPL.

Non-wetting phase contaminants present at saturations below the residual saturation are generally trapped by capillary forces and exist as discontinuous ganglia residing in the pore spaces between media particles. The presence of these ganglia result in reductions in the effective porosity and permeability of the media, as described by the following relationships:

$$\eta_e = \eta \, (1 - S_N) \tag{2-21}$$

$$k_e = k \, (1 - S_N)^{\zeta} \tag{2-22}$$

where ζ is an empirically determined constant with values reported between 3 and 4 (Corey, 1986) and the subscript e indicates an effective, rather than intrinsic, media property. At saturations above residual, the non-wetting phase becomes locally continuous and may be free-flowing. These higher-saturation cases (e.g., NAPL pools) will not be considered here.

Hydraulic conductivity and media permeability are related as follows:

$$K = \frac{k \rho_w g}{\mu_w} \tag{2-23}$$

where ρ_w and μ_w are the fluid density and dynamic viscosity, respectively, and g is the gravitational acceleration. Substitution of the effective porosity and permeability, described by (2-21) and (2-22), into (2-23) and (2-17), and combination with (2-16) enables the expression of pore water velocity in terms of the NAPL saturation:

$$v = -\frac{K (1 - S_N)^{\zeta - 1}}{\eta} \frac{dh}{dx} \tag{2-24}$$

Thus, velocities will be lower in zones with relatively high NAPL saturations (i.e., flow bypassing occurs around the low-permeability NAPL zones). Note that if a value of $\zeta = 1$ is assumed, the effect of S_N on velocity in (2-24) is eliminated. While this may not be a valid assumption for most cases, data presented by Chevalier et al. (1997) and van Valkenburg (1999) suggest that for $S_N < 0.1$, a value of $\zeta = 2$ may be reasonable. Thus, for this range of

NAPL saturations, ignoring the effect of S_N on velocity should result in errors of less than 10%. Most of the applications discussed here involve NAPL saturations of less than 0.1, and thus, throughout most of this work, the effect of the NAPL on the effective media properties is ignored. However, an approximate method of accounting for these effects is described below.

Wetting-phase contaminants are likely to form relatively thin coatings on aquifer materials. At NAPL saturations in the range of interest here (i.e., $S_N < 0.1$), the resulting effects of wetting-phase NAPLs on porosity and permeability will be much lower than those for nonwetting-phase contaminants and the errors associated with ignoring these effects should be small.

Flow bypassing. The assumption that f is representative of both the flux- and volume-averaged contaminated fractions is dependent on the effects of the NAPL on the media, as discussed above. Approaches for the consideration of flow bypassing were discussed by Soerens et al. (1998) in the context of both discrete and continuous NAPL distributions. For the homogeneous binary model, the mean velocity through the entire domain, v_T, can be expressed (adapted from Soerens et al., 1998):

$$v_T = (1 - f) v_{uc} + f v_c \tag{2-25}$$

From (2-24), the velocity in the contaminated zone can be expressed in terms of the velocity in the uncontaminated zone:

$$v_c = v_{uc} (1 - S_N)^{\zeta - 1} \tag{2-26}$$

The relative velocity through the contaminated fraction, v_c/v_T, is then:

$$\frac{v_c}{v_T} = \frac{(1 - S_N)^{\zeta - 1}}{(1 - f) + f(1 - S_N)^{\zeta - 1}}$$ (2-27)

The flux-averaged contaminated fraction of the domain, f_f, can then be expressed:

$$f_f = f \frac{v_c}{v_T}$$ (2-28)

Thus, in order to account for flow bypassing, (2-20) can then be rewritten in terms of f_f:

$$m_{N_T} = (1 - f_f) m_{N_{uc}} + f_f m_{N_c}$$ (2-29)

For the distributed binary model, each streamtube will have a different NAPL saturation, resulting in a distribution of velocities, each described by (2-26). Assuming N streamtubes in the contaminated fraction, the average velocity through the entire domain can be expressed:

$$v_T = (1 - f) v_{uc} + \frac{f}{N} \sum_{i=1}^{N} v_{c_i}$$ (2-30)

By applying (2-26) and (2-27) to individual streamtubes, the relative velocity of each can be determined as follows (again adapted from Soerens et al., 1998):

$$\frac{v_{c_i}}{v_T} = \frac{\left(1 - S_{N_i}\right)^{\zeta - 1}}{(1 - f) + \frac{f}{N} \sum_{i=1}^{N} \left(1 - S_{N_i}\right)^{\zeta - 1}}$$ (2-31)

A correction to f that accounts for flow bypassing, analogous to (2-28), must then be determined for each streamtube. If the simplifying approximation of substituting the average NAPL saturation within the contaminated zone for S_{N_i} in (2-31), then this equation reduces to (2-27). Errors resulting from this approximation should be minimal as long as the fraction of the domain that contains large NAPL saturations is small. This approach allows the use of (2-29) for both the homogeneous and distributed binary models.

In the equations presented below, the contaminated fraction will be represented as f and flow bypassing effects will be ignored. However, bypassing effects can be included through substitution of f_f for f. The impact of flow bypassing was investigated in relation to the laboratory experiments reported below but was not considered in the numerical simulations or field experiments.

<u>Homogeneous Binary Model</u>

In this model, a fraction, f, of the streamtubes within the domain are assumed to be homogeneously contaminated with NAPL at saturation S_N (Figure 2-1b). It is assumed that flow is one-dimensional and NAPL-water partitioning is instantaneous and linear. Also, each streamtube is assumed to be independent. For this analysis, only the equilibrium ADE and lognormal distribution transport models will be considered. Four parameters, then, are required to describe reactive solute transport through this binary system: two that describe the nonpartitioning solute behavior–R and P for the ADE model, and μ and σ for the lognormal distribution model–and two that describe the NAPL saturation distribution–f and S_N.

Assuming that the NAPL does not significantly affect media properties, nonpartitioning tracer transport is identical in the contaminated and uncontaminated regions. The fractional contribution of the contaminated zone to the moments of a nonpartitioning tracer BTC measured across the entire domain may be written:

$$m_{N_c}^{np} = f m_{N_T}^{np} \tag{2-32}$$

Because the contaminated and uncontaminated zone nonpartitioning tracer moments are equivalent to the total domain moments, the subscript T will be dropped when referring to the nonpartitioning tracer moments hereafter.

For a partitioning tracer, transport through the uncontaminated region of the domain should be identical to that of the nonpartitioning tracer. Thus, the moments of a partitioning tracer BTC measured across the entire domain can be expressed as follows:

$$m_{N_T}^{P} = (1-f) m_N^{np} + f m_{N_c}^{P} \tag{2-33}$$

Partitioning tracer moment equations for the contaminated portion of the domain can be developed by rearranging (2-3) to express partitioning tracer arrival time as a function of nonpartitioning tracer arrival time:

$$t_{P_c} = R t_{np} - R \frac{t_0}{2} + \frac{t_0}{2} \tag{2-34}$$

where the tracer arrival times are now considered to be random variables, and R and t_0 are constants for each streamtube. The Nth moment of a partitioning tracer BTC can then be determined by taking the expected value of both sides of (2-34):

$$m_N^p = \mathrm{E}\left[t_{P_c}^N\right] = \mathrm{E}\left[\left(Rt_{np} - R\frac{t_0}{2} + \frac{t_0}{2}\right)^N\right] \tag{2-35}$$

where the expected value operator, $\mathrm{E}[X]$ is a notation for the integral:

$$\mathrm{E}[X] \equiv \int_{-\infty}^{\infty} X f(t)\, dt \tag{2-36}$$

Expansion of (2-35) leads to expressions for the normalized temporal moments of the partitioning tracer travel time distribution measured through the homogeneously contaminated fraction of the domain. Incorporation of these equations into (2-33) results in the following expressions for the first two moments of a partitioning tracer BTC measured through the entire domain:

$$m_1^p{}_T = (1 - f)m_1^{np} + f\left[R_f m_1^{np} - R_f\frac{t_0}{2} + \frac{t_0}{2}\right] \tag{2-37}$$

$$m_2^p{}_T = (1 - f)m_2^{np} + f\left[R_f^2 m_2^{np} + R_f(1 - R_f)t_0 m_1^{np} + \frac{t_0^2}{4}\left(R_f^2 - 2R_f + 1\right)\right] \tag{2-38}$$

where R_f represents the retardation factor in the contaminated fraction and can be related to the total retardation, R_T, by $R_T = (1 - f) + fR_f$.

The parameters describing the solute travel time distribution can be determined from the nonpartitioning tracer BTC using the moment equations presented in Table 2-1. The unknown NAPL distribution parameters can then be determined from the partitioning tracer BTC moments by solving (2-37) and (2-38).

Distributed Binary Model

It is perhaps more likely that NAPL saturations within a contaminated zone will be distributed, rather than homogeneous. Here, the lognormal PDF is used to describe both the travel time and NAPL saturation distributions, where the saturation is assumed to be homogeneous within a given streamtube. Using this approach, five parameters are now required to describe reactive solute transport through the system: two parameters that describe the nonpartitioning solute behavior, μ_{np} and σ_{np}, one that quantifies the contaminated fraction of the domain, f, and two that describe the NAPL saturation distribution within the contaminated fraction, μ_{S_N} and σ_{S_N}.

The five unknown parameters can be estimated using five moment equations: two for the nonpartitioning tracer and three for the partitioning tracer. The presence of the NAPL is again assumed to have minimal impact on the nonpartitioning tracer moments. The parameters describing the solute travel time distribution can then be determined from the nonpartitioning tracer BTC using the moment equations presented in Table 2-1, as was done for the homogeneous binary model, except that here the lognormal distribution moment equations are used.

Partitioning tracer moment equations for transport through the contaminated zone can be determined by expressing partitioning tracer arrival time as a function on nonpartitioning tracer arrival time, again, as was done for the homogeneous binary model. For mathematical simplicity, it will be assumed here that the quantity $S = S_N/(1 - S_N)$, rather than S_N, is distributed lognormally. Making this simplification in (2-2) and substituting into (2-34) results in:

$$t_{p_c} = t_{np} + K_N S t_{np} - K_N S \frac{t_0}{2} \qquad (2\text{-}39)$$

where both t_{np} and S are lognormal random variables. The contaminated zone partitioning tracer moments are then:

$$m_N^p = \mathrm{E}\left[t_{p_c}^N\right] = \mathrm{E}\left[\left(t_{np} + K_N S t_{np} - K_N S \frac{t_0}{2}\right)^N\right] \qquad (2\text{-}40)$$

Solution of (2-40) requires the use of the following identities for lognormal distributions:

$$Z = XY \qquad \mu_Z = \mu_X + \mu_Y, \ \sigma_Z^2 = \sigma_X^2 + \sigma_Y^2 + 2\rho\,\sigma_X\sigma_Y \qquad (2\text{-}41)$$

$$\mathrm{E}[X^a Y^b] = m_a^X m_b^Y \exp(ab\,\rho\,\sigma_X\sigma_Y) \qquad (2\text{-}42)$$

where X, Y, and Z are lognormally distributed random variables, a and b are constants, and ρ is the correlation coefficient between X and Y (the derivations of (2-41) and (2-42) can be found in Jury and Roth (1990) and Appendix A, respectively). The correlation coefficient quantifies the degree of interrelation between two random variables and is defined:

$$\rho = \frac{\mathrm{E}\left[(X - m_1^X)(Y - m_1^Y)\right]}{\sigma_X\sigma_Y} \qquad (2\text{-}43)$$

Expansion of (2-40), and the incorporation of (2-41) and (2-42), results in the following expressions for the first three moments of the partitioning tracer BTC measured through the entire domain:

$$m_1^P{}_T = (1-f)m_1^{np} + f\left[m_1^{np} + K_N m_1^{np} m_1^S \exp(\rho\,\sigma_{np}\,\sigma_S) - m_1^S K_N \frac{t_0}{2}\right] \qquad (2\text{-}44)$$

$$\begin{aligned}
m_2^P{}_T = (1-f)m_2^{np} + f\Big[& m_2^{np} + 2K_N m_2^{np} m_1^S \exp(2\,\rho\,\sigma_{np}\,\sigma_S) \\
& - K_N t_0 m_1^{np} m_1^S \exp(\rho\,\sigma_{np}\,\sigma_S) - K_N^2 t_0 m_1^{np} m_2^S \exp(2\,\rho\,\sigma_{np}\,\sigma_S) \\
& + K_N^2 m_2^{np} m_2^S \exp(4\,\rho\,\sigma_{np}\,\sigma_S) + K_N^2 m_2^S \frac{t_0^2}{4} \Big]
\end{aligned} \qquad (2\text{-}45)$$

$$\begin{aligned}
m_3^P{}_T = (1-f)m_3^{np} + f\Big[& m_3^{np} + 3K_N m_3^{np} m_1^S \exp(3\,\rho\,\sigma_{np}\,\sigma_S) \\
& + 3K_N^2 m_3^{np} m_2^S \exp(6\,\rho\,\sigma_{np}\,\sigma_S) - 3K_N m_2^{np} m_1^S \frac{t_0}{2}\exp(2\,\rho\,\sigma_{np}\,\sigma_S) \\
& - 3K_N^2 t_0 m_2^{np} m_2^S \exp(4\,\rho\,\sigma_{np}\,\sigma_S) + 3K_N^2 m_1^{np} m_2^S \frac{t_0^2}{4}\exp(2\,\rho\,\sigma_{np}\,\sigma_S) \\
& - 3K_N^3 m_2^{np} m_3^S \frac{t_0}{2}\exp(6\,\rho\,\sigma_{np}\,\sigma_S) + 3K_N^3 m_1^{np} m_3^S \frac{t_o^2}{4}\exp(3\,\rho\,\sigma_{np}\,\sigma_S) \\
& + K_N^3 m_3^{np} m_3^S \exp(9\,\rho\,\sigma_{np}\,\sigma_S) - K_N^3 m_3^S \frac{t_0^3}{8} \Big]
\end{aligned} \qquad (2\text{-}46)$$

<u>Significance Relative to Lagrangian Stochastic Theory</u>

The moment equations listed in Table 2-1 are representative of one-dimensional solute transport. These equations can be used with BTCs that are generated from multi-dimensional transport processes, but the resulting parameters will be representative of equivalent one-dimensional processes. An alternative approach for the computation of BTC moments from parameters that are descriptive of multi-dimensional transport processes is

the stochastic Lagrangian framework that has been developed to consider nonreactive and reactive solute transport in multi-dimensional heterogeneous porous media (e.g., Dagan, 1989; Cvetkovic and Shapiro, 1990; Bellin et al., 1993; Cvetkovic et al., 1998; Demmy et al., 1999).

The appeal of the Lagrangian approach is that nonreactive and reactive tracer BTC moments can be estimated based on statistics that describe the point variability in the media and contaminant properties, with the presumption that these statistics can estimated through point sampling, while the focus here is on the inverse problem of estimating unknown media and NAPL saturation distribution parameters from tracer BTCs. Note that the models described above allow for the determination of the distribution of travel times and NAPL saturations between streamtubes, not the point distribution.

Nonpartitioning tracer transport. For a nonpartitioning tracer instantaneously injected into a heterogeneous multi-dimensional porous medium in proportion to the local velocity (i.e., injected in flux, using the terminology of Kreft and Zuber, 1978 and Demmy et al., 1999), the first two normalized temporal moments of a BTC measured at a position x along the mean flow direction can be written in terms of the media properties as follows (Demmy, 1999):

$$m_1 = \frac{x}{U} \tag{2-47}$$

$$m_2 = \frac{2\lambda\sigma_K}{U^2}\left(x + \frac{\lambda}{\kappa}\left[\exp\left(-\frac{\kappa x}{\lambda}\right) - 1\right]\right) + \left(\frac{x}{U}\right)^2 \tag{2-48}$$

where it is assumed that the hydraulic conductivity field is isotropic and exponentially correlated with correlation length λ and standard deviation σ_K, κ is a shape factor that is dependent on the media geometry, and U is the average pore water velocity and is defined

$$U = \frac{K^G J}{\theta} \psi \qquad (2\text{-}49)$$

where K^G is the geometric mean of the hydraulic conductivity field, equivalent to $\exp(\mu_K)$, J is the mean hydraulic gradient, θ is the mobile water content, and ψ is a shape factor dependent on the dimensionality of the flow system.

Partitioning tracer transport. Cvetkovic et al. (1998) developed a theoretical framework for describing reactive, or partitioning, tracer transport through multi-dimensional heterogeneous porous media based on the concept of an integrated Lagrangian reactive flow path statistic, μ. These authors derived analytical solutions for the temporal moments of a reactive tracer BTC in terms of the moments of the nonreactive tracer and μ. This approach is analogous to the streamtube-based method described above wherein partitioning tracer temporal moments were derived in terms of the nonpartitioning tracer and S distribution moments. However, the Lagrangian reactive transport equations are not simple closed-form solutions like (2-47) and (2-48). In addition, the first-order approximate solutions for the moments of μ that were presented by Cvetkovic et al. (1998) were subject to relatively large errors (e.g., 40% error in σ_μ^2 compared to numerical simulations).

Thus, the stochastic approach is particularly useful for predicting nonpartitioning tracer behavior from multi-dimensional numerical simulations, such as those presented below, wherein the mean, variance, and correlation length scale of the hydraulic conductivity

field are known *a priori*, but the prediction of partitioning tracer temporal moments with current Lagrangian methods is difficult and uncertain.

<u>Generating Model PDFs</u>

It is usually desirable to generate model BTCs for comparison with measured data following model parameter estimation from moment equations. The focus here is on representing nonpartitioning and partitioning tracer BTCs using lognormal distributions.

The lognormal PDF parameters, μ and σ, can be written in terms of the first two moments from a measured BTC (Table 2-1) as follows:

$$\mu = 2\ln(m_1) - \frac{\ln(m_2)}{2} \tag{2-50}$$

$$\sigma^2 = \ln(m_2) - 2\ln(m_1) \tag{2-51}$$

Model fits to simple nonpartitioning tracer BTCs can then be generated directly from (2-14).

Under the binary NAPL distribution framework, partitioning tracer BTCs can be generated through the superposition of solutions of (2-14) for the uncontaminated and contaminated zones. In the uncontaminated zone, the nonpartitioning and partitioning tracer travel time distributions are considered to be the same and can be represented with a single lognormal distribution. In the contaminated zone, (2-34) and (2-39) reveal t_{p_c} to be equivalent to a sum of lognormal distributions for both the homogeneous and distributed binary models, where the constants in (2-34) are considered zero-variance distributions. The sum of N lognormal random variables has been demonstrated to be very closely

approximated by a lognormal distribution (Schwartz and Yeh, 1982; Abu-Dayya and Beaulieu, 1994). Therefore, for both binary models, moments representative of tracer travel through only the contaminated zone can be determined by subtracting the fractional contribution of the uncontaminated zone from the total BTC moments as described by (2-20). The contaminated zone lognormal model parameters are then determined from (2-50) and (2-51). This approach was employed to generate the model BTCs for the numerical simulations and laboratory experiments described below.

Accurate description of nonpartitioning tracer transport through complex flow fields, such as those encountered at the field scale, may require the superposition of multiple solutions of (2-14). For example, Helms et al. (1999) observed that nonpartitioning tracer BTCs measured at several multilevel sampler locations at a Hill Air Force Base, UT field site were bimodal, with two distinct peaks, and could be fit effectively with the superposition of multiple ADE solutions. A similar superposition approach was employed by Abbaszadeh-Dehghani and Brigham (1984) to fit multimodal BTCs from layered systems. Helms et al. (1999) found that nonlinear regression of the superposition of multiple ADEs also performed well for asymmetric BTCs, characterized by an early peak followed by a long, dispersed tail, typical of many field-measured BTCs.

While a sum of lognormal distributions is lognormal, a superposition of lognormal distributions is not. Therefore, for cases where multimodal nonpartitioning tracer models are required, such as the field experiments reported below, t_{np} is not lognormal and t_{p_c}, therefore, may no longer be considered as a simple sum of lognormal distributions. In these cases, t_{p_c} must be determined numerically by summing the cumulative distribution functions

(CDFs) of each term in (2-34) or (2-39). In the distributed binary model, for example, the CDF of the first term of (2-39), t_{np}, is determined by summing the PDFs of the individual modes and then integrating the sum total. The third term of (2-39) is a lognormal distribution multiplied by a constant and the CDF is generated by simply integrating the PDF. However, determination of the CDF for the second term of (2-39) requires multiplication of the CDFs for S and t_{np} using Monte Carlo techniques. The model-predicted partitioning tracer BTC can then be determined by numerically differentiating the sum total CDF of (2-39). However, numerical differentiation may be subject to considerable errors (for a discussion of the potential pitfalls of numerical differentiation, see Atkinson, 1985). Therefore, for the field experiments presented below, the measured BTCs were numerically integrated such that comparisons were made between the measured and modeled CDFs, rather than the PDFs.

Incomplete Data and Truncated Moment Expressions (TMEs)

Introduction

An important consideration when using the method of moments to estimate parameters from measured BTC data is that while virtually all measured travel time distributions are truncated, particularly those measured at the field scale, the moment equations presented in Table 2-1 were derived for complete distributions. Truncation of experimentally determined BTCs generally arises from either limited experiment durations or tracer concentrations decreasing at late times to levels below analytical detection limits. Errors resulting from the application of complete distribution moment equations to

incomplete, or truncated, data sets have led many investigators to criticism of the method of moments and the promulgation of alternate parameter estimation methods (Clements, 1969; Østergaard and Michelsen, 1969; Anderssen and White, 1970; Fahim and Wakao, 1982). Two commonly employed methods of accounting for incomplete BTC data are exponential extrapolation (Sater and Levenspiel, 1966; Jin, 1995) and the time-domain fitting of a model to the measured data by nonlinear regression (NLR) (Clements, 1969). Helms et al. (1999) applied exponential extrapolation and NLR methods to truncated synthetic BTCs that were generated with the ADE, demonstrating that very accurate estimates of the complete BTC moments could be obtained through NLR of the appropriate model (i.e., the model used to create the synthetic data).

Another approach for parameter estimation from incomplete data is to compare the numerically integrated moments of the incomplete BTC to the truncated moments of the model (Kafarov, 1968). Delay et al. (1998) derived truncated moment expressions for the ADE, however, solution of these equations requires finite difference techniques. Here, truncated moment expressions (TMEs) are derived for the lognormal distribution. These expressions are much simpler than those for the ADE (Delay et al., 1998) and are readily applicable to the lognormal solute travel time and NAPL distribution models described above.

Derivation of Lognormal Distribution TMEs

The determination of partial moments for truncated distributions requires that the limits of integration of (2-15), zero and infinity, be replaced by the initial and final times for

which data are available, t_i and t_{max}, respectively. Substitution of (2-14) into (2-15) with the new integration limits and the following change of variable

$$y(t) = \frac{\ln(t) - \mu}{\sigma} \tag{2-52}$$

results in

$$m_N(t_i, t_{max}) = \exp(N\mu + N^2\sigma^2/2) \int_{y(t_i)}^{y(t_{max})} \frac{1}{\sqrt{2\pi}} \exp\left(-\frac{(y - N\sigma)^2}{2}\right) dy \tag{2-53}$$

where the truncated moment is now a function of t_i and t_{max}. Substitution into (2-53) of the following error function identity:

$$\int_0^z \exp(-a^2\zeta^2)d\zeta = \frac{\sqrt{\pi}}{2a} \operatorname{erf}(az) \tag{2-54}$$

where $a = 1/\sqrt{2}$ and ζ is a dummy variable, results in the solution

$$m_N(t_i, t_{max}) = \exp(N\mu + N^2\sigma^2/2) \frac{1}{2}\left[\operatorname{erf}\left(\frac{y(t_{max}) - N\sigma}{\sqrt{2}}\right) - \operatorname{erf}\left(\frac{y(t_i) - N\sigma}{\sqrt{2}}\right)\right] \tag{2-55}$$

The following expression for the Nth normalized moment of a lognormal travel time distribution results from the special case of (2-55) where t_i and t_{max} are equal to zero and infinity, respectively:

$$m_N = \exp(N\mu + N^2\sigma^2/2) \tag{2-56}$$

Equation (2-56) is the commonly presented (e.g., Aitchison and Brown, 1957; Jury and Roth, 1990) moment function for lognormal distributions that was used to generate the moment

equations in Table 2-1. This relation can be employed for parameter estimation by expanding for $N = 1$, 2 and solving for μ and σ, resulting in (2-50) and (2-51). It is emphasized, however, that this method of parameter estimation is strictly valid only for complete distributions. Accurate parameter estimation for incomplete distributions requires the solution of (2-55) through iterative regression for μ and σ. The error function terms in (2-55) are the correction terms that account for truncation. Note that at a given truncation level, as the moment order increases (i.e., increasing values of N) the truncated moments represent decreasing fractions of the true complete moments. Also, note that (2-55) and (2-56) are valid for Nth absolute moments normalized by the complete zeroth moment.

A discussion of the application of the TME approach to three artificially truncated synthetic tracer BTCs is presented in Appendix B.

Numerical Simulations

One-dimensional numerical simulations were conducted to demonstrate the utility of both the homogeneous and distributed binary NAPL distribution models. In addition, simulations conducted using the two-dimensional particle tracking code described by Demmy (1999) were used to investigate the effect of a correlation between nonpartitioning tracer travel time and NAPL saturation. Temporal moments were determined from simulated BTCs by numerical integration and parameters were estimated using the equations developed above.

Homogeneous Binary Model

For the homogeneous binary model, simulations were conducted using the code UFBTC developed by Jessup and Rao (1990), which incorporates the Brenner (1962) solution to the ADE. The parameters used in the simulations were selected to approximate the laboratory experiments reported below: $L = 62$ cm, $A = 30$ cm^2, $\eta = 0.36$, $Q = 4$ mL/min, $P = 124$, $t_o = 25$ min, and $K_N = 20$. The resulting pore volume of 670 mL was used as a scaling factor when calculating dimensionless variables and moments.

The BTCs of Figure 2-2 were generated based on the scenarios described in Figure 2-1. For the domain of Figure 2-1a, the partitioning tracer BTC was similar in shape to the nonpartitioning tracer BTC, but was temporally displaced and exhibited more spreading. For the domain of Figure 2-1b, however, the partitioning tracer BTC was bimodal. The first mode was representative of transport through the uncontaminated zone and closely followed the nonpartitioning tracer BTC, while the second mode was representative of transport through the contaminated zone and was thus relatively highly retarded.

The first two normalized temporal moments (in units of PV^N) for the nonpartitioning and partitioning tracers are also shown in Figure 2-2. In these simulations, the effect of S_N on media properties was ignored. Therefore, because (2-2) implicitly accounts for the effect of S_N on porosity, m_1^P was not the same for both simulations, even though the same NAPL volume was assumed in both scenarios. Solution of the first two ADE moment equations (Table 2-1) using the nonpartitioning tracer moments, and (2-37) and (2-38) using the partitioning tracer moments, resulted in the recovery of the input parameters P, R, f, and S_N with errors of less than 0.5% for both simulation scenarios.
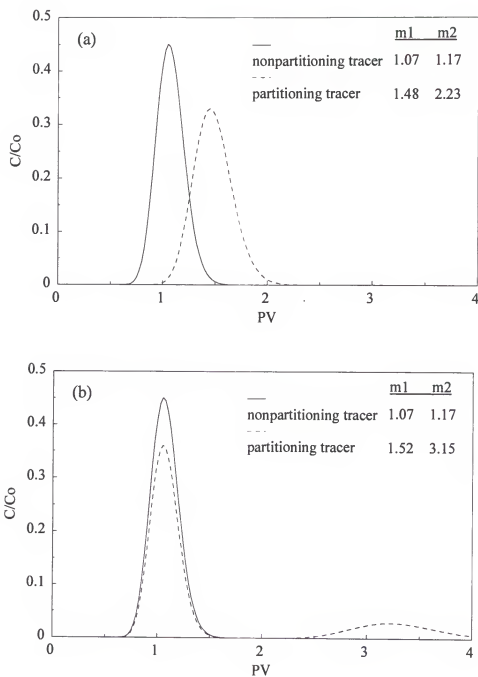
Figure 2-2. Simulated BTCs for nonpartitioning and partitioning tracer transport through the domains described in Figure 2-1.

Distributed Binary Model: One-Dimensional Simulations

In the distributed binary model, both the NAPL saturation and the solute arrival time distributions are represented using lognormal PDFs. The lognormal and ADE models produce similar BTCs when the model parameters are optimized to each other through moment matching (Jury and Roth, 1990). Therefore, in order to create a nonpartitioning tracer BTC similar to those from the homogeneous binary model simulations, equivalent nonpartitioning tracer lognormal model parameters were determined by substituting the ADE moments listed in Figure 2-2 into (2-50) and (2-51), resulting in $\mu_{np} = 5.185$ and $\sigma_{np} = 0.124$.

An arbitrary S distribution, $\mu_S = -3.7$ and $\sigma_S = 0.7$ (Figure 2-3a), was discretized over 1000 streamtubes, while an additional 250 streamtubes remained uncontaminated ($f = 0.8$). Nonpartitioning tracer transport was equivalent for each streamtube and was described by μ_{np} and σ_{np}. Because each streamtube was characterized by a single NAPL saturation, rather than a distribution of saturations, the partitioning tracer arrival time for each streamtube was simplified from (2-39) to (2-34). As described above, t_{p_c} in (2-34) and (2-39) represents a sum of lognormal random variables and can be considered lognormal as well. Thus, the total partitioning tracer BTC was generated from the superposition of solutions of (2-14) for each streamtube, where the lognormal parameters μ_p and σ_p were determined for each streamtube from (2-50) and (2-51) using (2-35) expanded for $N = 1, 2$.

The resulting nonpartitioning and partitioning tracer BTCs are presented in Figure 2-3b. In this case, the asymmetric S distribution caused more asymmetry in the partitioning tracer BTC than was observed in the nonpartitioning tracer BTC. Also because of this asymmetry, the partitioning tracer BTC was not bimodal, as would have been expected for
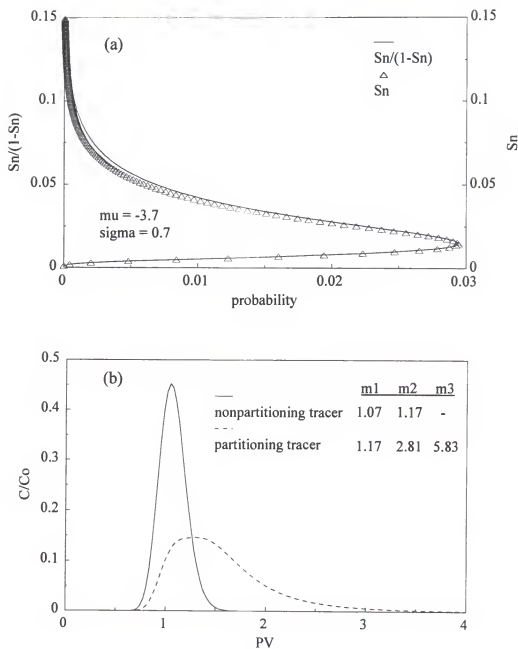
Figure 2-3. (a) Lognormal S distribution. (b) Simulated BTCs for nonpartitioning and partitioning tracer transport through a two-dimensional domain wherein 20% of the streamtubes were uncontaminated and the remainder were characterized by the S distribution of (a).

a homogeneous binary case where 20% of the streamtubes were uncontaminated. The measured values of the first two nonpartitioning and first three partitioning tracer normalized temporal moments are also shown in Figure 2-3b. Solution of (2-50) and (2-51) with the nonpartitioning tracer moments and (2-44)-(246) with the partitioning tracer moments resulted in the recovery of the model input parameters μ_{np}, σ_{np}, f, μ_S, and σ_S with errors of less than 0.5%.

Distributed Binary Model: Two-Dimensional Simulations

Particle tracking approach. Particle tracking simulations were conducted using the code described by Demmy (1999) to investigate the applicability of the correlated moment expressions (2-44)-(2-46). A summary of the simulation methods follows; additional details can be found in Demmy (1999) and Demmy et al. (1999). A turning bands algorithm (Tompson et al., 1989) was used to generate an exponentially correlated, lognormally distributed, isotropic saturated hydraulic conductivity field ($\mu_K = 0.0$, $\sigma_K = 1.0$) 46 correlation lengths, λ, in the mean flow direction x, by 36 λ in the y direction, with five conductivity blocks per correlation length (230×180 blocks). Constant head boundaries were specified at $x = 0$ and $x = 46$ λ with an average gradient of 0.02 and a homogeneous mobile water content of 0.2. A mixed finite element scheme was used to generate a system of coupled pressure-velocity equations that were solved to produce a velocity field for input into a particle tracking scheme. A Monte Carlo approach similar to that suggested by Cvetkovic et al. (1998) was employed wherein 2000 realizations of the flow field were generated and a single particle was injected into each at $x = 3$ λ, $y = 18$ λ. Particle arrival times were

recorded at $x = 39 \lambda$. This approach is conceptually equivalent to a uniform injection boundary condition for 2000 streamtubes. However, flux-weighted injection is more representative of interwell tracer tests, and the measured arrival times were thus weighted by their initial velocities, v_0 (see Kreft and Zuber, 1978 and Demmy et al., 1999 for discussions on the significance of uniform versus flux boundary conditions).

Solute BTCs are analogous to PDFs, but because of the discrete nature of the particle tracking method, particle arrival time distributions were represented as CDFs, $P(t)$. Flux-weighted CDFs were generated from the measured nonpartitioning and partitioning particle arrival times as follows:

$$P(t_i) = \frac{\sum_{j=1}^{i} v_{0,j} t_j}{\sum_{j=1}^{n} v_{0,j}} \tag{2-57}$$

where $P(t_i)$ represents the probability that the arrival time of particle i will be less than or equal to t, and n is the total number of particles.

Correlation between S_N and K. As discussed above, little experimental evidence exists to support a general model for a correlation between S_N and K. However, it will be assumed here that the general framework that has been developed for investigating correlations between K_d and K is applicable, subject to the consideration of constraints specific to NAPL contamination. Field measurements have indicated an approximately linear relationship between the logarithms of K_d and K (Robin et al., 1991; Tompson, 1993).

By substituting S for K_d and adding an uncorrelated component, this relationship can be expressed as follows:

$$\ln S = a + b \ln K + c \ln W \tag{2-58}$$

where W is a lognormally distributed random variable ($\mu_W = 0$, $\sigma_W = 1$) with the same spatial correlation structure as the K field. A relation similar to (2-58) was employed by Cvetkovic et al. (1998). For $b \neq 0$, S and K approach perfect correlation (i.e., $\rho = \pm 1$) as $c \to 0$, while $b = 0$ results in the uncorrelated case. A simplified approach is to assume $a = c = 0$ and investigate the effects of perfect positive and negative correlation, with $b > 0$ and $b < 0$, respectively. Modeling and analytical studies often implement this approach with $b = \pm 1$ (e.g., Bellin et al., 1993; Bosma et al., 1993; Soerens et al., 1998). However, the resulting variability in S, or K_d, will be equivalent to the K variability and may be unrealistically high. Tompson (1993) selected values of a and b to more closely mimic field measurements, but only investigated perfect correlation (i.e., $c = 0$).

Based on the arguments presented above, a relatively large value of $c = 0.75$ was selected here to create a weak correlation between S and K, and a value of $b = 0.3$ was selected to restrict the S values to a more limited range than K. Note that by rewriting (2-58) as $S = aK^bW^c$, it becomes apparent that $\mu_S = a$ and $\sigma_S = (b^2\sigma_K^2 + c^2\sigma_W^2)^{0.5}$ (see Appendix A). Thus, a value of $a = -3.27$ was selected to produce an average NAPL saturation of 0.05. The resulting relationships between S and K are presented in Figure 2-4 for $b = \pm 0.3$, with the corresponding S_N distributions plotted on the secondary y-axis. Note that the relationships in this figure represent the mean correlations (equivalent to $c = 0$).
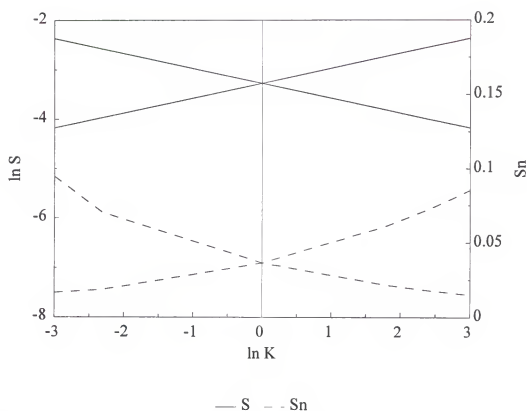
Figure 2-4. Relationship between K and S for positive and negative correlations (positive and negative slopes, respectively), with a and b in (2-58) equal to -3.27 and ± 0.3, respectively. The corresponding relationships between K and S_N are shown on the secondary y-axis.

For the uncorrelated case, values of a, b, and c were selected such that the mean and variance of the resulting S distribution would be equivalent to those for the correlated cases ($a = -3.27$, $b = 0$, $c = 0.81$).

Streamtube-average NAPL saturation. The average NAPL saturation (more exactly, the average value of S) that was observed along the trajectory of each particle was calculated as follows:

$$\hat{S}_i = \frac{\displaystyle\int_0^x \frac{S(x)\,dx}{v(x)}}{\displaystyle\int_0^x \frac{dx}{v(x)}} \qquad (2\text{-}59)$$

The resulting $\hat{S}_i$ values are analogous to the Lagrangian reaction flow path parameter, μ, described by Cvetkovic et al. (1998), and it is the statistics of this distribution that are determined from (2-44)-(2-46).

The simulations presented here were conducted with $f = 0.8$. Therefore, for 20% of the particles (randomly selected), K_N was set equal to 0 so that the nonpartitioning and partitioning tracer arrival times would be equal. For the remainder of the particles, the partitioning tracer arrival time was determined from the nonpartitioning tracer arrival time using (2-39) with $K_N = 20$ and $\hat{S}_i$.

Results: Nonpartitioning tracer transport. The first three temporal moments for the nonpartitioning and partitioning tracer CDFs are presented in Table 2-2 with units of PV^N (the PV was determined from the nonpartitioning tracer first moment). The nonpartitioning

Table 2-2. Temporal moments for nonpartitioning and partitioning tracer CDFs from two-dimensional particle tracking simulations.

Source of Moment Estimate	m_1	m_2	m_3	RMSD
Nonpartitioning Tracer				
Measured	1.0	1.052	1.165	-
Lognormal model fit	1.0	1.052	1.163	9.93E-4
Lagrangian prediction	0.986	1.026	-	2.00E-2
Partitioning Tracer				
$\rho_{K,S} = 0.0$				
Measured	1.836	3.775	8.522	-
[a] Model fit	1.836	3.775	8.507	9.93E-4
$\rho_{K,S} > 0$				
Measured	1.856	3.798	8.365	-
[b] Model fit	1.856	3.798	8.365	4.26E-5
[b] Model fit with $\rho_{K,S} = 0.0$	1.858	3.796	8.368	6.37E-4
$\rho_{K,S} < 0$				
Measured	1.816	3.766	8.817	-
[b] Lognormal model fit	1.816	3.765	8.817	6.71E-5
[a] Model fit with $\rho_{K,S} = 0.0$	1.816	3.766	8.802	9.93E-4

[a] These moments were calculated from the parameters listed in Table 2-3 that were determined from arithmetic solution of (2-44)-(2-46). [b] Moments calculated from (2-44)-(2-46) such that the RMSD from the measured moments was minimized. The minimum solution was found using a spreadsheet optimization routine.

tracer travel time lognormal model parameters, μ_{np} = -0.025 and σ_{np} = 0.225, were determined from the nonpartitioning tracer moments using (2-50) and (2-51). The moments generated from (2-56) using these parameters are compared in Table 2-2 to the measured values. Estimates of the first two nonpartitioning tracer moments determined from solution of (2-47) and (2-48), with κ = 3/8 and ψ = 1 for a two-dimensional domain (Demmy, 1999), are also compared to the measured values in Table 2-2. The stochastic theory resulted in estimates that were within 1.4% and 2.5% of the measured values for the first and second moments, respectively.

Note that σ_{np} was much lower than σ_K, indicating that much of the variability in the point statistics was damped out in the integrated measure. This effect has a significant impact on the interpretation of the $\hat{S}$ distribution statistics, as discussed below.

The flux-weighted measured nonpartitioning tracer CDF is shown in Figure 2-5a along with the partitioning tracer CDFs for the correlated and uncorrelated cases. The model CDF for the nonpartitioning tracer was generated from (2-14) using the μ_{np} and σ_{np} values given above.

Results: Partitioning tracer transport. Presented along with the measured partitioning tracer moments in Table 2-2 are the moment estimates determined from (2-44)-(2-46) using the $\hat{S}$ distribution parameters listed in Table 2-3. For the uncorrelated case, (2-44)-(2-46) were solved algebraically using the measured nonpartitioning and partitioning tracer moments to determine the S distribution parameters. However, for correlated cases, algebraic solution of these equations is difficult, if not impossible. For these cases, $\hat{S}$ distribution parameters were estimated using an optimization routine where the root mean
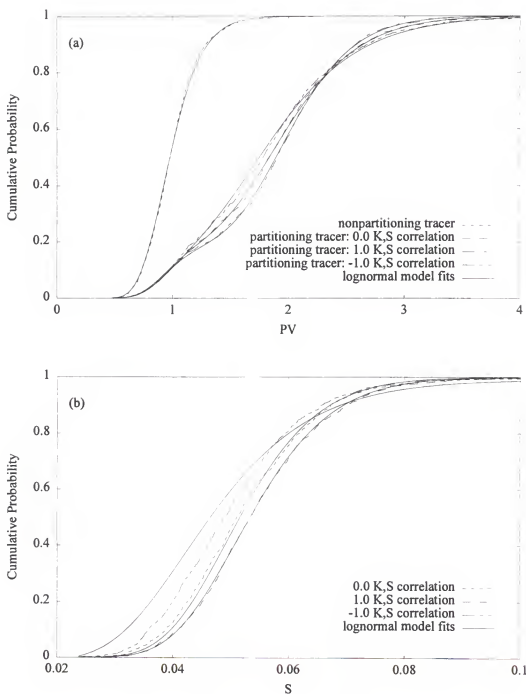
Figure 2-5. (a) Nonpartitioning and partitioning tracer CDFs from the particle tracking simulations with model fits determined from the CDF moments and (2-44)-(2-46) (i.e., the distributed binary model). (b) Measured and estimated $\hat{S}$ distributions for each case.

Table 2-3. Measured and estimated $\hat{S}$ distribution moments and model parameters from two-dimensional particle tracking simulations.

Estimate Source	$\hat{S}$ Distribution Moments				$\hat{S}$ Distribution Parameters			
	m_1 (10^{-2})	m_2 (10^{-3})	m_3 (10^{-4})	RMSD (10^{-2})	$\rho_{t,\hat{S}}$	f	$\mu_{\hat{S}}$	$\sigma_{\hat{S}}$
$\rho_{K,S} = 0.0$								
Measured	5.253	2.906	1.700	-	-0.04	0.800	-2.974	0.219
[a]Model fit	5.265	2.892	1.657	1.51	0.0	0.794	-2.965	0.205
$\rho_{K,S} > 0$								
Measured	5.466	3.123	1.868	-	-0.35	0.800	-2.930	0.207
[b]Model fit	5.445	3.093	1.834	1.21	-0.35	0.799	-2.932	0.206
[b]Fit with $\rho_{t,\hat{S}} = 0.0$	5.178	2.699	1.417	16.28	0.0	0.828	-2.964	0.082
$\rho_{K,S} < 0$								
Measured	5.035	2.692	1.539	-	0.29	0.800	-3.020	0.233
[b]Model fit	4.824	2.547	1.471	4.70	0.30	0.828	-3.077	0.300
[a]Fit with $\rho_{t,\hat{S}} = 0.0$	5.062	2.947	1.973	17.17	0.0	0.806	-3.053	0.374

[a] Parameters determined from arithmetic solution of (2-44)-(2-46). [b] Parameters determined from spreadsheet optimization routine where the RMSD between the measured moments and those calculated from (2-44)-(2-46) was minimized.

squared deviation (RMSD, see Appendix B) between the measured partitioning tracer moments and those calculated from (2-44)-(2-46) were minimized.

Model partitioning tracer CDFs were generated from the superposition of solutions of (2-14) for the uncontaminated and contaminated zones, as discussed above. These model CDFs are plotted along with the measured CDFs in Figure 2-5a. For all three cases, the model fits matched the measured CDFs closely.

Examination of the moments listed in Table 2-2 reveals that a positive correlation between K and S led to greater partitioning tracer retardation than for the uncorrelated case, and vice versa for a negative correlation, despite the fact that the point values for S, as determined from (2-58), exhibited the same mean and variance for all cases. Similar effects with K and K_d correlations were observed in numerical simulations by Tompson (1993), and predicted theoretically by several investigators (Dagan, 1989; Kabala and Sposito, 1991; Cvetkovic et al., 1998). Also, if the spread of each partitioning tracer CDFs is measured by the second central moment ($\mu_2^{'} = m_2 - m_1^2$), then it can be seen from the moments in Table 2-2, as well as from the CDFs in Figure 2-5a, that the spreading of the partitioning tracer CDF was greater for the negatively correlated case ($\mu_2^{'} = 0.47$) than for the uncorrelated case ($\mu_2^{'} = 0.40$), and vice versa for the positively correlated case ($\mu_2^{'} = 0.35$). This effect has also been either predicted or observed by several investigators (Kabala and Sposito, 1991; Bellin et al., 1993; Bosma et al., 1993; Tompson, 1993).

Results: Estimation of NAPL saturation distribution parameters. The estimated $\hat{S}$ distribution parameters are compared to the measured values in Table 2-3. The $\hat{S}_l$ values determined from (2-59) were flux-weighted according to (2-57) in order to create the

measured $\hat{S}$ CDF. The measured CDFs representing the $\hat{S}$ distribution within the contaminated fraction of the domain are compared in Figure 2-5b to those created from (2-14) using the parameters in Table 2-3.

The correlation between the nonpartitioning tracer travel time and $\hat{S}$, $\rho_{t,\hat{S}}$, was calculated using (2-43). Note that, as suggested by (2-19), a positive correlation between K and S resulted in a negative value of $\rho_{t,\hat{S}}$, and vice versa. The measured $\hat{S}_i$ values are plotted for each case with the corresponding nonpartitioning tracer arrival times in Figure 2-6. The effect of the relatively large value of c in (2-58) can be seen in the high degree of scatter in each plot in Figure 2-6.

For the uncorrelated and positively correlated cases, the estimated $\hat{S}$ distributions matched the measured distributions closely, while the fit was not as close for the negatively correlated case. For the negatively correlated case, the fit of the estimated $\hat{S}$ distribution to the measured distribution improves as approaches as the ratio b/c in (2-58) decreases (i.e., as the degree of correlation between K and S approaches zero). Conversely, the fit becomes worse as b/c increases. This may be because the $\hat{S}$ distributions resulting from negative correlations between K and S are less-well represented by lognormal distribution than for the other cases.

As was observed with K, much of the point variability in S was damped out in the integrated measure, $\hat{S}$. The measured ratios of $\sigma_{\hat{S}}$ to σ_S for the cases studied here (0.27, 0.26, and 0.29 for the uncorrelated, positively, and negatively correlated cases, respectively) were close to the ratio of σ_{np} to σ_K (0.23). The same effect was also manifested in the correlation between K and S, however, the degree of dampening was less. For example,
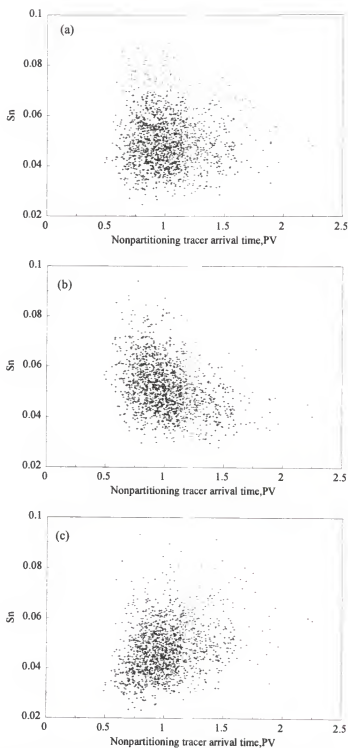
Figure 2-6. Measured relationship between the average NAPL saturation along each of N = 2000 particle trajectories and the nonpartitioning tracer travel time, measured in pore volumes (PV), for cases where the point values of K and S were (a) uncorrelated, (b) positively correlated, and (c) negatively correlated.

when a value of $c = 0$ was used in (2-58) (i.e., $\rho_{K,S} = 1.0$), $\rho_{t,\hat{S}}$ values of approximately 0.8 were measured for both positively and negatively correlated cases. The correlation between K and S decreases as c in (2-58) increases, and the effective $\rho_{t,\hat{S}}$ value will be somewhat lower still. The extent of these integration effects are related to the degree of heterogeneity within the system. Here, only a single value of σ_K was used, however, further study may result in a predictive relationship between point and integrated statistic variability.

The errors associated with ignoring the correlation between K and S were also investigated. Listed in Tables 2-2 and 2-3 are the estimated partitioning tracer moments and $\hat{S}$ distribution parameters that resulted when $\rho_{t,\hat{S}}$ was assumed to be equal to zero for both the positively and negatively correlated cases. Note that for both cases, very good agreement was obtained with the measured partitioning tracer moments, but the resulting estimates of the $\hat{S}$ distribution moments and parameters were relatively poor. These results point to the potential pitfall, when using tracer BTC moments for parameter estimation, of multiple solutions producing moment estimates that are quite close to the measured values. For example, the moment estimates obtained from the negatively correlated case where it was assumed that $\rho_{t,\hat{S}} = 0$ were obtained from algebraic solution of (2-44)-(2-46). While, here, the more-correct solutions (i.e., $\rho_{t,\hat{S}} \neq 0$) produced the lowest RMSD values (Table 2-2), it may be difficult to differentiate between the solutions for $\rho_{t,\hat{S}} = 0$ and $\rho_{t,\hat{S}} \neq 0$ with no prior information as to the expected correlation between K and S. Note that the magnitude of the errors that will be realized upon assuming that $\rho_{t,\hat{S}} = 0$ will be reduced as the ratio b/c decreases. Also, note that, for the correlated cases considered here, while the $\hat{S}$ distribution parameters that were estimated by assuming $\rho_{t,\hat{S}} = 0$ were not particularly representative of

the true distributions, the estimated values of f were reasonable. This result suggests that if the correlation between K and S is relatively weak, reasonable estimates of the fraction of the streamtubes in the domain that are contaminated may be obtained even if correlation effects are ignored.

Finally, it is noted that the effects on the retardation and spreading of the partitioning tracer CDFs that resulted from correlations between K and S were manifestations of the effects of these correlations on the $\hat{S}$ distribution first and second moments (Table 2-3). A positive correlation between K and S resulted in an increased first moment of $\hat{S}$ and decreased spreading ($\mu_2' = 1.35E{-}4$) compared to the uncorrelated case ($\mu_2' = 1.47E{-}4$), and vice versa for a negative correlation ($\mu_2' = 1.57E{-}4$). It is interesting to note that strong positive correlations between K and S may result in overpredictions of the amount of NAPL present in a system, while strong negative correlations may result in underpredictions.

<u>Laboratory Experiments</u>

Laboratory experiments were conducted in a flow chamber that was packed with a combination of clean 20-30 mesh Ottawa sand and sand mixed with n-decane to create a scenario similar to that of Figure 2-1b. Partitioning tracer tests were conducted and nonpartitioning and partitioning tracer BTC moments were calculated with the goal of recovering the design parameters f and S_N using the NAPL distribution models described above.

Laboratory Experimental Methods

The laboratory flow chamber was similar in design to that described by Jawitz et al. (1998a). The open-top chamber enclosed a volume of 62 cm length, 1.4 cm width, and 39 cm height and was constructed of two glass plates closed on three sides by 1.3 cm square aluminum tubing. The vertical sections of tubing on either end were slotted to a width of 0.03 cm at a frequency of 4 slots per cm, enabling homogeneous injection and extraction of fluids. Clean zones were packed by slowly pouring untreated sand into standing water in the chamber, while the contaminated zone was created by adding a mixture of 731 g of sand, 150 mL of water, and 7.7 mL of n-decane in approximately 10 g increments. These proportions were selected to provide a NAPL saturation of approximately 0.05 in a sand that was assumed to have a porosity of 0.36. Decane was selected as the NAPL because of its low aqueous solubility (0.009 mg/L, Verschueren, 1983), facilitating multiple tracer tests without significant NAPL mass loss due to dissolution. The water table was maintained at the top of the media during the addition of contaminated sand to minimize gravity segregation of the sand, water, and n-decane during emplacement. The total packed height in the flow chamber was 10.4 cm, with a 5 cm contaminated zone (731 g of sand) enveloped by clean zones above (3.4 cm, 513 g) and below (2 cm, 284 g). The measured bulk density of the packing was 1.7 g/cm³, which, for sand, corresponds to a porosity of 0.35.

Based on the total masses of clean and contaminated sand that were packed, the contaminated fraction was determined to be 0.48. However, the effective volumetric fraction that was realized may have varied from the measured value because of nonuniform packing or trapped air. Also, the sand, water, and n-decane were mixed in a glass beaker, and a

residue of *n*-decane was left behind following the transfer of the mixture to the flow chamber. In consideration of these factors, the true values of the NAPL saturation distribution parameters were considered to be $f = 0.48 \pm 0.05$ and $S_N = 0.048 \pm 0.05$.

A constant head reservoir was used to deliver fluids to the flow chamber through the injection well and a positive displacement pump (Masterflex L/S drive equipped with a Fluid Metering Inc. Q Pump head) was used to remove fluids through the extraction well. The effluent was pumped through an in-line flow cell attached to a gas chromatograph equipped with an autosampler (Perkin Elmer AutoSystem), allowing for quantification of tracer concentrations without discrete sampling. For each partitioning tracer test, a tracer pulse of approximately 0.15 PV was delivered to the injection well with a syringe pump (Harvard Apparatus 22) during steady-state water flow. During each tracer test, wax paper was placed over the media-air interface to minimize volatile losses of tracers. The tracer tests were continued until the tracer concentrations measured in the effluent were below detection limit (generally 1 mg/L). Application of the lognormal truncated moment method was investigated for moment estimation, but it was determined that because the measured BTCs were relatively complete, simple exponential extrapolation (Jin, 1995) was sufficient to provide accurate moment estimates.

Methanol was used as the nonpartitioning tracer, with 2,2-dimethyl-3-pentanol (DMP) and 6-methyl-2-heptanol (6M2H) as partitioning tracers. The fluid flow rates and tracer initial concentrations were varied to investigate the effects of nonequilibrium and nonlinear partitioning, respectively. Pore water velocities and tracer concentrations for each experiment are listed in Table 2-4.

Table 2-4. Pore water velocities and tracer initial concentrations for each laboratory experiment.

			$C_0{}^\dagger$		
Experiment Number		v (m/d)	Methanol (mg/L)	DMP (mg/L)	6M2H (mg/L)
E1	(v_0, C_0)	17.3	2500	500	180
E2	$(v_0/2, C_0)$	8.7	2500	500	180
E3	$(v_0/6, 0.5C_0)$	2.9	2500	250	90
E4	$(v_0/6, C_0)$	2.9	2500	500	180
E5	$(v_0/6, 2C_0)$	2.9	2500	1000	360
E6	$(v_0/6, 3C_0)$	2.9	2500	1500	540
E7	$(v_0/12, C_0)$	1.4	2500	500	180

$\dagger$ Partitioning tracer C_0 values were equivalent to approximately 6% of aqueous solubility.

The velocity of Experiment 1 (E1) (determined from (2-17) with $Q = 6$ mL/min) was chosen as an upper limit of approximately 10 times that suggested by Jin et al. (1995) for equilibrium conditions. Velocities lower than 1.4 m/d (E7) were not investigated because of concerns about mass loss of tracers due to volatilization. Also, field experimental experience suggests that lower velocities may not be practical for field implementation (see the discussion of field data below and Annable et al., 1998b; Sillan, 1999).

The aqueous solubility of DMP has been reported to be 8200 mg/L (Barton, 1984) and the solubility of 6M2H was estimated to be approximately 3000 mg/L (based on the solubilities of other methylated heptanols, as reported by Barton, 1984). The relatively low C_o values for DMP and 6M2H in E1 (approximately 6% of aqueous solubility) were selected to minimize the effects of NAPL-water tracer partitioning isotherm nonlinearities, demonstrated by Wise (1998) to become significant at C_o values above approximately 10% of aqueous solubility. In subsequent experiments, these C_o values were varied to ascertain whether nonlinear partitioning was a factor in these experiments.

The decane-water partitioning coefficients for DMP and 6M2H, $K_N = 12$ and 25, respectively, were measured using batch equilibration methods.

<u>Laboratory Results</u>

<u>Nonpartitioning tracer transport</u>. The first three normalized temporal moments of the nonpartitioning tracer BTCs measured from each experiment are presented in Table 2-5 (all moments presented here are in units of PV^N) along with the estimated lognormal distribution parameters. Because the lognormal model parameters were calculated from the first two

Table 2-5. Measured and estimated nonpartitioning tracer moments and model parameters from each laboratory experiment.

Experiment Number	Measured Moments			Calculated Moment [a]	Lognormal Parameters [b]	
	m_1	m_2	m_3	m_3	μ_{np}	σ_{np}
E1	1.070	1.156	1.261	1.261	0.063	0.096
E2	1.069	1.158	1.272	1.271	0.060	0.115
E3	1.068	1.153	1.262	1.261	0.059	0.109
E4	1.067	1.155	1.267	1.265	0.059	0.114
E5	1.072	1.172	1.309	1.307	0.060	0.140
E6	1.067	1.161	1.290	1.287	0.055	0.139
E7	1.064	1.148	1.259	1.258	0.054	0.121

[a] Calculated from (2-56) with the given lognormal parameters. [b] Determined from (2-50) and (2-51).

measured moments using (2-50) and (2-51), the measured moments and those computed from (2-56) were identical for $N = 1,2$. However, the relative agreement between the estimated and measured third moments provides a general measure of the goodness-of-fit of the lognormal model. Therefore, the estimated nonpartitioning tracer third moments are also shown in Table 2-5. Note that the discrepancy between these measures was less than 0.5% for each experiment. Also note the close agreement of the nonpartitioning tracer moments between experiments, indicating relatively consistent hydrodynamics. The relative agreement between the measured and modeled nonpartitioning tracer BTCs provided an additional check on the appropriateness of using a single lognormal distribution to describe solute transport in the laboratory experiments. For all experiments, the modeled nonpartitioning tracer concentration profiles fit the measured BTCs well (see Figures 2-8 and 2-9; note that these figures are plotted on log scale).

Partitioning tracer transport. The measured partitioning tracer BTCs from all seven experiments are shown in Figures 2-7a (E3-E6) and 2-7b (E7, E4, E2, and E1), where each BTC was scaled to its zeroth moment. Note that the partitioning tracer BTCs were bimodal, as was expected from the numerical simulations described above.

The tracer transport behavior in E3, E4, E5, and E6 (Figure 2-7a) was very similar, despite the fact that these experiments were conducted with tracer C_0 values ranging from approximately 3 to 18% of aqueous solubility. As demonstrated by Wise (1999), the effects of isotherm nonlinearities would be expected to increase with C_0. The results presented here, therefore, indicate that partitioning isotherm nonlinearities were not a significant concern in these experiments. However, the results presented in Figure 2-7b, which are from

□ 0.5 Co   △ Co   ▽ 2 Co   × 3 Co

□ 1.4 m/d   △ 2.9 m/d   ▽ 8.7 m/d   × 17.3 m/d
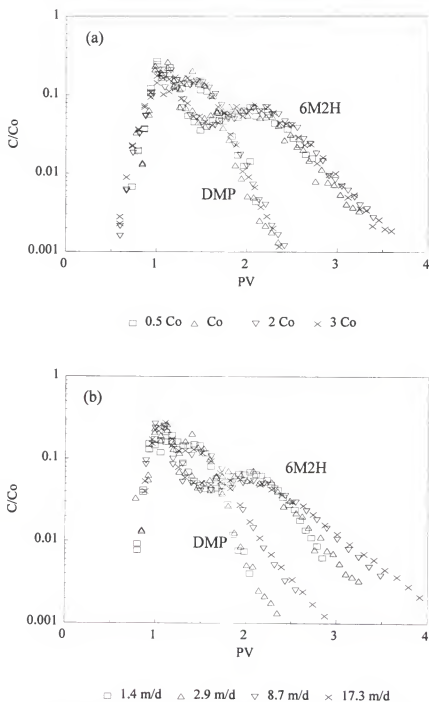
Figure 2-7. Partitioning tracer BTCs measured from experiments with (a) equivalent velocities, $v = 2.9$ m/d, but varying tracer initial concentrations (E3, E4, E5, and E6), and (b) equivalent initial concentrations, approximately 6% of aqueous solubility, but varying velocities (E7, E4, E2, and E1).

experiments conducted at four different pore water velocities, indicate that nonequilibrium partitioning likely was a factor in these experiments. Note that the degree of spreading in the second mode of the BTCs in Figure 2-7b increased with pore water velocity, as would be expected for rate-limited sorption, or partitioning (e.g., Valocchi, 1985).

The first three temporal moments from the partitioning tracer BTCs measured during E1, E2, E4, and E7 are presented in Table 2-6 (because the results from the experiments conducted at different C_0 values were approximately equivalent, only one of these, E4, was considered further). Note that for both tracers, m_2 and m_3 decreased with pore water velocity, in accordance with the observation that the spreading of the partitioning tracer BTCs decreased with velocity. Also note that in every case, except 6M2H in E4, m_1 decreased with pore water velocity. Valocchi (1985) demonstrated that m_1 should be independent of velocity, even under nonequilibrium conditions, assuming that the rate constant, k_2, is independent of velocity. Therefore, these results suggest that k_2 may be velocity-dependent for the experiments described here.

Estimation of f and S_N. Estimates of the S_N distribution parameters were determined for E1, E2, E4, and E7 using both the homogeneous and distributed binary models (Table 2-6). Note that the estimated S_N values were uniformly lower than the true value (this remained the case even when differences between the measured and estimated f values were considered). This may have been because the actual volume of NAPL that was emplaced in the flow chamber was less than 7.7 mL (evidenced by the aforementioned residue in the mixing beaker), or because the effective K_N values that were realized were lower than the

Table 2-6. Measured partitioning tracer moments and estimated NAPL distribution model parameters for each laboratory experiment.

Tracer [a]	Measured Moments [b]			Homogeneous Model		Distributed Model		
	m_1	m_2	m_3	f	S_N	f	S_N [c]	$\sigma_2 \div \sigma_1$ [d]
E1 (v_n)								
DMP	1.324	1.870	2.851	0.39	0.051	0.51	0.039	2.12
6M2H	1.641	3.170	7.221	0.42	0.051	0.54	0.040	2.90
E2 ($v_n/2$)								
DMP	1.311	1.838	2.764	0.38	0.049	0.43	0.045	1.45
6M2H	1.564	2.895	6.244	0.37	0.050	0.42	0.045	1.86
E4 ($v_n/6$)								
DMP	1.277	1.700	2.358	0.49	0.034	0.50	0.034	1.05
6M2H	1.578	2.806	5.575	0.48	0.040	0.56	0.036	1.87
E7 ($v_n/12$)								
DMP	1.265	1.663	2.268	0.52	0.031	0.59	0.028	1.21
6M2H	1.549	2.653	4.982	0.54	0.034	0.59	0.032	1.64

[a] Initial concentrations, C_0, were equal for each experiment (see Table 2-5). [b] Moment estimates obtained from the homogeneous and distributed binary models were very close to the measured values (generally within 1%) and are not shown. Units are PV^N. [c] Determined from m_1^S and $S_N = S/(1 + S)$. [d] Ratio of the σ values for the second and first modes of the partitioning tracer BTCs; indicative of the degree of 'excess' spreading.

batch-measured values. However, the estimates for f and S_N are independent and errors in K_N would be reflected only in S_N, and not f.

The homogeneous binary model parameters were determined by algebraic solution of (2-37) and (2-38) and the model BTCs generated with these parameters are compared to the measured BTCs in Figure 2-8. Note that the model fits improved as the pore water velocity decreased, with quite close matches obtained for DMP at the lowest velocities. As pore water velocity decreases, residence time increases and conditions at the local scale approach equilibrium. Thus the inherent model assumption of instantaneous partitioning is most closely approximated, and the resulting model BTCs most closely match the data, at low velocities. Inspection of the BTCs in Figure 2-8 indicates that, at a given velocity, the partitioning of DMP appeared to be closer to equilibrium than 6M2H, which implies that k_2 for DMP was greater than that of 6M2H. This result is consistent with the observations of Brusseau and Rao (1989) and Augustijn (1993) of an inverse relationship between the sorption, or partitioning, rate constant and partitioning coefficient (also see Chapter 4).

The distributed binary model was also applied to the measured data. The resulting model parameters, determined from solution of (2-44)-(2-46), are listed in Table 2-6 and the corresponding model fits are compared to the measured BTCs in Figure 2-9. While the flow chamber was packed such that the NAPL saturation within the contaminated zone would be relatively homogeneous, and the results discussed above indicated that, at low velocities, the homogeneous binary model adequately described the transport of partitioning tracers, it was desired to investigate whether the application of the distributed binary model would provide equally adequate, or even improved, parameter estimates and fits to the data. However,
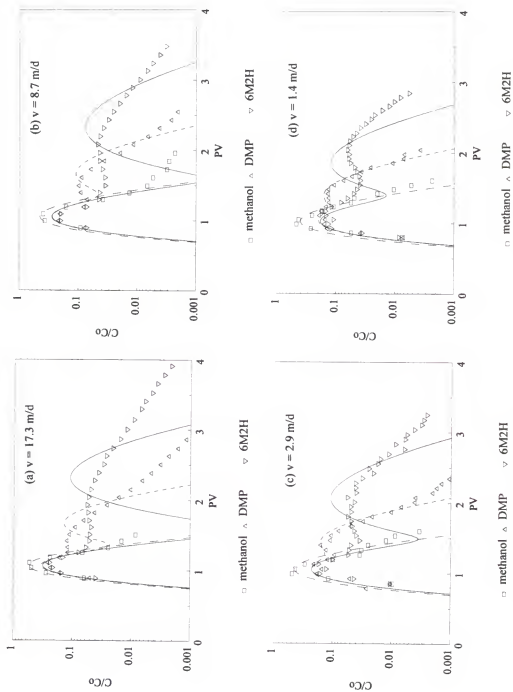
Figure 2-8. Measured nonpartitioning and partitioning tracer BTCs from (a) E1, (b) E2, (c) E4, and (d) E7, each shown with the homogeneous binary model fit.

68
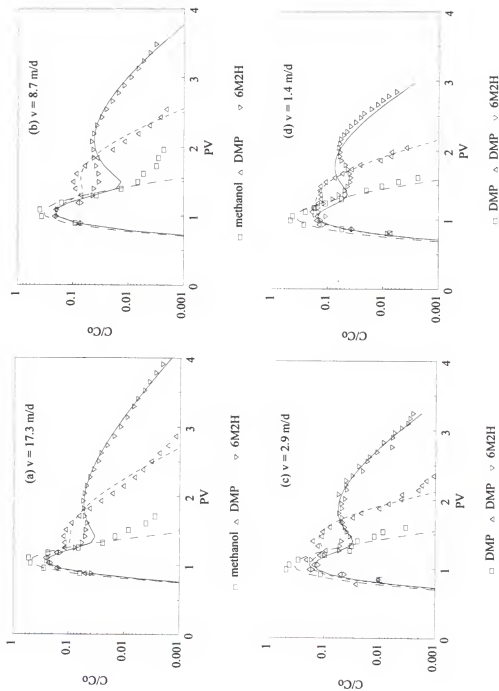
Figure 2-9. Measured nonpartitioning and partitioning tracer BTCs from (a) E1, (b) E2, (c) E4, and (d) E7, each shown with the distributed binary model fit.

because, in this case, the excess spreading that was realized in the partitioning tracer BTCs was due to rate-limited partitioning, and not a nonhomogeneous NAPL distribution, it is emphasized that the resulting parameters, μ_S and σ_S, should be considered as generally descriptive of the degree of excess BTC spreading, rather than as specifically descriptive of the distribution of NAPL within the contaminated zone. When this concession is made, the information that can be gleaned from the distributed binary model that is descriptive of the NAPL saturation distribution is reduced to that of the homogeneous binary model, namely f and S_N.

Comparison of the model fits in Figure 2-9 to those in Figure 2-8 indicates that, at each velocity, the distributed binary model provided better fits to the measured data than did the homogeneous binary model. The ratio of the lognormal distribution σ values from the second and first modes of the partitioning tracer BTCs is a measure of the degree of excess spreading in the contaminated zone compared to the uncontaminated zone. The nonpartitioning tracer σ values reported in Table 2-5 were used for the first mode, while the second mode values were determined from (2-20), (2-50), and (2-51), as described above. For each experiment, the ratio $\sigma_2 \div \sigma_1$ is listed in Table 2-6. Note that this ratio generally decreased with velocity except at the lowest velocity. The decreasing trend with velocity is consistent with other observations indicating that partitioning was rate-limited. Also note that at the lowest velocity (E7) the model fit for 6M2H was worse than at the other flow rates (Figure 2-9), and the estimated f values were farther from the true value than at the other flow rates (Table 2-6). This result is contrary to the expectation that the model fits should

improve as chemical equilibrium is approached (as was observed with the homogeneous binary model).

An explanation for the poor fit of the model to the E7 BTCs can be surmised by noting that the spreading of the first mode of the 6M2H BTC was greater than that of the methanol BTC (Figure 2-9d). This observation was quantitatively verified by fitting the measured partitioning BTCs with the superposition of two lognormal distributions (not shown), resulting in ratios of the partitioning tracer σ_1 to the single-mode methanol σ of 1.08 and 1.46 for DMP and 6M2H, respectively. At very low velocities, advection becomes less dominant over diffusion as a transport mechanism (the role of diffusion as a rate-limiting step in sorption, partitioning, and dissolution processes is also discussed in Chapter 4), and diffusion-limited processes approach equilibrium. It is suggested that, at velocities that are low enough to allow for equilibrium partitioning, diffusion between the contaminated and uncontaminated zones may become non-negligible. At a given time, the partitioning tracers that are retarded in the contaminated zone have not traveled as far as the tracers in the uncontaminated zone. Therefore, a concentration gradient exists across the boundary between the adjoining zones, and the resulting diffusion produces excess spreading in the portion of the partitioning tracer BTC that is nominally representative of the uncontaminated zone.

Finally, the effects of flow bypassing were considered. However, because of the relatively low NAPL saturations in the contaminated zone in these experiments, these effects were minor. Combination of (2-27) and (2-28) with $\zeta = 2$ and the f and S_N values in Table 2-6 resulted in corrections to f of approximately 2-3%. For example, correction of the flux-

averaged value of f given in Table 2-6 for DMP in E1 to a volume-averaged value resulted in an increase from 0.39 to 0.40.

<u>Discussion</u>

These laboratory experiments investigated the relative contributions of nonuniform NAPL distribution, partitioning isotherm nonlinearity, and nonequilibrium partitioning to excess spreading of partitioning tracer BTCs. Partitioning isotherm nonlinearity appeared to have minimal effect over a tracer concentration range of approximately 3% to 18% of aqueous solubility. The effects of nonequilibrium partitioning, however, were observed over a broad range of pore water velocities. Generally, local conditions are closer to equilibrium at lower velocities and excess spreading due to nonequilibrium partitioning decreases. However, as velocities approach zero, the effects of molecular diffusion become non-negligible. In cases where the NAPL distribution is nonuniform, tracer concentration gradients may exist across streamtubes leading to enhanced BTC spreading from molecular diffusion. Because partitioning rate constants are a function of K_N, the velocities required to achieve local equilibrium will be different for different tracers. Therefore, when multiple partitioning tracers are used in systems with nonuniform NAPL distributions, it is probable that some degree of nonequilibrium effects, on either a local (i.e., pore) or multiple streamtube scale, can be expected regardless of velocity.

In these experiments, the NAPL was relatively homogeneously distributed within the contaminated zone, but because of nonequilibrium effects, the distributed binary model provided better fits to the data than the homogeneous binary model. In these cases, the

estimated parameter σ_S is not representative of the standard deviation of the NAPL saturation distribution, but rather can be considered as a general parameter that accounts for the spreading of the partitioning tracer BTC. The values of f and S_N that were estimated using both the homogeneous and distributed binary models were relatively close to the measured values for these experiments. However, because these models are based on the assumption of instantaneous partitioning, our ability to estimate NAPL saturation distribution parameters may be restricted until nonequilibrium effects are specifically considered.

Application of Models to Field Data

The distributed binary model was applied to data from field-scale partitioning tracer tests conducted at two different sites. The first field experiment–conducted at Hill AFB, UT–is described in detail in Chapter 3, while the second study–conducted at the site of a former dry cleaner in Jacksonville, FL–is described in Sillan (1999).

Background and Methods

The two field sites were contaminated with different types of NAPL, leading to different NAPL saturation distributions. At Hill AFB, the multicomponent NAPL was less dense than water, while the primary contaminant at the Jacksonville site, tetrachloroethylene (also called perchloroethylene, PCE), was denser than water. These contaminants can be generally categorized as light and dense NAPLs (LNAPLs and DNAPLs), respectively.

Light NAPLs float on the water table, often creating smear zones as the water table fluctuates seasonally. At the Hill AFB site, the mean water table position was only

approximately 1 m above a clay confining unit at 8 m below ground surface (bgs), and soil core data indicated a NAPL smear zone extending from the clay to approximately 5 m bgs (see Chapter 3). The Hill AFB experiments were conducted within a hydraulically isolated sheet pile test cell, enabling manipulation of the water table. During the partitioning tracer tests, the water table in the test cell was maintained at approximately 5 m bgs in order to capture the entire NAPL smear zone. Thus, it was expected that most of the streamtubes within the test cell would intercept some NAPL ($f \approx 1.0$).

At the Jacksonville site, the areal and vertical extent of the NAPL source zone was less clear. Soil cores indicated a NAPL source zone between 7 and 10 m bgs that consisted of thin layers of separate phase PCE that did not appear to be horizontally continuous (Sillan, 1999). Example soil concentration profiles are presented in Figure 2-10. These data illustrate that much of the aquifer was uncontaminated, but the fraction of horizontal trajectories intercepting some amount of NAPL was likely greater than the value of f that might be expected from the examination of individual borings. There were no sheet pile walls at the Jacksonville site. Also, the confining clay layer (approximately 11 m bgs) and the water table (approximately 3 m bgs) did not strictly bound the NAPL source zone, as in the Hill AFB study. Therefore, it was likely that some of the tracer solution followed streamlines through portions of the aquifer that were either above or below the NAPL source zone. Thus, while an accurate *a priori* estimate of the fraction of the streamtubes that might have intercepted some NAPL was not possible, it was estimated that a measurable fraction of the streamtubes would be uncontaminated (i.e., $f < 1.0$).
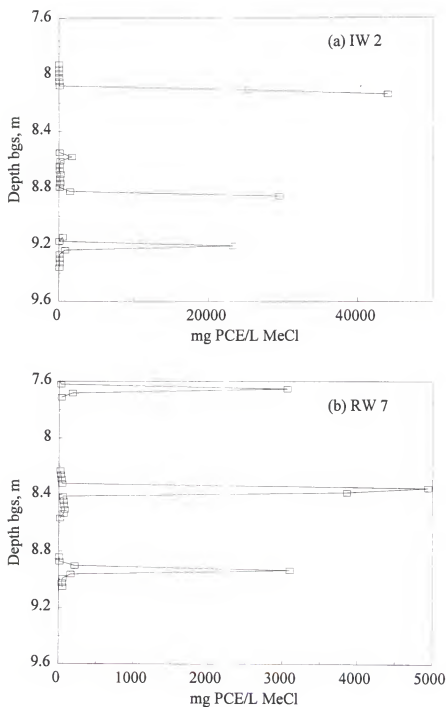
Figure 2-10. Example PCE soil concentration profiles from the Jacksonville, FL field site for samples collected during the installation of (a) an injection well, and (b) a recovery well. Adapted from Sillan (1999).

Methanol was used as the nonpartitioning tracer at both sites and the partitioining tracers were DMP (K_N = 10.7) and 2-ethyl-1-hexanol (EHex, K_N = 74) at the Hill AFB and Jacksonville sites, respectively. Both studies were conducted at flow rates that were equivalent to approximately 1 PV per day. Only one set of nonpartitioning and partitioning tracer BTCs are presented here for each study. The Jacksonville results are from a recovery well labeled RW 7, while the Hill AFB results are from the flux-average of the BTCs measured at all three extraction wells, representing information integrated over the entire test cell volume.

<u>Field Results</u>

The first three temporal moments of the nonpartitioning and partitioning tracer BTCs measured during both studies are presented in Table 2-7 (units are d^N). The measured BTCs were truncated because of the dual limitations of analytical detection and experiment duration, as described above, and the values listed in Table 2-7 are the complete moment estimates obtained using the truncated lognormal distribution approach with the superposition of two lognormal distributions.

Nonpartitioning and partitioning tracer CDFs–determined by scaling the measured BTCs to their zeroth moments and integrating–from both field studies are presented in Figure 2-11 along with the model fits for each. For both studies, accurate modeling of the nonpartitioning tracer transport required the superposition of two lognormal distributions and the resulting lognormal parameters are listed in Table 2-7 (note that these parameters are equivalent to those used to calculate the complete moments because the complete moment

Table 2-7. Nonpartitioning and partitioning tracer moments and NAPL saturation distribution parameters for the Hill AFB, UT and Jacksonville, FL field tracer experiments.

Tracer	Moments [a]			Lognormal Model Parameters [b]				
	m_1	m_2	m_3	μ_1	σ_1	F/f	μ_2/μ_S	σ_2/σ_S
Hill AFB, UT								
Methanol	1.242	2.985	16.36	-0.188	0.444	0.807	0.712	0.704
DMP	2.117	8.666	75.39	-	-	1.0	-2.69	0.100
Jacksonville, FL								
Methanol	1.062	2.329	10.36	-0.865	0.193	0.201	-0.127	0.809
EHex	1.422	4.481	28.79	-	-	0.650	-4.89	0.066

[a] Units are d^N. [b] Subscripts 1 and 2 refer to the first and second modes of the superposition of two lognormal distributions used to model the nonpartitioning tracer data, where F is the fractional contribution of the first mode. The NAPL saturation distribution parameters f, μ_S, and σ_S were determined from the partitioning tracer moments using (2-44)-(2-46).
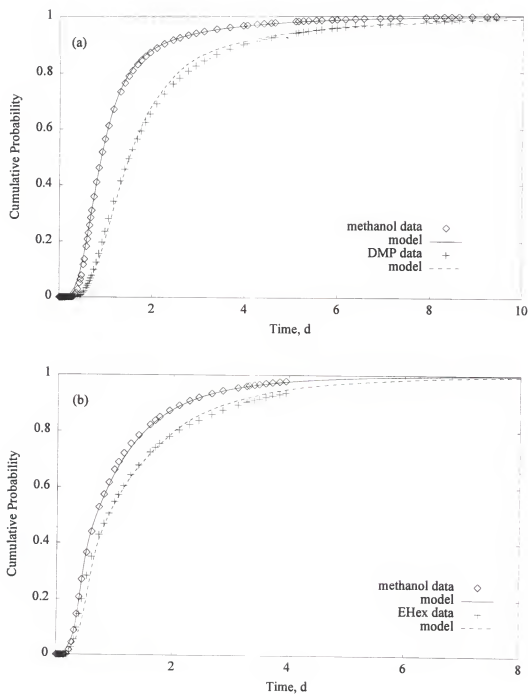
Figure 2-11. Measured nonpartitioning and partitioning tracer CDFs with model fits for the (a) Hill AFB, UT and (b) Jacksonville, FL field studies.

estimates were also obtained from the superposition of two lognormal distributions). The NAPL saturation distribution parameters (Table 2-7) were determined for each study from (2-44)-(2-46) by minimizing the RMSD between the measured and estimated values for the first three normalized temporal moments of the partitioning tracer BTC. Exact solution of (2-44)-(2-46) was not possible for these data, presumably because of the bi-continuous nature of the nonpartitioning tracer BTCs. In the absence of data supporting a correlation between K and S_N, and in consideration of the damping effect of media heterogeneity and flow geometry, $\rho_{t,S}$ was assumed to be equal to zero for both field sites.

As discussed above, the bi-continuous nonpartitioning tracer BTCs also complicated the generation of the partitioning tracer model fit. Model CDFs were generated using the methodology described above and were compared to the measured partitioning tracer CDFs. Note that for both studies, the partitioning tracer CDFs that resulted from the application of the distributed binary model closely matched the measured data.

As discussed in relation to the laboratory experiments, it is suggested that σ_S should not be interpreted as strictly representative of the NAPL saturation distribution, but instead should be interpreted as a general measure that incorporates the combined effects of nonuniform NAPL distribution within the contaminated fraction of the domain, nonequilibrium and nonlinear partitioning, and correlation between NAPL saturation and media properties. Also, note that, as discussed in relation to the two-dimensional particle tracking simulations, σ_S is representative of the variability in the integrated streamtube-average NAPL saturation distribution, which is likely to be much less variable than the point distribution. For example, the CDF generated by integrating (2-14), using the Hill AFB μ_S

and σ_S values (Table 2-7), is compared in Figure 2-12 to the CDF generated from 59 soil

samples collected within the Hill AFB flushed zone (see Chapter 3). Note that both CDFs

have been scaled to their respective means to illustrate their disparate variances. The soils

data CDF was based on n-undecane soil concentrations, which should have been similar to

the NAPL saturation distribution, assuming a relatively homogeneous NAPL composition

within the test cell (CDFs for different NAPL constituents were similar to that shown in

Figure 2-12). Note that, as shown in the numerical simulations, the variability of the point

data was much greater than that of the integrated measure.

The relatively small σ_S values that were determined for both field sites indicated that,

within the contaminated zone, the NAPL saturation distributions were not particularly

variable. It, therefore, should not be surprising that application of the homogeneous binary

model to these data produced model fits (not shown) that were very close to those presented

in Figure 2-11, with NAPL distribution parameters that were only slightly different from

those in Table 2-7 ($f = 1.0$ and 0.47, and $S_N = 0.064$ and 0.010 for the Hill AFB and

Jacksonville sites respectively). These data suggest that accurate characterization of

nonpartitioning tracer transport (e.g., through the superposition of multiple transport

equations) and the fraction of the domain that is contaminated (using either the homogeneous

or distributed binary models) may be sufficient to adequately characterize partitioning tracer

transport, and thus the NAPL saturation distribution, even when the impact of other factors

such as nonequilibrium partitioning and correlations between K and S_N are ignored. Finally,

it is emphasized that the estimated f values for both sites were consistent with qualitative

expectations based on the type of NAPL and the flow geometry at each site.
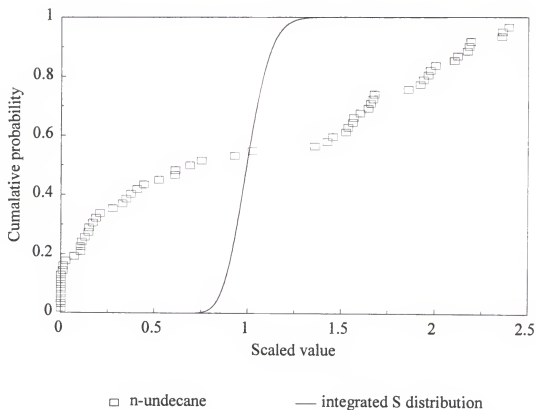
Figure 2-12. Comparison of CDFs from the Hill AFB, UT *n*-undecane soil core point data and the estimated streamtube-average *S* distribution. Both CDFs have been scaled to their respective means.

CHAPTER 3
FIELD-SCALE AQUIFER REMEDIATION:
SINGLE-PHASE MICROEMULSION (SPME) FLUSHING

Introduction

Recently, many investigators have demonstrated that in situ flushing techniques show promise for the remediation of aquifers contaminated with nonaqueous phase liquids (NAPLs), such as fuels and chlorinated solvents, in time frames much smaller than would be expected for traditional pump-and-treat methods (Falta et al., 1996; Fountain et al., 1996; Rao et al., 1997). Similar to enhanced oil recovery (EOR) (e.g., Shah, 1981; Lake, 1989), these flushing technologies generally involve the addition of chemical agents to an injection fluid during either miscible or immiscible displacements to accelerate the dissolution or displacement of NAPLs from contaminated aquifers. Two classes of chemical agents used for in situ flushing which have been the focus of much study are cosolvents (Peters and Luthy, 1993; Brandes and Farley, 1993; Augustijn et al., 1994; Imhoff et al., 1995) and surfactants (Abdul et al., 1992; West and Harwell, 1992; Pennell et al., 1993; Fountain et al., 1996; Shiau et al., 1996).

Both cosolvent and surfactant solutions can be used to accelerate the removal of residually-trapped NAPLs from porous media through either mobilization or enhanced solubilization. Mobilization of NAPL trapped within the porous media by capillary forces

81

is facilitated by a reduction in the interfacial tension (IFT) between the NAPL and the flushing solution as either a cosolvent or surfactant solution displaces the resident groundwater and contacts NAPL ganglia. Similarly, solubilization of the NAPL is enhanced due to the reduced polarity of the flushing solution, compared to that of the resident groundwater.

Several laboratory and field mobilization studies have shown that a large percentage of the NAPL trapped in contaminated porous media, often > 95%, can be removed after injecting a small number of pore volumes (PV) of flushing fluid (e.g., Pennell et al., 1996; Sabatini et al., 1996). However, mobilization technologies are limited to sites where the flow of the mobilized NAPL can be controlled and the potential for migration of NAPL through layers that previously acted as capillary barriers can be assured. Remediation technologies which rely on solubilization generally do not remove the NAPL as efficiently as mobilization technologies. However, solubilization technologies generally pose less risk with regard to uncontrolled migration of the mobilized NAPLs and are less complex to design, particularly with regard to the number of parameters requiring optimization. It is for these reasons that the focus of the group at the University of Florida (UF) has been on developing aquifer remediation strategies which solubilize NAPLs without inducing mobilization (Rao et al., 1991; Augustijn et al., 1994; Ouyang et al., 1996; Rhue et al., 1999).

The results reported here are from a field-scale aquifer remediation study conducted in a surficial aquifer contaminated with a complex NAPL mixture, wherein NAPL solubilization without mobilization was the goal. This study was one of eight pilot-scale tests funded by the Strategic Environmental Research and Development Program (SERDP)

and the Advanced Applied Technology Demonstration Facility (AATDF), and conducted side-by-side at Hill Air Force Base (AFB), Utah for the purpose of evaluating in situ flushing remediation technologies for the removal of NAPLs from subsurface environments. In 1995, UF and the U.S. Environmental Protection Agency (EPA) conducted a field-scale evaluation of in situ cosolvent flushing within the same contaminant source zone at Hill AFB (Rao et al., 1997; Annable et al., 1998; Sillan et al., 1998), wherein the flushing solution (70% ethanol, 12% *n*-pentanol, and 18% water by volume) was designed to solubilize the NAPL. In this second solubilization study, the objective was to achieve high NAPL solubilization efficiencies with a lower concentration of chemical additives in the flushing solution than was required in the cosolvent flushing experiment. A surfactant/alcohol mixture was used to generate a Winsor Type I system, where the NAPL was solubilized and transported as a single-phase microemulsion (SPME). For the SPME process, only 5.5 wt % of the flushing solution was comprised of chemical additives.

The SPME flushing study was conducted in a hydraulically-isolated test cell (2.8 m × 4.6 m), similar in design to that described by Rao et al. (1997). The amount and spatial distribution of residual NAPL within the test cell were determined both before and after SPME flushing using soil cores and interwell partitioning tracer tests (Jin et al., 1995; Annable et al., 1998). During the SPME flood, fluid samples were regularly collected from extraction wells and multilevel samplers and were analyzed for target NAPL constituents. Each of these data sets was used to evaluate the performance of the SPME flushing experiment in terms of both the NAPL removal effectiveness, defined as the fraction of the initial amount of contaminants present that was removed by the remediation technology, and

the NAPL removal efficiency, defined as the amount of NAPL removed divided by a measure of the volume of flushing fluid applied. Also, the performance of the SPME flood was compared to that of the 1995 cosolvent flood using the same performance measures.

Technology Description

A microemulsion is an optically transparent dispersion of liquid droplets (< 0.1 μm) suspended within a second, immiscible liquid stabilized by an interfacial film of surface-active molecules (Rosen, 1989). Generally, the stabilizing interfacial film is comprised of both a surfactant and a cosurfactant (such as an intermediate chain-length alcohol). Varying a parameter which changes the character of the system from hydrophilic to lipophilic will produce a phase transition from an oil-in-water microemulsion (oil, or NAPL, droplets in a water-continuous phase; Winsor Type I), to a water-in-oil microemulsion (water droplets in an oil phase; Winsor Type II). Winsor Type III systems are formed mid-way in the transition from hydrophilic to lipophilic systems. At the transition to a Winsor Type III system the IFTs between the microemulsion phase, also known as the middle phase, and any excess oil or water phases present reach extreme minimums, much lower than those achieved in Winsor Type I and II systems. It is because of these ultra-low IFTs that middle-phase microemulsions have been promoted for both EOR (Shah, 1981; Lake, 1989) and aquifer remediation via NAPL mobilization (Baran et al., 1994; Sabatini et al., 1996; Shiau et al., 1996). However, middle-phase systems can be difficult to design in field settings because of the relatively large number of parameters requiring optimization (e.g., salinity, surfactant

concentration, and aquifer geochemical conditions) (Pithapurwala et al., 1986; Sabatini et al., 1996).

Martel and collaborators (Martel et al., 1993; Martel and Gélinas, 1996) proposed the use of Winsor Type I microemulsions to solubilize NAPLs without mobilization. These systems have the advantages of high solubilization of NAPLs (although not as high as middle-phase microemulsions) with relatively low amounts of chemical additives required. Huh (1979) showed that in microemulsions, solubilization of the oil phase into the microemulsion is related to interfacial tension by an inverse-squared relationship. Therefore, remediation systems which rely on Winsor Type I microemulsification will necessarily be less efficient than those that rely on Winsor Type III microemulsions and mobilization, since solubilization will be lower at the higher interfacial tensions required to prevent mobilization.

The mechanisms of aqueous solubilization, micellar solubilization, and microemulsification are contrasted in the conceptual diagram shown in Figure 3-1. In aqueous solubilization, individual molecules of NAPL constituents dissolve in the water (Figure 3-1a). In the presence of surfactant micelles, solubilization is enhanced as NAPL constituent molecules are scavenged from the aqueous solution (Figure 3-1b). Rather than solubilizing individual constituent molecules, microemulsions, through a reduction of interfacial tension, are able to encapsulate tiny droplets of the NAPL itself (Figure 3-1c).

(a) Aqueous Solubilization
(Pump and Treat)

(b) Micellar Solubilization

(c) **Microemulsification**: low interfacial tension
Surfactant   - 3% Brij 97® [C$_{18}$O(C$_2$H$_4$O)$_{10}$H]
Cosurfactant - 2.5% n-pentanol
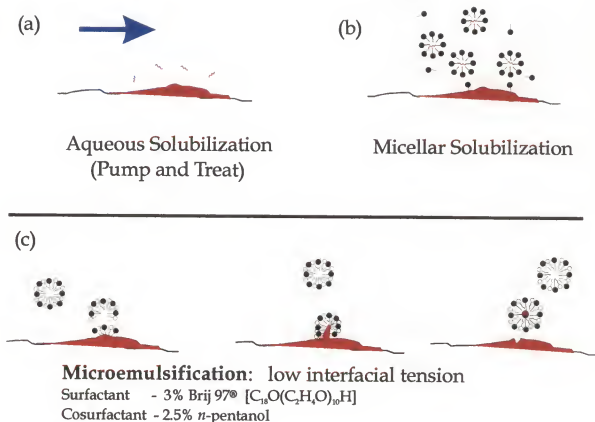
Figure 3-1. Conceptual comparison of (a) aqueous solubilization, (b) micellar solubilization, and (c) microemulsification. Solid circles indicate surfactant molecules, open circles indicate cosurfactant molecules and squiggles indicate NAPL constituent molecules.

Laboratory Investigations

The NAPL used in the laboratory phase of this study was free product taken in June, 1995 from a monitoring well (OU1-202) located approximately 25 m northwest of the test cell at Hill AFB. It had a viscosity of 10.7 cp and a density of 0.85 g/cm^3 at 24°C. Of the approximately 200 constituents that have been identified in the NAPL at Hill AFB (Montgomery Watson, 1995) nine target analytes were selected for monitoring the presence of NAPL in aqueous microemulsions. These nine compounds are listed in Table 3-1 along with their respective mass fractions in the NAPL. Also listed in Table 3-1 are the mass fractions of the nine target compounds in a free product NAPL sample taken in June, 1996 from a monitoring well (labeled MW-2 in Table 3-1) located approximately 2 m north of the test cell at Hill AFB. It had a density of 0.88 g/cm^3 at 24°C. The spatial compositional heterogeneity of the Hill NAPL is indicated by the different compositions of the two samples. While the OU1-202 NAPL was used for the laboratory phase of this project, the MW-2 NAPL was collected very near the field test cell and was thus used for determining NAPL composition for the field phase of the study.

The first phase of this study was to select a surfactant and cosurfactant, which together form the microemulsion precursor, that would produce a low-viscosity, single-phase microemulsion on contact with the multicomponent NAPL found at the field site. Rhue et al. (1999) screened 86 surfactants and 3 alcohols, with maximum NAPL solubilization and low-viscosity (< 2 cp) as the main acceptance criteria. The viscosity of the precursor solution was limited to preclude large hydraulic gradients across the test cell and excessive drawdown around the extraction wells. The precursor solution selected was the surfactant

Table 3-1. Mass fractions and octanol-water partitioning coefficients of target NAPL constituents.

NAPL Constituent	Mass Fraction, X_i [b] (g/100 g NAPL)		$\log K_{ow}$ [c]
	OU1-202	MW-2	
[a]p-xylene	0.892	0.144	3.15
1,2-dichlorobenzene	1.66	NM	3.40
[a]1,2,4-trimethylbenzene	1.08	0.438	3.63
naphthalene	0.055	NM	3.35
1,2,4-trichlorobenzene	0.62	0.461	4.10
[a]n-decane	2.14	0.477	6.25
[a]n-undecane	1.32	1.573	6.53
[a]n-dodecane	0.680	0.698	6.80
[a]n-tridecane	0.510	0.285	7.40

[a] NAPL constituents emphasized in this analysis. [b] Measured by dissolving NAPL collected from the field site in hexane and analyzing by gas chromatograph with flame ionization detection. [c] From Sangster (1989), except 1,2-dichlorobenzene and 1,2,4-trichlorobenzene, which were from Abernethy et al. (1988), and n-undecane and n-tridecane, which were estimated based on linear interpolation. NM = not measured.

Brij 97 (polyoxyethylene (10) oleyl ether) at 3 wt % and *n*-pentanol at 2.5 wt % in water.

Rhue et al. (1999) found that upon equilibration of the SPME precursor solution with the

OU1-202 NAPL, the dissolved concentration of dodecane was 104 mg/L, compared to an

expected aqueous concentration of 2.5×10^{-5} mg/L (based on an aqueous solubility of 0.0037

mg/L and a mass fraction in the NAPL of 0.680 wt %, Table 3-1). Greater NAPL

solubilization could be achieved with higher concentrations of surfactant and cosurfactant.

However, increased solubilization would be accompanied by a concomitant increase in

viscosity. The field-measured viscosity of the precursor was 1.66 cp, while the viscosity of

tap water at the same ambient temperature (approximately 32°C) was measured to be 0.87

cp.

As suggested by Figure 3-1, when a multicomponent NAPL is emulsified, the relative

proportions of the NAPL constituents in the microemulsion should be the same as those in

the NAPL itself. This is contrasted to dissolution processes, wherein more soluble NAPL

constituents would be selectively dissolved in preference to less soluble constituents.

Chromatograms, measured by gas chromatography (GC), of OU1-202 NAPL in a hexane

solution and in an aqueous microemulsion formed with the SPME precursor are compared

in Figure 3-2. Peaks associated with the nine target analytes as well as hexane and *n*-

pentanol are identified. The NAPL was completely dissolved in the hexane solution,

whereas the microemulsion was formed in the presence of excess NAPL. Except for the

hexane and pentanol peaks, the two chromatograms are similar and indicate little

solubilization selectivity in the microemulsion phase with respect to the nine target analytes.

Lack of selectivity is also demonstrated in Figure 3-3, where the concentrations of target
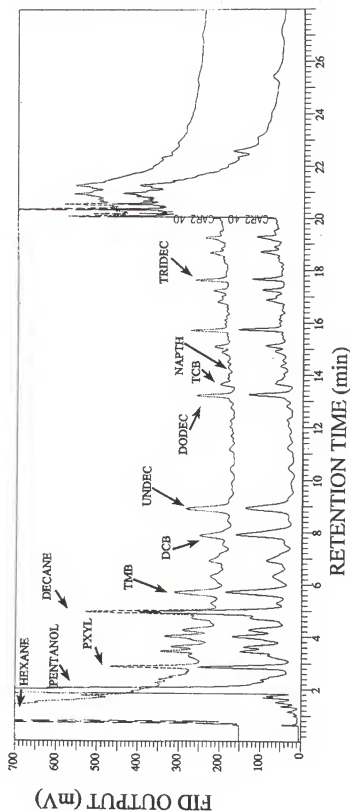
Figure 3-2. Comparison of chromatograms for OU1-202 NAPL from Hill AFB completely dissolved in hexane (upper) with an aqueous microemulsion formed with a Brij 97/n-pentanol solution in the presence of excess NAPL (lower).
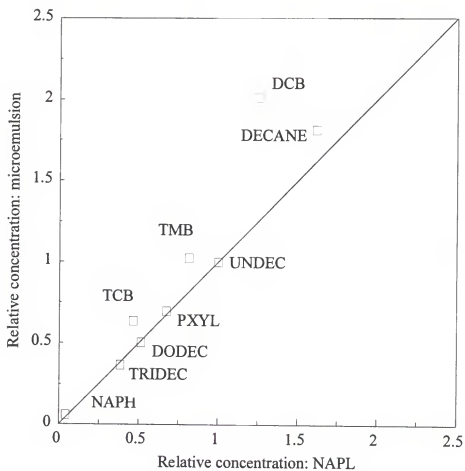
Figure 3-3. Concentrations of target analytes, relative to *n*-undecane, in the OU1-202 NAPL and in a Brij 97/*n*-pentanol microemulsion (adapted from Jawitz et al., 1997a and Rhue et al., 1999).

analytes in the microemulsion, relative to that of *n*-undecane are plotted against relative concentrations in the NAPL. With the possible exception of 1,2-dichlorobenzene (DCB), which tended to be present in the microemulsion phase at a slightly higher concentration, relative to *n*-undecane, than it was in the NAPL, it appears that selectivity was negligible. These results suggest true emulsification of the multicomponent NAPL by the SPME precursor solution.

<u>Field Site Characterization</u>

<u>Field Site Background</u>

A brief summary of the field site history and geohydrology follows; greater detail can be found in a report written for Hill AFB by Montgomery Watson, Inc. (1995). Hill AFB is located approximately 50 km north of Salt Lake City, UT at the western foot of the Wasatch Mountain Range. The field site was located in a NAPL source zone within a shallow surficial aquifer which is located on the Weber Delta, approximately 100 m above the Weber River valley. The aquifer material consists of sand and gravel (Provo Formation), with a thick (> 60 m) clay aquitard (Alpine Formation) approximately 8 m below ground surface (bgs). The aquifer was contaminated through the use of two chemical disposal pits in the 1940s and 1950s. A variety of liquid wastes such as fuels, waste oils, and spent solvents from degreasing operations were disposed of in these pits. Migration over the years has caused spreading of the NAPL source zone to an area of approximately 2.8 ha. A schematic diagram of the field site is presented in Figure 3-4, illustrating the locations of the eight SERDP/AATDF test cells, the 1995 UF test cell, and the chemical disposal pits.
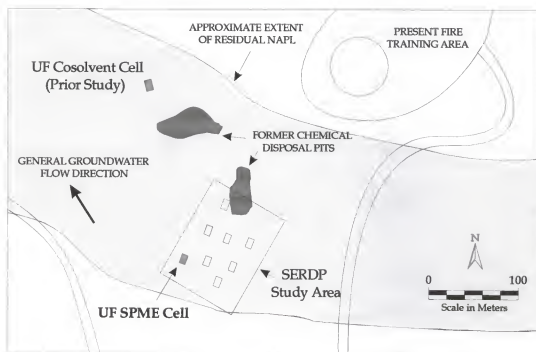
Figure 3-4. Locations of the SERDP/AATDF test cells within the NAPL source zone at Operable Unit 1, Hill AFB, Utah.

The NAPL collected from wells at the site was a very hydrophobic mixture which tended to strongly coat solid surfaces. Contaminated aquifer solids collected from within the test cell appeared to be completely coated with the NAPL. However, free phase NAPL samples collected at the site were completely miscible with both hexane and methylene chloride. Because the NAPL density was less than that of water, it was generally found at or above the water table. While the seasonal water table was at approximately 7 m bgs at the time these experiments were conducted (May - August 1996), periodic water table fluctuations since the contamination events have created a NAPL smear zone extending up approximately 3 m from the clay layer (i.e., 5 m to 8 m bgs). For the experiments reported here, the water table within the cell was maintained at 4.9 m bgs in order to capture the entire NAPL smear zone within the flow domain.

Test Cell Design and Instrumentation

The design of the eight hydraulically-isolated test cells at the SERDP site was similar to that of the cell which was built for the 1995 UF/EPA cosolvent flushing project at Hill AFB (Rao et al., 1997; Annable et al., 1998; Sillan et al., 1998). Each cell was constructed using 9.5 mm thick interlocking steel sheet piles with grouted joints, enclosing rectangular areas of approximately 2.8 m × 4.6 m and penetrating from the ground surface to approximately 3.7 m into the clay confining unit. The Z-shape of the individual piles resulted in 12 large (0.60 m × 0.33 m) corrugations around the perimeter of the cell which represented approximately 17% of the cell area (Figure 3-5). The instrumentation of each cell was similar to that described by Annable et al. (1998), with four injection wells (IWs)
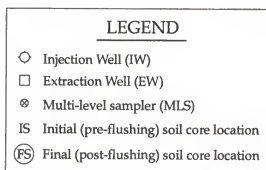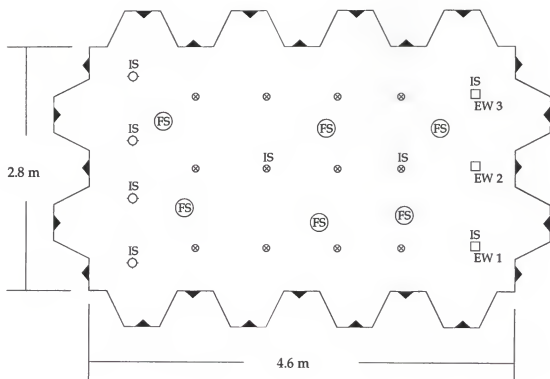
Figure 3-5. Plan view of cell layout. Solid triangles represent grout-filled joints between individual interlocking sheet piles. All preflushing soil cores were taken during installation of wells and MLSs at the indicated locations.

and three extraction wells (EWs), all fully-screened, and 15 multilevel samplers (MLSs) (Figure 3-6). Each of the seven wells was screened from 4.9 m to 7.9 m bgs with 0.25 mm slotted stainless steel casing. The MLSs were constructed using 0.32 cm stainless steel tubing terminating with either a 20 μm or 40 μm stainless steel filter. Between five and eight samplers were bundled at each of the 15 MLS locations, resulting in 96 individual sampling points. One set of MLSs was attached directly to each of the EWs prior to installation. Individual samplers may have become turned around during installation such that the sampler was located behind the EW (i.e., not in-line with the Iws). Thus, data from these samplers are generally considered to be less reliable than data from the other sampling locations.

A leak test was conducted in the cell prior to the flushing experiments. Heavy rains at the field site during late spring of 1996 contributed to a rise in the water table within the cell to a level of approximately 1.4 m bgs, greater than 5 m above the water table outside the cell. Water table monitoring over a period of 5 days showed losses of approximately 47 L/day at the extreme head differential, corresponding to an average leakage of 0.3% of the pore volume per day. Thus, it was deemed that during experiments conducted within the test cell, wherein the head differential across the cell walls was only approximately 2 m, losses from leakage could be ignored.

Hydrodynamics Characterization

A nonreactive tracer test was conducted to characterize the test cell hydrodynamics prior to partitioning tracer tests and SPME flushing. The effective pore volume of the test
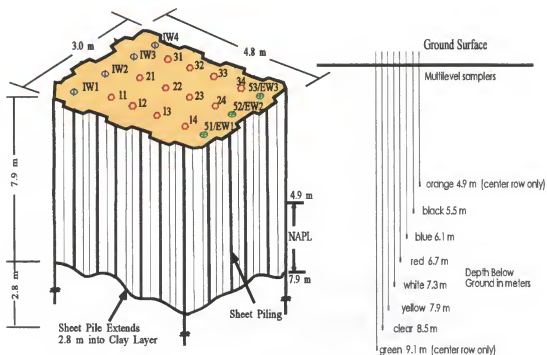
Figure 3-6. Schematic of the SPME test cell.

cell was determined to be approximately 6.0 kL, based on moment analysis of nonreactive tracer BTCs measured at the extraction wells. The effective porosity within the test cell was measured to be 0.14 by both hydraulic testing and the nonreactive tracer test. Also, the average hydraulic conductivity across the cell was determined to be 0.01 cm/s by measuring the hydraulic gradient between two piezometers, set 1.6 m apart along the flow direction, at different flow rates.

Contaminant Distribution Characterization

The spatial distribution of residual NAPL within the test cell both before and after SPME flushing was determined using two methods: (1) soil cores, and (2) interwell partitioning tracer tests.

Soil cores. The preflushing distribution of target NAPL constituents was determined from 85 soil samples collected from 8 borings, and the postflushing distribution was determined from 40 subsamples collected from 6 borings (Figure 3-5). Soil cores were subsampled immediately upon collection and approximately 10 g of soil were placed into 40 mL vials containing 5 mL each of methylene chloride and water. The samples were shipped in coolers overnight to Michigan Technological University, Houghton, MI and were analyzed using a Hewlett Packard 5890 GC equipped with a 0.25 mm diameter, 30 m long DB-1701 column (J&W Scientific) with either a Hewlett Packard 5970 or 5972 mass spectrometer.

For consistency in the evaluation of the remediation effectiveness of the 8 SERDP/AATDF pilot tests, soil samples collected from each test cell were analyzed for the

same 12 NAPL constituents (Montgomery Watson, 1995). Of these twelve constituents, the following seven were found to be most prevalent in the UF cell: two alkanes (n-decane and n-undecane), four substituted benzenes (1,2-dichlorobenzene, 1,3,5-trimethylbenzene, o-xylene, and p-xylene), and naphthalene. The following five constituents were found to have average soil concentrations of less than 0.1 mg/kg and were not considered further: 1,1,1-trichloroethane, trichloroethene, benzene, toluene, and ethylbenzene.

Selected preflushing soil concentration profiles are presented in Figure 3-7 for the three constituents with the highest soil concentrations: n-undecane, n-decane, and 1,3,5-trimethylbenzene (also see Table 3-4). The NAPL smear zone is evident where the maximum contaminant concentrations are centered around the approximate position of the regional water table (7 m bgs, or 1 m above the clay confining unit). Note that the center of mass was approximately 0.5 m deeper in the soil cores taken from the west side of the cell (IW 4 and EW 3) than in those from the east side of the cell (IW 1 and EW 1). Pre- and postflushing soil core data were compared below as a measure of the remediation effectiveness of the SPME flood.

Partitioning tracers. The amount and spatial distribution of residual NAPL present before and after SPME flushing were estimated using interwell partitioning tracer tests conducted with methods similar to those described by Annable et al. (1998). For both the pre- and postflushing tracer tests, steady-state water flow of approximately 1 PV/day (3.6 L/min) was established in the cell using peristaltic pumps (Masterflex L/S drives, Cole Parmer) to deliver uniform flow distributed equally between the injection and extraction wells. While maintaining steady water flow, a tracer pulse of 0.16 PV was delivered to the
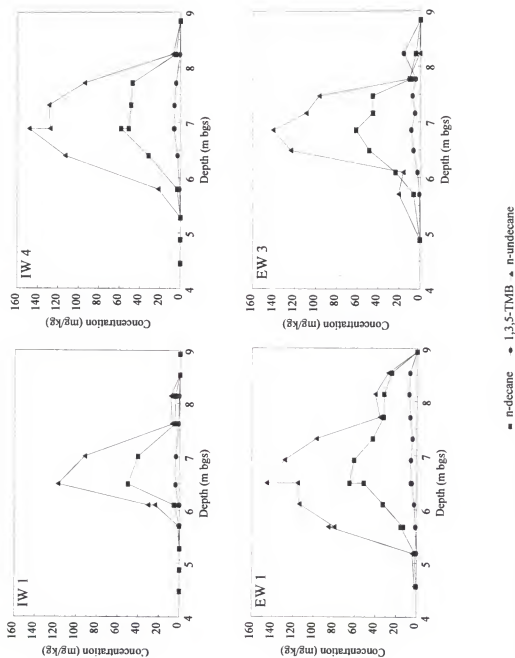
Figure 3-7. Selected preflushing soil core profiles for *n*-undecane, *n*-decane, and 1,3,5-trimethylbenzene (note that the clay depth was 8 m bgs).

■ n-decane   ● 1,3,5-TMB   ▲ n-undecane

IWs, with methanol (C_o = 2700 mg/L) and 2,2-dimethyl-3-pentanol (2,2-DMP; C_o = 930 mg/L) as the nonpartitioning and partitioning tracers, respectively. Samples collected at the EWs and MLSs during the partitioning tracer tests were shipped overnight to laboratories at UF, where they were analyzed using a Perkin-Elmer AutoSystems XL GC with direct liquid injection of 1μL onto a 0.53 mm diameter, 30 m long DB624 capillary column (J&W Scientific) with flame ionization detection (FID). The same system was also used to quantify NAPL constituents and *n*-pentanol during SPME flushing.

In order to accurately characterize the BTC tails, where much of the measured retardation is often found, both the pre- and postflushing tracer tests were continued until tracer concentrations at the EWs were below the detection limits (approximately 1 mg/L), and tracer BTC tails were exponentially extrapolated (Jin, 1995). The preflushing partitioning tracer test BTCs for methanol and 2,2-DMP measured at the three EWs are presented in Figure 3-8. For illustrative purposes, the distal portions of the EW 2 BTCs are replotted on a log scale on the secondary *y*-axis. The delayed arrival of 2,2-DMP in all three BTCs indicates the presence of NAPL within the swept volume of each EW.

The pulse-corrected mean arrival times (e.g., first normalized temporal moments) of the tracer BTCs were calculated, through numerical integration, in terms of cumulative flow. The nonpartitioning tracer first moments were therefore representative of the well swept volumes. The NAPL content within each swept volume was calculated from the tracer first moments using (2). The NAPL-water partitioning coefficient, K_N = 10.7, for 2,2-DMP was measured using batch equilibration methods.

□ Methanol ▲ 2,2-DMP
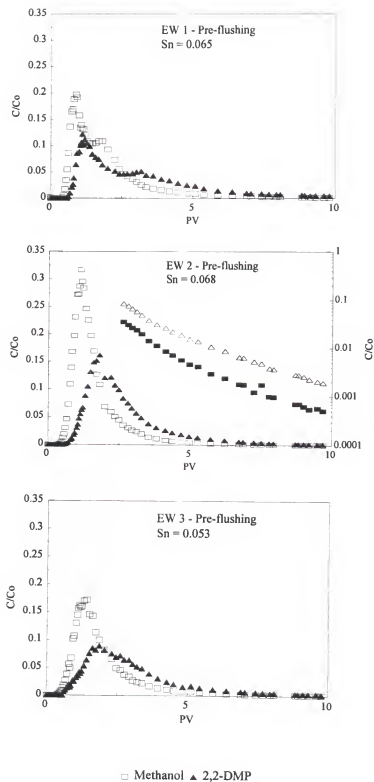
Figure 3-8. Preflushing partitioning tracer BTCs measured at each extraction well. The distal portion of the EW 2 BTCs have been replotted on log scale on the secondary *y*-axis.

The preflushing swept volumes for each well and the estimated NAPL content within those swept volumes are presented in Table 3-2. Note that the swept volumes of EW 1 and EW 3 were approximately equal, and both were larger than the EW 2 swept volume, while the EW 1 swept volume contained the most NAPL. Also, the EW 2 BTC showed higher peak concentrations and less spreading than those measured at EWs 1 and 3. These effects are indicative of the geometry of the test cell, wherein the EW 1 and EW 3 swept zones encompassed a broader distribution of flow path lengths, because of the sheet-pile wall corrugations, than did the center-line swept zone of EW 2.

Microemulsion Flushing

Field Methods

The microemulsion flushing field experiment consisted of pumping 9 PV of precursor solution through the test cell over a period of 18 days, followed by 1 PV of a surfactant-only flood, and 6.5 PV of water flooding. The designed duration of the experiment was based upon laboratory column studies conducted by Rhue et al. (1999) with contaminated soil from Hill AFB, wherein after approximately 5 PV of SPME flushing, NAPL constituents were no longer being eluted from the soil. This value was increased approximately two-fold to account for greater hydrodynamic dispersion expected as a consequence of field-scale heterogeneities.

Approximately 54.3 kL of microemulsion precursor solution were mixed on-site and delivered to the test cell using the fluid mixing and delivery system shown in the schematic diagram of Figure 3-9. Injection and waste tanks were located remotely from the cell, within

Table 3-2. Preflushing NAPL content in the swept volume of each well, as determined from partitioning tracers.

	EW 1	EW 2	EW 3	total
Swept volume (kL)	2.21	1.62	2.21	6.04
NAPL saturation, S_N	0.065	0.068	0.053	0.061^b
[a] NAPL volume (kL)	0.153	0.118	0.125	0.396

[a] NAPL volumes determined from $V_s \times S_N / (1 - S_N)$, where V_s is the swept volume. [b] Volume-weighted average of the three extraction wells.
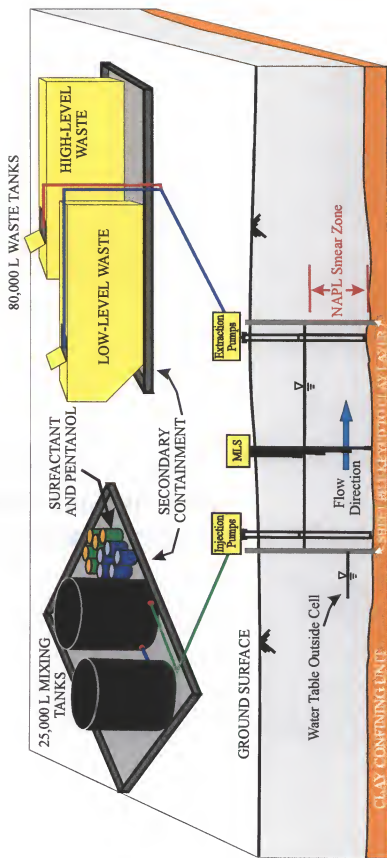
Figure 3-9. Schematic diagram of SPME flushing field experiment fluid mixing and delivery system.

secondary containment. The precursor solution was mixed in three batches in two 25 kL polyethylene tanks (Baker Tanks, Salt Lake City, UT). A 40 L/min sump pump was used for continuous circulation within the tanks during initial mixing and throughout the 18 days of microemulsion flooding. For each precursor batch, the water was added to the tank first, then Brij 97 (donated by ICI Americas, Inc., Wilmington, DE) was slowly (1 L/min) delivered using a peristaltic pump. After mixing overnight, *n*-pentanol (purchased from Union Carbide, Danbury, CT) was added in the same manner as the surfactant. The two 25 kL tanks were connected through valved ports at the tank bases. During the experiment, these ports were periodically opened for homogenization of the injection fluids as the fluid level decreased in the tank that was discharging to the test cell.

Fluid flow rates and flow perturbations. Because the viscosity of the precursor solution was measured to be approximately twice that of water, the initial fluid flow rate during SPME flushing was set at one-half the flow rate during the tracer tests (1.8 L/min, or 0.5 PV/day) in order to produce a hydraulic gradient equivalent to that measured during the tracer tests (see Equations 2-16 and 2-23). A slower flow rate also served as a precaution against potential mass transfer constraints on NAPL solubilization.

The importance of mass transfer rate limitations during the SPME flood was investigated by varying the SPME residence time. The original flow rate was doubled after approximately 2 PV (12.6 kL) of precursor solution had been flushed through the test cell, then reduced back to the original flow rate after 6.8 PV (40.8 kL), and finally doubled again after 8.2 PV (49.2 kL). In addition, the flow was interrupted for periods of 24 h at approximately 4 PV (22.8 kL), 32 h at 6 PV (35.7 kL), and 67 h at 9 PV (54.3 kL).

Sample analyses. Because the 12 analytes selected as indicators for comparison of the 8 SERDP/AATDF pilot tests were not the most prevalent constituents in the NAPL found in our cell, Rhue et al. (1999) selected 9 constituents which: (1) produced large peaks in a GC-FID chromatogram of NAPL from our cell which had been dissolved in hexane (Figure 3-2), and (2) were representative of different contaminant types. These nine constituents included the six compounds identified in Table 3-1, and 1,2,4-trichlorobenzene (TCB), 1,2-dichlorobenzene (DCB), and naphthalene. Fluid samples collected during the flushing experiment at the EWs (540 samples) and the MLSs (6500 samples) were shipped overnight to UF and were analyzed by GC-FID for these nine target NAPL constituents. The extraction well data for TCB, DCB, and naphthalene are not presented here because chromatographic peak overlapping led to unreliable results.

Waste management and minimization. The extraction fluid waste was characterized as either low-level or high-level. Fluids extracted from the test cell which were representative of groundwater contamination at the site, and fluids containing low levels of injected tracers, were characterized as low-level waste. Effluent which was extracted from the cell during the SPME flushing process was characterized as high-level waste. Both categories of waste were approved for discharge to the industrial wastewater treatment plant at Hill AFB. However, because of its high chemical oxygen demand, the high-level waste discharge was metered over a period of 30 days.

Extraction Well Results

SPME hydrodynamic considerations. Analytical interferences with NAPL constituents precluded analysis of effluent samples for surfactant concentrations. Therefore, precursor arrival at the EWs was inferred from n-pentanol arrival. This assumption was based on laboratory column studies (Rhue et al., 1999), using soil from the field site, that indicated no chromatographic separation of surfactant and pentanol. Also, the n-pentanol arrival time at the EWs during the SPME flood was equivalent to the arrival time of the nonpartitioning tracer (methanol) during the postflushing tracer test, indicating no significant retardation of the n-pentanol. Thus the precursor injection and elution profiles are characterized by measured n-pentanol concentrations (Figure 3-10).

A decreasing trend is evident in the n-pentanol injection profile (averaged over all four IWs) in Figure 3-10, indicating that the n-pentanol concentration varied among the three batches of precursor solution which were mixed during the 18 day experiment. This trend is evidenced in the subsequent n-pentanol BTCs measured at the EWs, where concentrations initially reached approximately 2.5%, but then decreased to approximately 2.25%, reflecting the changing injected concentrations. Of perhaps greater significance to the results presented here, though, is the disparity in the shapes of the BTCs between EW 2 and EWs 1 and 3. As noted with the tracer BTCs, the n-pentanol BTCs from EWs 1 and 3 were very similar, while that of EW 2 was steeper, indicating less tailing on the frontal rise. As discussed above, the corrugations of the sheet-pile walls contributed to a broader distribution of flow path lengths in the swept volumes of the two outer wells (EW 1 and EW 3) than in the swept volume of the center-line well (EW 2), leading to greater tailing in the BTCs at the outer wells.
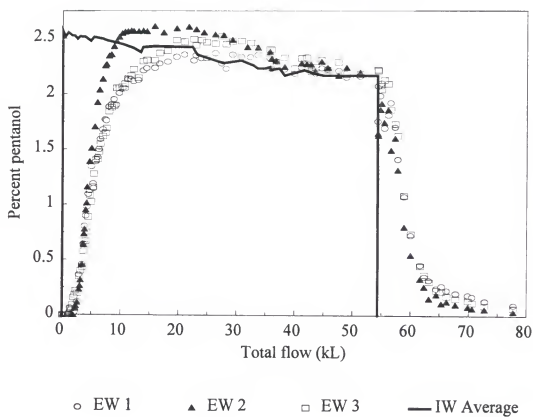
Figure 3-10. Precursor injection profile, averaged over all four injection wells, and elution profiles for the three extraction wells, all determined from *n*-pentanol analysis.

NAPL microemulsification. Breakthrough curves for target analytes measured at the EWs (Figure 3-11) represent NAPL constituent removal over the entire swept volume of the fully-screened wells. Note that the BTCs in Figure 3-11 are plotted in terms of the total flow through the entire test cell (total flow), while all other BTCs presented here are plotted as the flow through an individual well (local flow). For each target constituent, a significant increase was observed in the effluent fluid concentrations, compared to the pre-SPME flood concentrations. Overlain on the first of the target analyte BTCs (n-decane) is the n-pentanol breakthrough data for the three EWs. The increase in n-decane concentration is shown to be coincident with the arrival of the precursor solution; a similar trend was observed for all analytes. The NAPL constituent BTCs were integrated to determine the total mass of each contaminant removed from the swept volume of each of the EWs (Table 3-3). The amount of mass removed from each well was similar, with a trend of greater mass removed from EW 1 than from EWs 2 and 3, as was expected from the partitioning tracer results which indicated that the EW 1 swept volume contained the most NAPL.

For all analytes, the BTCs measured at EW 2 showed higher peak concentrations and less spreading than those measured at EWs 1 and 3. This behavior suggests differences in hydrodynamic dispersion among these flow zones, as discussed above in relation to the the n-pentanol and preflushing, nonpartitioning tracer BTCs.

During the SPME flood, the physical appearance of the fluids extracted from the test cell followed patterns similar to those evident in the BTCs of Figure 3-11. Both the resident groundwater and the precursor solution were clear and nearly colorless, but as the microemulsified NAPL started to break through at the extraction wells, a light brown color
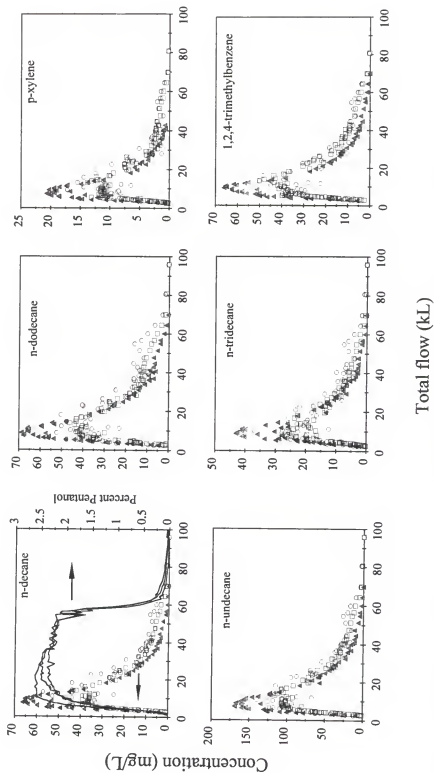
Figure 3-11. Targe NAPL constituent BTCs measured at EW 1 (circles), EW 2 (triangles), and EW 3 (squares). Overlain on the n-decane BTC are the n-pentanol breakthrough data.

Table 3-3. Mass of target NAPL constituents removed from the extraction wells during SPME flushing.

NAPL constituent	EW 1 (kg)	EW 2 (kg)	EW 3 (kg)	total (kg)
p-xylene	0.104	0.097	0.100	0.301
1,2,4-trimethylbenzene	0.370	0.366	0.387	1.123
n-decane	0.408	0.367	0.346	1.121
n-undecane	1.130	1.005	0.982	3.117
n-dodecane	0.492	0.442	0.414	1.348
n-tridecane	0.257	0.238	0.203	0.697

was evident in the effluent samples. This trend is evident in Figure 3-12, which is a photograph of effluent samples collected throughout the SPME flood. As the concentration of microemulsified NAPL increased, the extracted fluids became darker, reaching a dark brown color at maximum concentrations and gradually lightening in color as concentrations decreased. Even the darkest extracted fluids remained isotropically clear, with no sign of macroemulsification; in none of the fluids extracted from the test cell was a separate phase, or mobilized, NAPL observed.

For microemulsification, wherein droplets of NAPL are homogeneously dispersed within the aqueous phase, the relative mole fractions of the NAPL constituents in the microemulsion should be the same as those in the NAPL itself. Petroleum engineers have reported no fractionation (i.e., selective solubilization) in the microemulsification of oil mixtures and crude oils (Salager, 1979; Puerto and Reed, 1983), and have successfully modeled the microemulsification of these multicomponent oils as a single "psuedocomponent" (Vinatieri and Fleming, 1979). Recently, Shiau et al. (1996) reported no selective solubilization in the microemulsification of a ternary mixture of chlorinated solvents. Thus, in the SPME flood, simultaneous elution of all NAPL constituents was expected. Despite the broad range of hydrophobicities exhibited by the Hill AFB NAPL constituents (characterized by the log octanol-water partitioning coefficient, K_{ow}; see Table 3-1), they were all eluted from the test cell within a narrow time window. This behavior is demonstrated in the cumulative production curves for each analyte, which have been scaled to their respective calculated zeroth moments (Figure 3-13). While the constituents were all eluted nearly concurrently, a trend, that was consistent for each EW, was evident in the
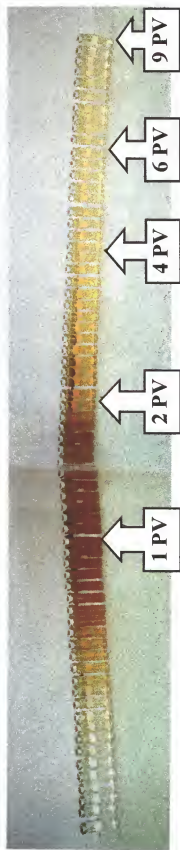
Figure 3-12. Effluent samples collected during SPME flushing, with selected sample times indicated in pore volumes (PV).
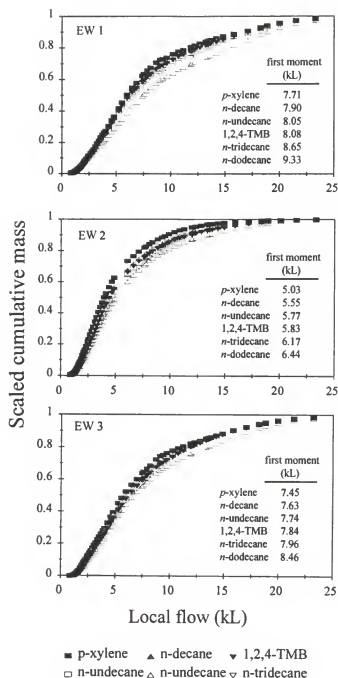
Figure 3-13. Cumulative production curves for the target NAPL constituents, each scaled to its respective calculated zeroth moment. First normalized moments are inset.

first normalized moments of the BTCs (inset in Figure 3-13). Generally the least hydrophobic constituents were eluted before the most hydrophobic (e.g., *p*-xylene was removed first and *n*-dodecane and *n*-tridecane were removed last), and this type of trend usually suggests selective dissolution. However, the trend in elution order did not strictly follow inverse-hydrophobicity order, as would be expected if selective dissolution was the governing process. This behavior was also investigated through an examination of the NAPL constituent BTCs measured at the MLSs (see below), with the results indicating that the trend in elution order may have been more closely related to the spatial distribution of the NAPL composition than to microemulsification dynamics.

Rate-limited microemulsification. Under rate-limited conditions, as the flushing fluid residence time is increased, through either reduced flow rates or flow interruption, solubilization is increased due to greater contact time between the NAPL and the solubilizing agent (Pennell et al., 1993). Of the many flow rate changes and interruption periods that were initiated during SPME flushing, noticeable changes in target NAPL constituent concentrations were observed only at one extraction well (EW 1) and only after the 67 h interrupt at 54.3 kL (Figure 3-11). This result suggests either equilibrium conditions or that rate-limited mass transfer processes were too slow to be evidenced during the time scale measured.

Elution of precursor solution. After 9 PV, the injection fluid was switched from the SPME precursor solution to a 3% solution of surfactant only. One PV of the surfactant solution was injected to facilitate the removal of *n*-pentanol from the test cell; this was followed by 6.5 PV of water flooding. After water flooding, the *n*-pentanol concentrations

at EW 2 had been reduced to 0.5% of C_o, while concentrations were 2% of C_o at EW 1 and 1% of C_o at EW 3. Following the postflushing partitioning tracer test, during which an additional 10 PV of water were flushed through the cell, *n*-pentanol concentrations in all three extraction wells were below 1 mg/L.

Multilevel Sampler Results

The relative sparseness of the MLS networks in the test cell necessarily resulted in incomplete sampling of the aquifer heterogeneity. However, examination of the MLS data allowed the characterization of the SPME flood on a smaller scale than was possible with the EW data. The MLS data were synthesized for interpretation in two ways: (1) data from all the MLSs within each of five control planes (CPs) normal to the mean flow direction were averaged to provide information about tracer travel times and NAPL dissolution as a function of distance along the mean flow direction, and (2) data from the MLSs located at the EWs were compared to the integrated EW data to provide information about tracer travel times and NAPL dissolution as a function of depth. Results from the former method were compared to similar values calculated from the 1995 UF/EPA cosolvent flushing experiment at Hill AFB (Rao et al., 1997; Sillan et al., 1998). The latter method could not be applied to the cosolvent flushing data because there were no MLSs installed at the EWs in the cosolvent test cell. The following MLS data (not shown) from both the SPME and cosolvent flushing studies were used for these analyses: pre- and postflushing nonpartitioning and partitioning tracer first moments, and the zeroth and first moments of NAPL constituent BTCs measured during flushing.

Control plane approach. The network of MLSs in the SPME test cell can be viewed as a series of control planes evenly spaced between the injection and extraction wells (Figure 3-5). If the nonpartitioning tracer local arrival times are assumed to be inversely proportional to the local fluxes, as suggested by Equations 2-30 and 2-31, then the flux-averaged tracer mean arrival time at a CP can be estimated from the harmonic mean, $\overline{t}_H$, of the tracer mean arrival times at the individual sampling points:

$$\overline{t}_H = \left(\frac{1}{n} \sum_{i=1}^{n} \frac{1}{t_i^*} \right)^{-1} \tag{3-1}$$

where n is the number of sampling locations within the control plane, and t_i^* represents the nonpartitioning tracer pulse-corrected, first normalized moment at sampling point i. In both the SPME and cosolvent test cells, the samplers located at or near the upper and lower flow boundaries (i.e., the water table and the clay layer formed the upper and lower boundaries, respectively) were generally less reliable than the samplers located within the main flow zone. The data from these sampling locations were relatively sparse and were therefore not included in the CP analysis. Thus, with 3 MLSs per CP and an average of 4 functioning sampling points per MLS, there were approximately 12 total sampling points per CP in each test cell.

For the SPME study, preflushing nonpartitioning tracer BTCs were measured at the 5.5 m, 6.1 m, 6.7 m, and 7.3 m bgs sampling locations at each CP. The harmonic means of the tracer arrival times at each CP are presented in Figure 3-14a along with a linear interpolation of tracer arrival time along the length of the test cell that was based on the flux-
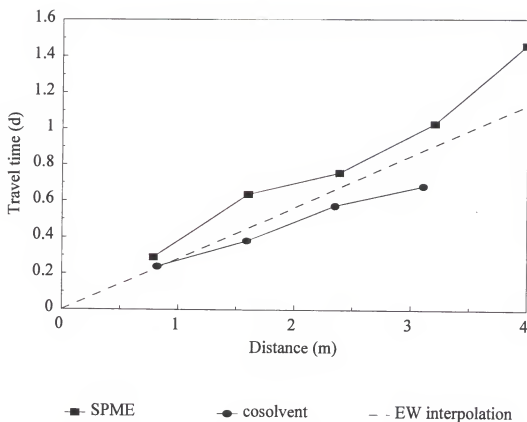
Fig. 3-14. Harmonic means of nonreactive tracer travel times at the MLSs in each control plane compared to a linear interpolation based on the mean arrival times of the tracer at the EWs in the SPME and cosolvent test cells.

averaged tracer mean arrival time measured at the EWs. A similar plot constructed using preflushing nonpartitioning tracer data from the cosolvent flushing experiment is presented in Figure 3-14b (calculated using nonpartitioning tracer mean arrival times at the 4.57 m, 4.95 m, 5.33 m, and 5.72 m bgs sampling locations). The flux-averaged tracer mean arrival time at the EWs was approximately 1.2 d in each cell, however, the swept volumes of the EWs, representative of the entire test cell, included volumes behind the EWs that were not within the swept volumes of the MLSs. Therefore, for this analysis the mean arrival times at the EWs were corrected to account for the extra volumes behind the EWs. Scale factors of 0.95 and 0.92 were derived from the geometries of the SPME and cosolvent cells, respectively, resulting in mean arrival times of 1.06 d and 1.09 d in the SPME and cosolvent cells, respectively.

In both test cells, the trend of increasing tracer mean arrival time with travel distance was consistent with the linear assumption based on the EW tracer mean arrival times. This indicates that the average flow velocity within both test cells was relatively homogeneous with distance, and that the MLS data compared favorably with the EW data. The largest deviation of the MLS data from the EW-based interpolation occured at CP_5 ($x = 4$ m) in the SPME cell. The MLSs at this CP were attached directly to the EWs prior to installation. Individual samplers may have become turned around during installation such that the sampler was located behind the EW (i.e., not in-line with the IWs), contributing to the relatively long average travel time at CP_5.

The BTCs measured at the MLSs during flushing were integrated to determine the mass of each NAPL constituent removed from within the swept volume of each sampling

location. However, while flux-averaged EW BTCs could be directly integrated to obtain the NAPL constituent masses, the local fluxes, q_i, at the individual multilevel sampling locations were unknown and had to be estimated. Local flux estimates were obtained based on the law of mass conservation, which requires the total fluid flux, Q, through each test cell to have been constant at all planes normal to the flow direction, and the assumption that all the samplers within each control plane represented equal areas. Also, the ratio of the harmonic mean tracer arrival time at a CP and the tracer arrival time at the individual sampling point was assumed to be inversely related to the ratio of the average flux at the multilevel sampling locations, Q/η, and the local flux, resulting in the following expression for the local fluid flux:

$$q_i = \frac{Q}{n} \frac{\bar{t}_H}{t_i^*} \qquad (3\text{-}2)$$

Local estimates of NAPL constituent mass removal were made by multiplying the local fluxes by the zeroth moments of the target NAPL constituent BTCs measured at the MLSs. However, in order to account for the the flow rate changes during the SPME study, the temporal moments at each sampling location were calculated in terms of scaled time. Because the local flux estimates were based on the tracer test flow rate (3.6 L/min), the ratio of the SPME flow rate and this flow rate was used as a scaling factor. For example, the duration of the period over which the SPME flood flow rate was 1.8 L/min was halved when calculating temporal moments in order to account for the 3.6 L/min basis of the local flux estimates.

The total mass removed between the injection wells and a given CP was then represented by the sum of the local removal estimates at each sampling point within the CP. For both the SPME and cosolvent studies, the total mass removed at each CP was scaled to the total mass removed through each test cell, as determined from EW BTCs (see Table 3-2 for the SPME study and Rao et al. (1997) for the cosolvent study), and compared to a linear interpolation along the length of each test cell based on the EW total (Figure 3-15). For this analysis, the EW-based mass removal totals were again scaled to account for the volume behind the wells, as described above. For the cosolvent study, data are presented for 1,2-dichlorobenzene (DCB) and n-undecane, the two most prevalent constituents. In the cosolvent cell the trend of increasing total mass removal with distance agreed well with the linear interpolation estimate based on the EW total, indicating that mass removal was relatively homogeneous along the flow path. Similar agreement was observed in the SPME cell, with the exception of CP_2 where the data indicated the implausible result of greater mass removal than at CP_3. While the partitioning tracer test results do indicate a proportionately large NAPL volume between CP_1 and CP_2 (see below), the excessive total removal predicted at CP_2 is likely due to an over-prediction of the local fluxes at this CP.

The general agreement between the CP data and the EW interpolations in Figures 3-14 and 3-15 indicates that the transport and dissolution processes were approximately linear in the SPME and cosolvent cells. However, these data also indicate that while improved descriptions likely would have been obtained with more sampling locations, the sampler network density at the Hill AFB test sites appears to have been sufficient to adequately
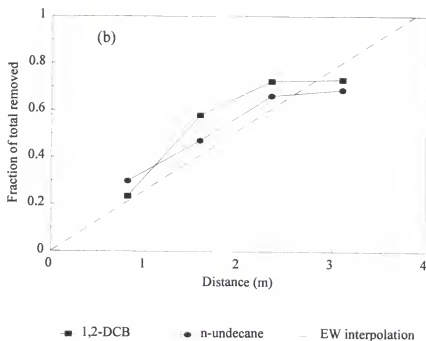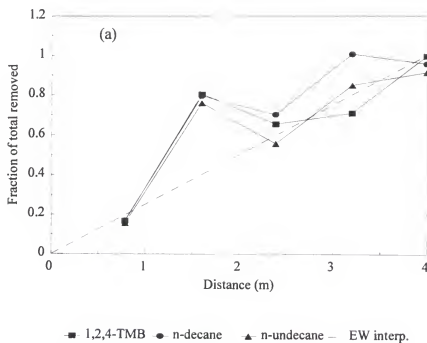
Figure 3-15. MLS-based estimates of total removal of select NAPL constituents at each control plane, scaled to the EW-based measure of total mass removed and compared to a linear interpolation of the EW value for the (a) SPME and (b) cosolvent studies.

describe tracer travel time and NAPL dissolution behavior as a function of distance in the direction of flow.

Extraction well MLSs. The swept volume of each EW encompassed the entire length of the cell, approximately one-third of the width, and the entire vertical depth, as the wells were fully screened from 4.9 to 7.9 m bgs. Thus, BTCs measured at each EW are representative of NAPL dissolution over approximately one-third of the cell volume. During the SPME study, samples were collected from five depths (5.5 m, 6.1 m, 6.7 m, 7.3, and 7.9 m bgs) at all three of the MLSs that were attached directly to the EWs. Therefore, BTCs measured at the MLSs attached to the EWs are representative of NAPL dissolution over a volume of approximately one-fifth of those measured at the EWs.

The local flux at each sampling location was estimated in a manner analogous to that described above. While the total flow rate through all planes normal to the mean flow direction was known to be equal, the local flow rate was known only at the well locations. Thus, because the CP_5 MLSs were attached to the EWs, the flow rate was known on a smaller scale than for the other CPs. Therefore, instead of using the total flow rate through the test cell (3.6 L/min) in (3-2) to estimate the local fluxes, the flow rate through each EW (1.2 L/min) was used as Q. Also, $\bar{t}_H$ was determined from the tracer arrival times at the 5 samplers at each EW instead of using the arrival times at all 15 samplers in the control plane.

The local flux estimates were used to integrate the constituent BTCs measured at each MLS located at the EWs. The constituent masses determined from this analysis were summed for all five depths at each MLS and compared to the total mass removed from the respective EW (Table 3-4). Again, the EW-based values were scaled to account for the

volume behind the wells, as described above. In addition, the mass removed of each constituent was summed from all of the samplers within the CP and compared to the sum of the EW mass removals. These values are compared in Table 3-4 to similar values computed using the CP approach described above. Both MLS data synthesis methods compared favorably with the EW data.

Analysis of the data from the MLSs located at the EWs also allows a comparison of the relative mass removal with depth for each NAPL constituent (Figure 3-16). The composite total of all 15 sampling locations at the EWs shows that the most mass was removed from the samplers located 6.7 m bgs, indicating that the NAPL saturation at this depth was higher than at the other depths, which is consistent with the preflushing soil core data (Figure 3-7). Also note that at EW 1 the MLS data indicates that the NAPL saturation was highest at 6.7 m bgs, but at EW 3 the NAPL saturation appears to have been highest at 7.3 m bgs, while at EW 2 the highest NAPL saturation appears to have been between these depths. These results are also consistent with the soil core data (Figure 3-7) which showed that the center of mass for the target analytes was slightly deeper on the east side of the cell (IW 1 and EW 1) than on the west side of the cell (IW 4 and EW 3).

Also evident from Figure 3-16 are spatial trends in the elution of the NAPL constituents. At all depths, n-undecane, n-dodecane, and n-tridecane were removed in nearly constant proportions. Conversely, at all three EWs, p-xylene, n-decane, and 1,2,4-TMB were removed in proportionately greater amounts from the swept volume represented by the 7.3 m bgs sampler than were the other three constituents of interest. Finally, at EW 2 a disproportionately large mass of 1,2,4-TMB was removed from the 7.9 m bgs sampler.

Table 3-4. Mass of each NAPL constituent eluted from the MLSs at the EWs; scaled to the mass removed through the EWs.

NAPL Constituent	EW 1	EW 2	EW 3	Total	Total - CP
p-xylene	1.02	0.83	0.74	0.87	0.84
1,2,4-TMB	1.28	1.58	0.68	1.17	1.00
n-decane	1.09	0.91	0.82	0.95	0.96
n-undecane	1.01	0.83	0.79	0.88	0.91
n-dodecane	1.39	1.12	1.11	1.22	1.29
n-tridecane	1.32	0.93	1.03	1.10	1.15

Note that the mass removed from the EWs was determined by adjusting the values in Table 3-2 to account for the volume behind the EWs (scale factor of 0.92).
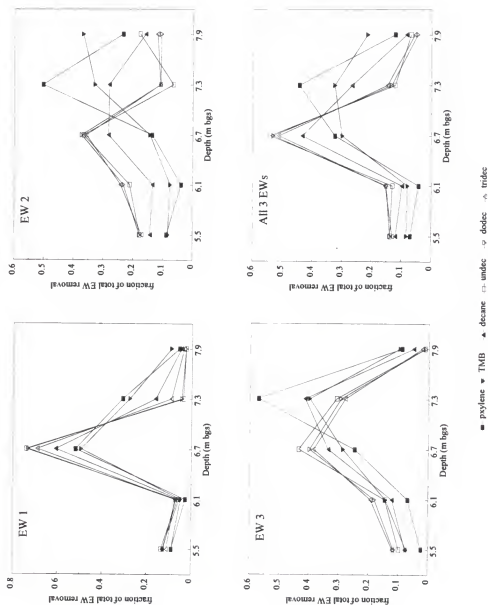
Figure 3-16. Estimates, by depth, of the fraction of total mass of select NAPL constituents removed from the specified EW, as determined from the MLSs located at the EWs.

Inspection of the local flux estimates for the MLSs at the EWs (Table C-2) reveals that the zone represented by the 7.3 m bgs samplers was estimated to have the highest local fluid flux (0.34 L/min, determined from an arithmetic average of the fluxes at the samplers at the three EWs), while the zone represented by the 7.9 m bgs was estimated to have the lowest local flux (0.15 L/min). Thus, the early elution of *p*-xylene and *n*-undecane, and the relatively late arrival of 1,2,4-TMB, that were observed at the EWs (Figure 3-11) may have been a result of the spatial distribution of the NAPL composition within the test cell, rather than of selective dissolution by the microemulsion precursor solution.

Rate-limited microemulsification. While the NAPL constituent BTCs measured at the EWs showed little response to the flow rate perturbations that were designed to reveal evidence of rate-limited microemulsification, BTCs measured at many of the MLS locations did show elevated concentrations following periods of quiescence. Complete BTCs were measured at 65 of the 96 sampling ports, of which 4 exhibited too much scatter to make any determinations regarding rate limitations, and in an additional 20 of the BTCs virtually all of the constituent mass had been removed before the 32 h interrupt at 9.7 d. Of the remaining 41 BTCs for which judgements regarding rate-limitations could be made, 20 showed no effect following any of the flow interruption periods and 21 showed elevated concentrations following at least one interrupt. Examples of BTCs where most of the mass was removed prior to the interruption periods are presented in Figure 3-17 and BTCs showing no effects of rate-limitations are presented in Figure 3-18. The BTCs presented are for the three constituents that were removed from the EWs in the greatest quantities (*n*-undecane, *n*-dodecane, and 1,2,4-TMB; see Table 3-4). Note that the flow interruption
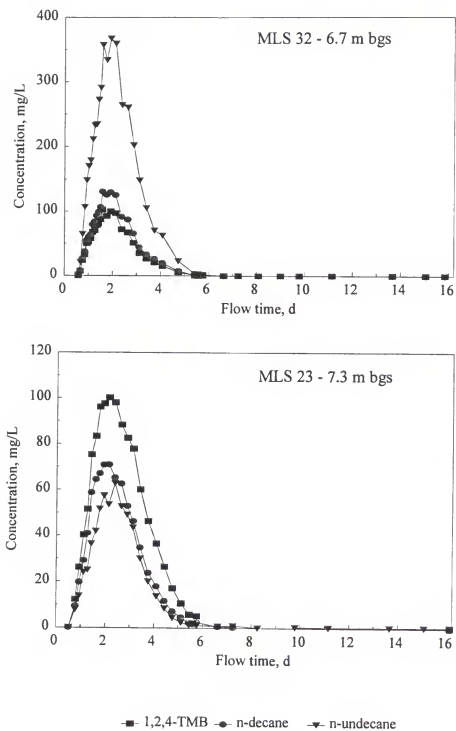
Figure 3-17. Examples of BTCs measured at MLS locations where most of the NAPL constituent mass had been removed prior to the flow interruption periods (initiated at $t = 7.0$ d, 9.7 d, and 15.0 d).
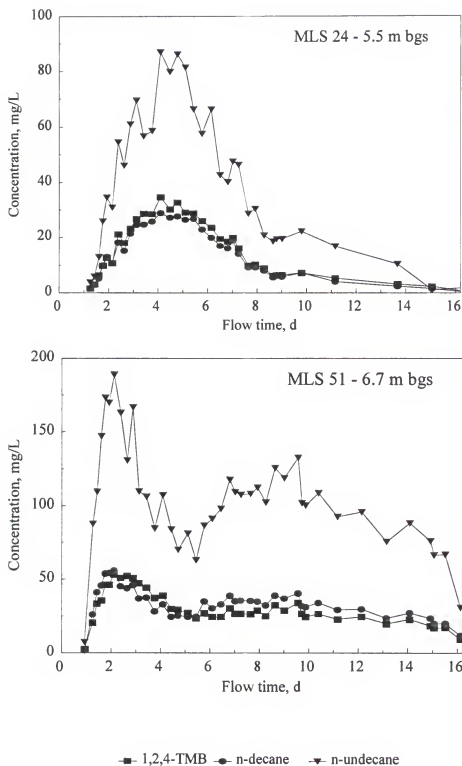
Figure 3-18. Examples of BTCs measured at MLS locations where no effects of rate-limitations were observed following flow interruption periods at t = 7.0 d, 9.7 d, and 15.0 d.

periods initiated at 4 PV, 6 PV, and 9 PV corresponded to times of 7.0 d, 9.7 d, and 15.0 d, respectively, and that at none of those times was an increase in concentration evident in the BTCs of Figure 3-18. However, at the samplers located 5.5 m bgs at MLSs 22 and 23, increased solubilization was evident following all three flow interruption periods (Figure 3-19). Examples of BTCs measured at locations where substantially increased solubilization was evident following only one of the flow interrupts are presented in Figure 3-20. The complete set of MLS BTCs can be found in Jawitz et al. (1997a).

Local flux estimates were also available at 36 of the 41 sampling locations where rate-limitations could be investigated. For the MLSs located at the EWs, local fluxes were calculated based on the flow rate through each well, whereas all other MLS fluxes were calculated using the control plane approach. These 36 locations are listed, in order of descending flux, in Table 3-5, and are categorized as to whether or not the constituent BTCs showed evidence of rate-limitations. The average rank order was 12.4 for the locations showing rate-limitations was 22.4 for the locations showing no evidence of rate-limitations. Thus, not only do the MLS data suggest evidence of mass-transfer limitations in the SPME flood, but a correlation between high local fluxes and mass-transfer limitations was found.

<u>NAPL Removal Effectiveness</u>

<u>Measures of Performance Effectiveness</u>

Rao et al. (1997) used extraction well mass balances, and pre- and postflushing data from groundwater samples, soil cores, and partitioning tracer tests to characterize the NAPL removal effectiveness, ϵ_N, of the UF/EPA cosolvent flushing experiment. The NAPL
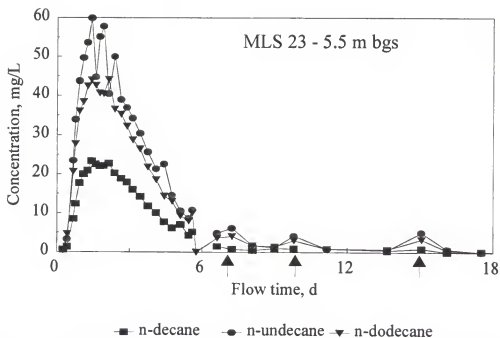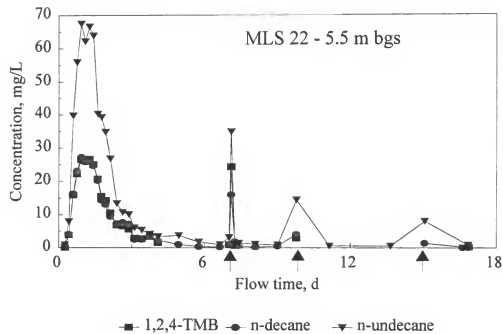
Figure 3-19. Breakthrough curves measured at MLS locations where increased solubilization was evident following all three flow interruption periods (t = 7.0 d, 9.7 d, and 15.0 d, indicated with arrows).

— n-decane   — n-undecane   — n-dodecane
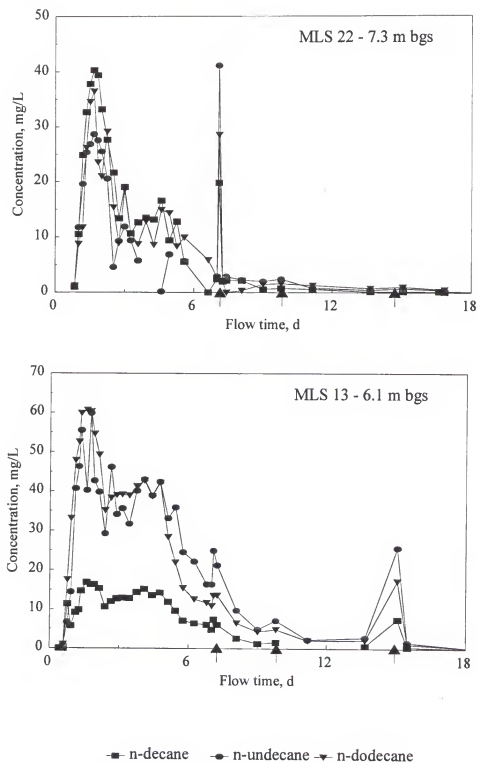
Figure 3-20. Examples of BTCs measured at MLS locations where substantially increased solubilization was evident following only one of the flow interrupts ($t = 7.0$ d, 9.7 d, and 15.0 d, indicated with arrows).

Table 3-5. Correlation between local flux and rate-limited microemulsification.

MLS	Depth bgs (m)	Local flux (L/min)	Rate-limited	No effect
22	5.5	0.587	1	
33	7.3	0.570	2	
13	6.1	0.516	3	
31	6.1	0.499	4	
34	6.1	0.473	5	
51	6.7	0.457		6
34	7.3	0.446	7	
14	6.1	0.392		8
31	6.7	0.377	9	
23	5.5	0.365	10	
24	6.1	0.349		11
24	6.7	0.339		12
34	5.5	0.299	13	
12	5.5	0.293	14	
22	7.3	0.280	15	
52	6.7	0.262		16
52	7.3	0.255		17
52	7.9	0.247		18
23	6.7	0.241		19
12	6.1	0.239	20	
51	7.3	0.234		21
11	5.5	0.212		22
33	5.5	0.211	23	
22	6.1	0.200		24
22	6.7	0.187		25
32	6.1	0.186		26
14	6.7	0.183		27
13	5.5	0.182		28
23	6.1	0.182		29
33	6.1	0.154	30	
14	5.5	0.109		31
51	7.9	0.106		32
53	7.9	0.103		33
11	6.1	0.083	34	
21	6.1	0.065		35
24	5.5	0.060		36
Average Rank			12.7	22.7

removal effectiveness of the SPME flood was determined from partitioning tracer tests and soil cores using the following relation:

$$\epsilon_N = \frac{\zeta_{preflushing} - \zeta_{postflushing}}{\zeta_{preflushing}} \qquad (3\text{-}3)$$

where ζ was replaced by S_N for the partitioning tracer tests and $\overline{X}_c$, the cell-average soil concentration of NAPL constituent c, for the soil core analyses. In addition, NAPL constituent BTCs were integrated to determine the total mass of each contaminant removed during SPME flushing. These values were compared to estimates of the initial amount of NAPL present as determined from both partitioning tracer tests and soil cores.

Groundwater samples were collected from 84 MLSs both before and after SPME flushing and were analyzed for all 12 analytes monitored in the soil samples, except for the very slightly soluble *n*-decane and *n*-undecane, using headspace GC techniques. However, all but seven of the groundwater samples resulted in non-detects, most likely because these constituents were present in our cell in only very small quantities (Table 3-2). Therefore, data from the groundwater samples were not used to evaluate the effectiveness of the SPME flood.

Soil Cores

Soil concentration profiles of several target NAPL constituents, measured both before and after SPME flushing, are presented in Figure 3-21. The NAPL smear zone is evident in the pre-flushing data, wherein the maximum contaminant concentrations are centered around the approximate position of the regional water table (7 m bgs, or 1 m above the clay

Concentration in soil (mg/kg)
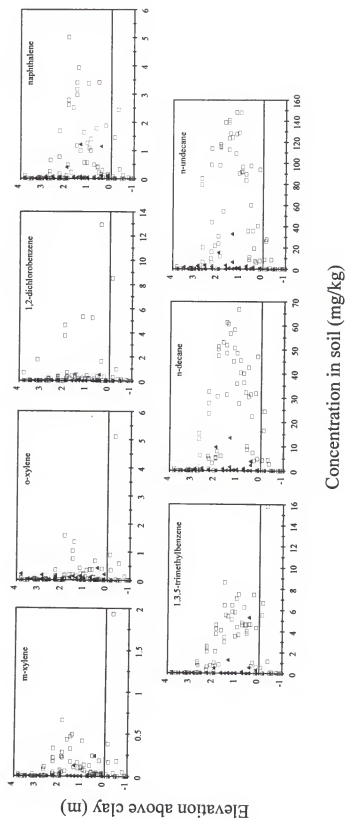
Figure 3-21. Soil concentration profiles before (squares) and after (triangles) SPME flushing for selected NAPL constituents (determined from methylene chloride extracts of soil samples).

confining unit). A visual comparison of the pre- and post-flushing data indicates a dramatic reduction in the target analyte concentrations.

Arithmetic average concentrations of the target constituents are presented in Table 3-6 for soil samples collected within the flushed zone both before and after SPME flushing. Data for those constituents with pre-flushing average concentrations of less than 0.1 mg/Kg are not presented here. Note that the concentrations were significantly higher for *n*-undecane, *n*-decane, and 1,3,5-trimethylbenzene (1,3,5-TMB) than for the other components. The results for these more prevalent constituents are considered to be more reliable than those of the other constituents present only in very small amounts.

Values for NAPL removal effectiveness were determined, using (3-3), from the fraction reduction in average soil concentration of the target NAPL constituents (Table 3-6). For the NAPL constituents with substantial initial amounts (i.e., pre-flushing average soil concentrations of > 1 mg/Kg), NAPL removal effectiveness values were greater than 90%.

Partitioning Tracer Tests

Partitioning tracer BTCs measured at both the EWs and MLSs were used to evaluate E_N for the SPME flood. A comparison of the MLS-measured E_N values with the EW values is complicated by the fact that each MLS value is representative of the zone swept by the tracers between the injection wells and the sampling point. Thus, obtaining truly local estimates has required either the differencing of measurements made at successive sampling points, under the assumption that the flow paths between sampling points were strictly linear (Helms, 1997; Sillan et al., 1998), or the use of stochastic inverse modeling techniques

Table 3-6. Pre- and postflushing average soil concentrations of target NAPL constituents.

NAPL constituent	Average soil concentration (mg/kg)[a]		Fraction Reduction[d]
	Preflushing[b]	Postflushing[c]	
n-undecane	61.2 ± 51.6	2.51 ± 5.87	0.96 ± 0.10
n-decane	24.9 ± 21.2	1.10 ± 2.71	0.96 ± 0.12
1,3,5-trimethylbenzene	2.90 ± 2.49	0.25 ± 0.89	0.92 ± 0.31
naphthalene	0.91 ± 1.23	0.11 ± 0.27	0.88 ± 0.34
1,2-dichlorobenzene	0.74 ± 1.99	0.03 ± 0.08	0.96 ± 0.16
o-xylene	0.18 ± 0.31	0.06 ± 0.09	0.65 ± 0.79
m-xylene	0.12 ± 0.15	0.02 ± 0.04	0.87 ± 0.39

[a] Values are arithmetic averages with standard deviation, where standard deviation represents the spatial variability. [b] Of the 83 samples, $n = 59$ were from within the swept zone. [c] $n = 36$. [d] Fraction reduction determined from $(C_i - C_f)/C_i$, where C_i is the pre-flushing average concentration and C_f is the post-flushing average concentration. Standard deviation of fraction reduction determined by propagating pre- and post-flushing standard deviations, STD_i and STD_f, respectively, using $[(C_f STD_i/C_i^2)^2 + (STD_f/C_i)^2]^{1/2}$.

(James et al. 1997). Here, the control plane approach was again implemented to synthesize the MLS data for comparison with the EW data. Results from the application of the control plane approach to the partitioning tracer data from the 1995 UF/EPA cosolvent flushing experiment at Hill AFB (Rao et al., 1997; Sillan et al., 1998) are presented here as well.

Extraction well data. A comparison of the postflushing tracer BTCs (Figure 3-22), with the preflushing data (Figure 3-8), reveals substantially less retardation of 2,2-DMP in the postflushing test for all three EWs. Note that the distal portions of the BTCs were again plotted on a log scale on the secondary y-axis. The postflushing swept volumes and the estimated NAPL content within them are presented in Table 3-7, along with the NAPL removal effectiveness, determined from the fraction reduction in S_N (Equation 3-3). The cell-average reduction in S_N was 72%.

Multilevel sampler data. Because the swept volume of each sampling point within a given CP was assumed to be equal, the arithmetic average of the pre- and postflushing S_N values measured at each sampling point within the CP, $\overline{S}_N$, was assumed to represent the average NAPL saturation within the zone between the IWs and the CP. The volume between each CP was equivalent to approximately 20% of the total volume of each test cell. Therefore, S_{N-CP_i}, the contribution of the volume between CP_{i-1} and CP_i to the cell-average NAPL saturation, was determined as follows for both the pre and pre- and postflushing conditions:

$$S_{N-CP_i} = \sum_{i=1}^{n}\left[(0.2\,i\overline{S}_{N_i}) - 0.2(i-1)\overline{S}_{N_{i-1}}\right] \qquad (3-4)$$

□ Methanol ▲ 2,2-DMP
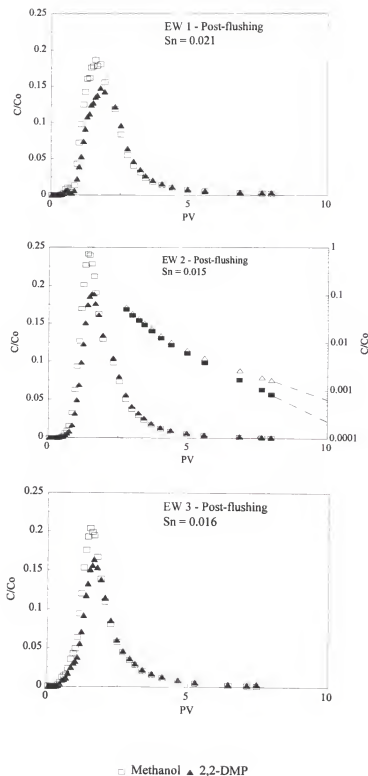
Figure 3-22. Postflushing partitioning tracer BTCs measured at each extraction well. The distal portion of the EW 2 BTCs have been replotted on log scale on the secondary *y*-axis; dashed lines are exponential extrapolations.

Table 3-7. Postflushing NAPL content in the swept volumes of each well, as determined from partitioning tracers.

	EW 1	EW 2	EW 3	total
Swept volume (kL)	2.17	1.88	2.04	6.09
NAPL saturation, S_N	0.021	0.015	0.016	0.017[b]
[a] NAPL volume (kL)	0.047	0.029	0.033	0.109
Fraction reduction of S_N	0.68	0.78	0.70	0.72

[a] NAPL volumes determined from $V_s \times S_N / (1 - S_N)$, where V_s is the swept volume. [b] Volume-weighted average of the three extraction wells.

where n is the number of CPs (four for the cosolvent cell and five for the SPME cell). The S_{N-CP_i} values were summed sequentially and are plotted with distance along the direction of flow for the two test cells in Figure 3-23. The MLS-based estimates of S_{N-CP_i} were compared to linear interpolations of the EW-based cell-average S_N estimates in each test cell. Also plotted in Figure 3-23 are the control plane E_N values determined using (3-3) with the pre- and postflushing S_{N-CP_i} values. These MLS-based values are compared to the EW-based cell average E_N estimates, which were assumed to be uniform over the length of each test cell.

The MLS-based estimates of both pre- and postflushing NAPL saturations at the CPs agree relatively closely with the interpolations made using the average values from the EWs for both the cosolvent and SPME flushing studies. The E_N values calculated from the MLS data also agree relatively closely with the assumption of uniform effectiveness, indicating that both flushing processes performed consistently along the direction of flow. The most notable exception is the SPME study S_{N-CP_S} value, which is much lower than the EW-based value at the same distance along the flow path and contributes to the low MLS-based E_N value at the same location.

<u>Extraction Well Mass Balance</u>

The NAPL removal effectiveness of the SPME flood was also estimated by dividing the amount of NAPL removed by the initial amount present. The volume of NAPL removed from the test cell was estimated by dividing the mass of each constituent removed through the extraction wells (Table 3-4) by the mass fractions of the constituents in the NAPL (Table 3-1) and the NAPL density (0.88 g/cm³). The initial amount of NAPL present as determined
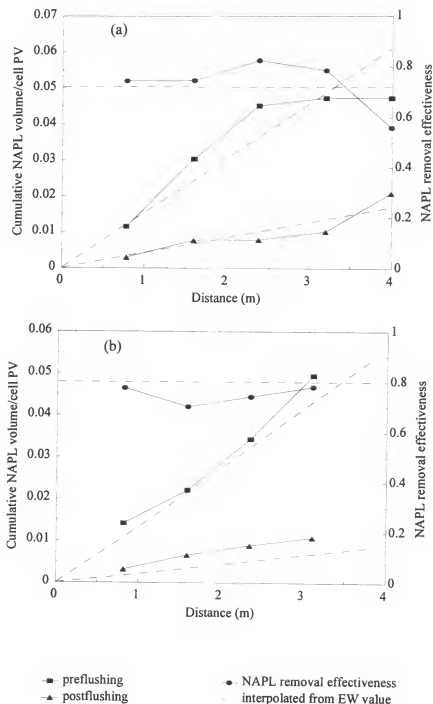
Figure 3-23. Comparison of EW- and MLS-based estimates of pre- and postflushing NAPL saturation and removal effectiveness at each control plane for the (a) SPME, and (b) cosolvent studies.

from partitioning tracers is shown in Table 3-2. Soil core data were also used to estimate the initial amount of NAPL present, but of the NAPL constituents that were common to the extraction well and soil core analyses, only n-decane and n-undecane yielded reliable chromatographic peaks in the effluent samples. The total mass of these two constituents initially present was calculated by multiplying the pre-flushing cell-average soil concentrations (Table 3-6) by the total mass of soil in the flushed zone, estimated from the cell area (14.9 m²), an average saturated depth of 3.0 m, and the soil bulk density. Because of the limited diameter (5 cm) of the hollow-stem auger used to collect the soil samples, and the standardized 40 mL vials used for the methylene chloride extractions, the soil concentrations reported in Table 3-6 are representative of primarily the sand fraction (i.e., smaller grain sizes) of the aquifer. The field aquifer material, however, contained a substantial fraction of gravel and cobbles. Therefore, the effective bulk density was estimated to be between 1.7 g/cm³, a standard value for sandy soils (Freeze and Cherry, 1979), and 0.66 g/cm³, equivalent to the standard value scaled by the ratio of the measured porosity (0.14) to the expected porosity for sandy soils (0.36).

The extraction well mass balance determined using partitioning tracers to estimate the initial NAPL volume yielded NAPL removal effectiveness values of 55-75% (Table 3-8). The mass balance obtained using soil core data to estimate the initial amounts of n-decane and n-undecane yielded NAPL removal effectiveness estimates of 60-175%. These results demonstrate that determinations of remediation effectiveness made using extraction well BTCs, where the mass removed and the initial mass are determined with different characterization techniques, may exhibit more inconsistency than methods where initial and

Table 3-8. NAPL removal effectiveness determined from extraction well BTCs and estimates of the initial amount of NAPL from both partitioning tracer and soils data.

NAPL constituent	source of initial mass estimate	
	partitioning tracers	soil cores [a]
p-xylene	0.60	
1,2,4-trimethylbenzene	0.74	
n-decane	0.68	0.61[b] - 1.54[c]
n-undecane	0.57	0.68[b] - 1.72[c]
n-dodecane	0.56	
n-tridecane	0.70	

[a] Of the constituents listed here, only *n*-decane and *n*-undecane were measured in the soil cores. [b] Obtained using an effective bulk density of 1.7 g/cm^3. [c] Effective bulk density of 0.66 g/cm^3.

final contaminant amounts are measured with the same technique, as with the partitioning tracer and soil core methods.

Relative Permeability

As described by (2-22), the relative permeability of a porous medium is a function of NAPL saturation. Thus, a measured difference between the pre- and postflushing average relative permeabilities of the aquifer material within the SPME flushed zone should reflect the difference in the pre- and postflushing average S_N. For the pre- and postflushing partitioning tracer tests, all parameters in (2-16) and (2-23) were constant except k_e and dh. The pre- and postflushing head differentials and NAPL saturations can then be related as follows:

$$\frac{dh_{pre}}{dh_{post}} = \left(\frac{1 - S_{N_{post}}}{1 - S_{N_{pre}}} \right)^{\zeta} \tag{3-5}$$

where the appropriate value of ζ for the Hill AFB field site was unknown. Corey (1986) reported that values of between 3 and 4 are typical for sandy porous media, but that a value of 3 corresponds to a uniform pore size with greater values as the degree of uniformity decreases. Therefore, because of the heterogeneous nature of the field site, the effective value of ζ was expected to be greater than 3.

The head differential across the SPME cell was determined from two piezometers set 1.6 m apart along the mean flow direction, and was monitored at regular intervals throughout the tracer tests. Values of dh measured during the last two PV of the preflushing partitioning tracer test and the first two PV of the postflushing partitioning tracer test (i.e., the data most

representative of the conditions immediately before and after SPME flushing) are presented in Figure 3-24 along with the mean values during each period. The pre- and postflushing tracer test flow rates measured at the EWs during these periods are also presented in Figure 3-24. The mean values of dh for the pre- and postflushing tracer tests were 0.15 m and 0.11 m, respectively, resulting in a value of 1.37 for the left side (3-5). Substitution of the pre- and postflushing S_N values from Tables 3-2 and 3-7 results in values of 1.17 and 1.20 for the right side of (3-5), using ζ values of 3.5 and 4, respectively. A ζ value of 6.9 was required to match the left and right sides of (3-5). Thus, it seems that the utility of relative permeability measurements for quantitative assessment of changes in S_N, is restricted by the uncertainty in ζ, resulting from the complexity of the field site aquifer materials, however, the head measurements required to evaluate changes in k_{rw} are simple, and these data do indicate a significant change in S_N between the pre- and postflushing tracer tests.

Discussion of NAPL Removal Effectiveness

The evaluation of the effectiveness of the SPME flushing experiment was confounded by the complex composition of the NAPL, leading to inconsistent results from the different removal effectiveness characterization methods.

Soil samples collected from the test cell during pre-flushing coring appeared to be completely coated with the NAPL. Soils collected during post-flushing coring did not appear to be coated with NAPL but appeared to be stained black, especially when compared to uncontaminated aquifer materials collected at the site. This result is consistent with laboratory evidence from column studies using contaminated soil from the field site and the
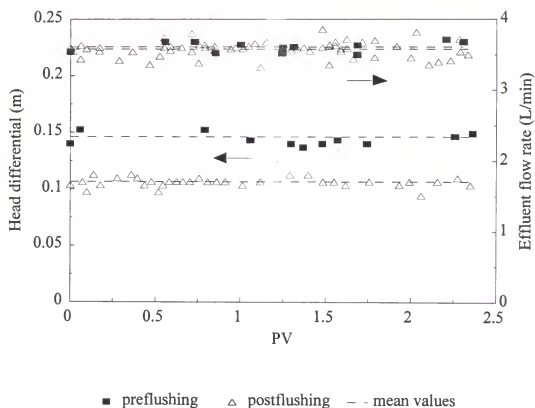
Figure 3-24. Head differential measured between two piezometers in the SPME cell during the pre- and postflushing tracer tests, along with the flow rates at the EWs during the same periods.

same SPME precursor (Rhue et al., 1999). After 5 PV of SPME flushing, the column was flushed with hexane, and no NAPL constituents were found in the hexane effluent, indicating that all compounds soluble in organic solvents had been removed from the soil. However, pre- and post-flushing partitioning tracer tests indicated that only 70% of the NAPL had been removed. Inspection of the flushed soil revealed a dark coating. This residue was not solubilized by either the SPME precursor or hexane, but did serve as a sorbent for the partitioning tracers (no retardation of tracers was found on uncontaminated field soil).

Thus, while soil core data indicate that > 90% of the mass of the target NAPL constituents was removed by the SPME flood, partitioning tracer and observational data indicate that an anthropogenic residue was left behind. It remains to be determined whether better agreement would be found between different techniques for assessing the effectiveness of SPME flushing at sites with less complex NAPLs.

NAPL Removal Efficiency

The efficiency of a system is defined as the work done divided by the energy supplied. For NAPL source zone remediation technologies, a measure of the work done is the volume of NAPL removed, ΔV_N. One measure of the energy input is the cost of the remedial system; however, technical performance is of more immediate interest here, and energy input was thus measured in terms of the volume of flushing fluid applied, quantified by the first normalized moments of the NAPL constituent BTCs, m_1^c. This approach enables the calculation of separate remediation efficiencies for NAPL constituents that may be eluted from the flushed zone at different times (i.e., after the application of different volumes of

flushing fluids). The first moment of each constituent was corrected for the resident fluid volume that was initially displaced by the flushing fluid by subtracting the first normalized moment of a nonpartitioning tracer measured at the same sampling location. Thus, the NAPL removal efficiency, E, is generally defined as the volume of NAPL removed by a given volume of flushing fluids (corrected for the resident volume of water):

$$E = \frac{\Delta V_N}{m_1{}^c - m_1{}^{np}} \qquad (3\text{-}6)$$

High values of E indicate efficient remediation technologies, with a maximum value of one (where all the NAPL present is removed with only one PV of flushing fluids). Likewise, E values would approach zero for the most inefficient remediation strategies.

A technology's efficiency rating should not be biased by the initial conditions under which it was tested. This measurement normalizes the performance evaluation of different experiments or pilot-scale tests to variations in the amount of NAPL initially present, and to variability in arrival time distributions (and, hence, permeability distributions). Assuming that a given technology would require proportionally more pore volumes of flushing fluid to remediate a site with a large initial NAPL saturation than a site with a low saturation, the same efficiency rating would result for both. However, if the efficiency rating of (3-6) were calculated using the fraction reduction in V_N instead of the change in V_N, the rating could be biased by the initial amount of NAPL present at a site.

Holding all other initial conditions equal, spatial variability in permeability may affect the second moment of a contaminant BTC, but should not affect the first moment.

Thus, by incorporating the first moment of the contaminant BTC as a measure of the volume of flushing fluid required to remove the contaminant, the end-point efficiency is normalized for contrasts in permeability variability between experiment sites.

It should be noted, however, that (3-6) does not account for variability in NAPL spatial distribution. The remediation of a site with a highly variable NAPL distribution would be expected to be less efficient than the remediation of a site with a more uniform NAPL distribution. Similarly, changes in the NAPL distribution during the remedial process may affect the remediation efficiency; however, these effects are not addressed here.

Specific Measures of Efficiency

The soil core, partitioning tracer, and extraction well mass balance characterization methods presented above can be used to quantify the work done by a remediation system with measures which can be transformed to the change in NAPL volume. Approaches for calculating NAPL removal efficiency using each of these three methods are described below.

Partitioning tracers. The first measure of NAPL removal efficiency is calculated using the change in NAPL saturation determined from pre- and postflushing partitioning tracer tests. Conversion of the NAPL saturation, defined as the volume of NAPL divided by the pore volume, to the NAPL volume requires multiplication by the pore volume:

$$\Delta V_N = \frac{\Delta S_N \, m_1^{np}}{1 - S_{N_{pre}}} \tag{3-7}$$

where it is assumed that the preflushing nonpartitioning tracer first moment, corrected for

the preflushing NAPL saturation, $S_{N_{pre}}$, is representative of the pore volume. Combination

of (3-6) and (3-7) results in the following expression for NAPL removal efficiency:

$$E_{pt} = \frac{\Delta S_N}{\left(\dfrac{m_1^c}{m_1^{np}} - 1 \right) \left(1 - S_{N_{pre}} \right)} \tag{3-8}$$

where the subscript pt indicates that this measure was determined using partitioning tracers.

<u>Soil cores</u>. The change in the mean soil concentration of a NAPL constituent, $\Delta \bar{X}_c$,

can be converted to an estimate of the change in NAPL saturation using the constituent mass

fraction within the NAPL, χ_c:

$$\Delta S_N = \frac{\Delta \bar{X}_c \, \rho_B}{\chi_c \, \rho_N \, \eta} \tag{3-9}$$

where ρ_B is the soil bulk density and ρ_N is the NAPL density. By combining (3-8) and (3-9),

the NAPL removal efficiency can be expressed as follows:

$$E_{sc} = \frac{\left(\dfrac{\Delta \bar{X}_c \, \rho_B}{\chi_c \, \rho_N \, \eta} \right)}{\left(\dfrac{m_1^c}{m_1^{np}} - 1 \right) \left(1 - \dfrac{\bar{X}_{c_{pre}} \, \rho_B}{\chi_c \, \rho_N \, \eta} \right)} \tag{3-10}$$

where the subscript sc indicates that this measure was determined from soil core data. This

formulation enables the comparison of efficiencies between systems wherein the amount of

an individual NAPL constituent initially present varies (e.g., the NAPLs initially present at

153

two sites may have different compositions but share common constituents). Again, if E_{ac} were calculated using the fraction reduction in $\overline{X}_c$, the measure could be biased by the initial mass of that contaminant.

NAPL constituent BTCs. The zeroth moment of an individual NAPL constituent BTC, m_0^c, is representative of the mass that was removed from the swept volume of the sampling location, and can be converted to the change in NAPL volume as follows:

$$\Delta V_N = \frac{m_0^c}{\rho_N \chi_c} \qquad (3-11)$$

Combination of (3-7) and (3-11) results in a third measure of NAPL removal efficiency:

$$E_{BTC} = \frac{m_0^c}{\rho_N \chi_c \left(m_1^c - m_1^{np}\right)} \qquad (3-12)$$

where the subscript BTC indicates that this measure was determined from a NAPL constituent BTC.

Pump-and-treat. For comparison purposes, the removal efficiency that would be expected from pump-and-treat (PAT) methods was estimated as well. If it is assumed that the concentration of a constituent in each pore volume flushed is equal to the product of the constituent aqueous solubility limit, S_c, and the constituent mass fraction in the NAPL, then the total constituent mass removed by PAT, represented by the zeroth moment of the constituent elution curve, can be expressed as follows:

$$m_0^c = S_c X_c V_T \qquad (3-13)$$

where V_T is the total volume of water flushed through the contaminant source zone. The remediation efficiency of a PAT operation, E_{PAT}, can be determined through combination of (3-10) and (3-13), subject to the following considerations: m_1^c is assumed to be equivalent to one-half of the number of PVs required to remove the constituent, and, because water is the flushing agent in PAT operations, m_1^c does not need to be corrected for the resident fluid pore volume. The resulting efficiency expression is then

$$E_{PAT} = \frac{2 S_c}{\rho_N} \tag{3-14}$$

Results

NAPL removal efficiencies were calculated for both the SPME and the cosolvent flushing studies using the partitioning tracer, soil core, and constituent BTC measures described above. The efficiency measure based on NAPL constituent BTCs was calculated at both the EWs and MLSs for both studies. Because the NAPL composition was not the same in the two test cells, different target constituents were analyzed for each experiment. This analysis will focus on the following constituents: n-decane and n-undecane, which were common to both test cells, 1,2,4-TMB (SPME study) and 1,3,5-TMB (cosolvent study), which were assumed to exhibit similar dissolution behavior because of their similar log octanol-water partitioning coefficients, 3.63 and 3.42, respectively (Sangster, 1989), and 1,2-dichlorobenzene (DCB) which was prevalent only in the cosolvent cell. For comparison with PAT, the behavior of more-hydrophobic contaminants was illustrated with n-decane ($S_c =$ 0.009 mg/L), and less-hydrophobic contaminants with DCB ($S_c =$ 100 mg/L). All of the

parameters required to calculate the NAPL removal efficiencies for both studies have been compiled in Appendix C.

  <u>Cell-averaged efficiencies</u>. When EW data are used in (3-8), (3-10), and (3-12), the NAPL removal efficiencies calculated using these measures are representative of the remediation performance averaged over the entire flushed zone. The cell-averaged efficiencies calculated using flux-averaged data from all three EWs for both the SPME and cosolvent studies are presented in Table 3-9. The mean of the efficiency values determined from all three measures was 0.02 for both the SPME and cosolvent studies, indicating that both technologies performed equally efficiently. A general interpretation of an efficiency of 0.02, based on (3-8), is that approximately 2.5 PV of flushing agents were required to effect a reduction of 0.05 in the average NAPL saturation within each test cell. However, it is emphasized that the efficiency calculations presented here were based on constituent BTC first moments, and thus represent the mean dissolution behavior. Because the NAPL constituent dissolution profiles exhibited significant tailing, from the combined effects of field-scale heterogeneities and rate-limited dissolution, more than 2.5 PV of flushing was required to approach complete NAPL removal (approximately 9 PV of flushing agents were flushed through each test cell).

  While there is no clear trend in the efficiency values in Table 3-9 to indicate whether cosolvent or SPME flushing was more efficient, a comparison of these values with the E_{PAT} values indicates that both flushing experiments removed the NAPL much more efficiently than pump-and-treat methods would have. Both flushing technologies were approximately 10^2 times more efficient than PAT for the less hydrophobic NAPL constituents (e.g., DCB)

Table 3-9. Cell-averaged NAPL remediation efficiencies for the SPME and cosolvent flushing field experiments.

Efficiency Measure	NAPL Constituent			
	DCB[a]	TMB[b]	n-decane	n-undecane
E_{pt} (Partitioning tracers)				
SPME	NP	0.018	0.019	0.018
Cosolvent	0.022	0.017	0.015	0.013
E_{sc} (Soil cores)				
SPME	NP	_[d]	0.030	0.021
Cosolvent[c]	0.026	NM	0.028	NM
E_{BTC} (Extraction wells)				
SPME	NP	0.019	0.018	0.015
Cosolvent	0.023	0.037	0.026	0.014
E_{PAT} (Pump-and-treat) [c]	2.4×10^{-4}	-	2.1×10^{-8}	-

[a] 1,2-dichlorobenzene was not present (NP) in the NAPL from the SPME cell. [b] Cosolvent experiment: 1,3,5-TMB; SPME experiment: 1,2,4-TMB. [c] These constituents were not measured (NM) in the soil cores from the cosolvent cell. [d] SPME: 1,2,4-TMB measured in effluent, but 1,3,5-TMB measured in soil cores. [e] Pump-and-treat efficiency was calculated only for 1,2-dichlorobenzene and n-decane.

and approximately 10^6 times more efficient for the more hydrophobic compounds (e.g., *n*-decane). Thus, by chemically enhancing PAT with either cosolvent or SPME technology, an improvement in NAPL removal efficiency of between 10^2 and 10^6 times may be expected, depending on the hydrophobicity of the compounds of interest.

Also, note that the average of the efficiencies determined from partitioning tracer tests, which required no transformations to calculate S_N, was very similar for both experiments, however, the cosolvent flushing removal efficiency decreased with increasing constituent hydrophobicity, while the SPME efficiency was approximately equal for all constituents. The differences in cosolvent flushing remediation efficiency for various NAPL constituents was due in part to the solvent injection program, wherein one PV of ethanol was injected before the introduction of the stronger solvent, *n*-pentanol, and in part due to selective dissolution (for details regarding the solvent injection program, see Rao et al., 1997). Less-hydrophobic compounds, such as DCB, were solubilized in the ethanol-water mixture, whereas more-hydrophobic compounds (such as *n*-decane) did not achieve significant solubility enhancement until the injection of *n*-pentanol was initiated.

An alternate method of determining remediation efficiency for the cosolvent flushing experiment, which would have strictly accounted for the delayed injection of *n*-pentanol, would have been to calculate E in terms of PVs of ethanol/*n*-pentanol/water solution flushed, instead of PVs of solvent solution flushed. However, because some initial amount ethanol-water flooding may be needed to prevent the phase separation of *n*-pentanol, the efficiency measures presented in Table 3-9 were calculated in terms of volume of flushing agents applied.

<u>Local efficiencies: MLS data</u>. There were a total of 38 sampling locations in the cosolvent cell and 61 in the SPME cell for which all of the information required for the calculation of NAPL removal efficiencies using (3-12) was available. The mean and standard deviations of the MLS-based efficiency values calculated at each control plane for both studies are presented in Table 3-10. It was assumed that each sampling location represented an equal area within the control plane and the efficiencies were thus arithmetically averaged. The average efficiencies at the control planes were relatively constant, indicating that the NAPL removal efficiency was not a function of distance along the flow direction. Also, the average efficiencies determined from all of the MLSs in each cell were in relatively close agreement with the average efficiencies determined from the EWs.

However, there was significant variability in the individual sampling location efficiency values, as evidenced by the large standard deviations associated with the CP averages in Table 3-10. Potential causes of variability in local NAPL removal efficiencies are differences in spatial distributions of the NAPL and differences in local flux. The latter was investigated by calculating the correlation between local NAPL removal efficiency and local flux using (2-43). The individual E values calculated at each sampling location are plotted as a function of the inverse of the local flux estimates in Figure 3-25, with the calculated correlation coefficients inset. For all constituents from both studies, a positive correlation was found between the inverse flux and E, indicating that higher efficiencies were realized at locations where the local fluxes were lower, as would be expected for rate-limited dissolution.

Table 3-10. Control plane and cell-wide averages of NAPL removal efficiencies determined using (3-12) from NAPL constituent BTCs measured at the MLSs for the cosolvent and SPME flushing studies. Arithmetic averages are shown with standard deviation.

	Cosolvent		SPME		
	DCB	undecane	1,2,4-TMB	n-decane	n-undecane
CP 1	0.013 ± 0.009	0.009 ± 0.004	0.033 ± 0.030	0.024 ± 0.026	0.021 ± 0.020
CP 2	0.020 ± 0.018	0.010 ± 0.006	0.029 ± 0.014	0.026 ± 0.019	0.020 ± 0.018
CP 3	0.021 ± 0.017	0.011 ± 0.005	0.027 ± 0.016	0.027 ± 0.022	0.017 ± 0.017
CP 4	0.021 ± 0.020	0.011 ± 0.006	0.026 ± 0.019	0.028 ± 0.023	0.019 ± 0.020
CP 5	–	–	0.024 ± 0.011	0.017 ± 0.008	0.012 ± 0.007
MLS Average [a]	0.018 ± 0.017	0.010 ± 0.006	0.028 ± 0.019	0.024 ± 0.020	0.017 ± 0.017
EW Average [b]	0.023 ± 0.004	0.014 ± 0.002	0.019 ± 0.003	0.018 ± 0.003	0.015 ± 0.002

[a] Based on $n = 38$ and 61 sampling locations for the cosolvent and SPME studies, respectively. [b] $n = 3$.

(a)

ρ_{TMB} = -0.26
ρ_{dec} = -0.32
ρ_{und} = -0.32

NAPL removal efficiency

Local flux, L/min

□ 1,2,4-TMB △ n-decane ▽ n-undecane

(b)

ρ_{DCB} = -0.38
ρ_{undec} = -0.42

NAPL removal efficiency

Local flux, L/min

□ 1,2-DCB △ n-undecane
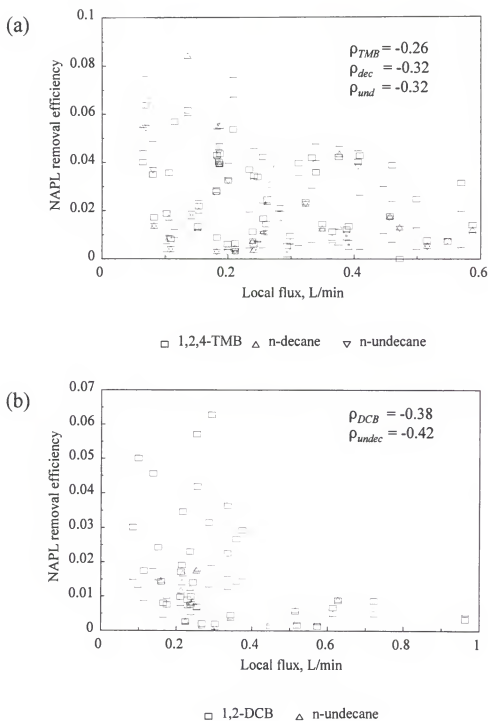
Figure 3-25. Correlation between NAPL removal efficiency and local flux measured at multilevel sampler locations in both the (a) SPME and (b) cosolvent test cells, with correlation coefficients, ρ, inset.

Discussion of NAPL Removal Efficiency

While remediation performance comparison can be difficult for multi-component NAPLs, the data presented here have demonstrated that neither cosolvent nor SPME flushing was markedly more efficient than the other; however, as the ultimate deciding factor is usually economics, the next level of decision-making would be to determine the cost per pore volume of flushing agent for each technology. Also, because these data have indicated that both technologies are subject to rate limitations, fluid flow rates and the resultant pore water velocities under which these technologies may be implemented are an important consideration. Greater NAPL removal efficiencies may be possible at lower flow rates than were used in these two studies, but the effect of longer flushing durations on total project costs must be considered.

CHAPTER 4
NUMERICAL MODELING OF LABORATORY- AND FIELD-SCALE ENHANCED AQUIFER REMEDIATION

Introduction

Nonequilibrium effects observed during NAPL dissolution generally result from diffusion caused by either large-scale heterogeneities in media properties and NAPL distribution, or local-scale mass transfer constraints. At local scales, mass transfer across fluid-solid or fluid-fluid interfaces within porous media is often diffusion-limited. Large-scale hydraulic conductivity variability results in a heterogeneous distribution of pore water velocities. High-velocity streamlines are likely to be exhibit lower solute concentrations than low-veolocity streamlines because of rate-limited mass transfer across interfaces. Solute concentrations will similarly vary among streamlines that contain either different amounts of NAPL, or NAPLs of different compositions. Concentration gradients between streamlines result in solute diffusion between streamlines. These diffusion effects are mechanistically similar to those described for rate-limited sorption processes (e.g., Brusseau et al. 1991). Augustijn (1993) noted that aqueous dissolution of multi-component NAPLs can be modeled as desorption because both processes involve solute diffusion through an organic phase (NAPLs for dissolution and soil organic matter for desorption). Large-scale diffusion limitations are also equivalent for both process. Finally, Augustijn (1993) noted that the

162

similarity between dissolution and desorption is particularly acute when the NAPL contains an insoluble pitch fraction, as was observed in the Hill AFB NAPL.

Here, the one-dimensional flow, cosolvent-enhanced desorption code of Augustijn et al. (1994) was adapted to model both cosolvent-enhanced dissolution and single-phase microemulsification of NAPLs. This model was applied to laboratory and field data from both the cosolvent and SPME flushing studies. Transport of the flushing agents was described with a one-dimensional advection-dispersion equation, wherein the effects of media heterogeneity were encompassed by the Peclet number, P. For the field experiment simulations, the superposition of two solute transport equations was used to characterize the more complex heterogeneities encountered at the field scale. Nonequilibrium dissolution/desorption was described using the bicontinuum approach, wherein a fraction, F, of the dissolution/desorption occurs instantaneously, and the remainder is characterized by a first-order mass transfer model.

Modeling Dissolution as Desorption

Upon the injection of a flushing agent into a contaminated porous medium, the effects of the flushing agent on contaminant sorption are reflected by changing values of R and the nonequilibrium parameters F and ω. Contaminant transport is modeled through the solution of the two-site nonequilibrium transport equations, (2-9) and (2-10), using finite difference techniques.

The following changes in the original model of Augustijn et al. (1994) were implemented for the simulation of NAPL dissolution: (1) the total retardation of each NAPL

constituent was calculated in terms of the constituent mass, (2) the log-linear effects of cosolvents on contaminant aqueous solubility and retardation were adapted to represent the linear effects of microemulsions, and (3) the effects of cosolvents on nonequilibrium sorption parameters were assumed to be identical for dissolution, but microemulsions were assumed to have no effect on nonequilibrium parameters. Each of these adaptations is discussed below.

<u>Representing Total Contaminant Mass With R</u>

The total mass of NAPL constituent c, M_c, contained within the pore volume of a NAPL-contaminated porous medium is equal to the sum of the mass in solution and the mass in the NAPL phase:

$$M_c = C_c(1 - S_N) + S_c^N S_N \tag{4-1}$$

where C_c is the aqueous concentration of the constituent, and S_c^N is the mass of the constituent per unit volume of NAPL. Assuming linear partitioning of the constituent between the aqueous and NAPL phases:

$$S_c^N = C_c K_N \tag{4-2}$$

Substitution of (4-2) into (4-1) and rearranging results in the following:

$$\frac{M_c}{C_c(1 - S_N)} = 1 + \frac{K_N S_N}{(1 - S_N)} \tag{4-3}$$

For a multi-component NAPL, the equilibrium aqueous concentration of an individual component is defined by Raoult's law:

$$C_c = \chi_c S_c^w \tag{4-4}$$

where χ_c is the mass fraction of the constituent in the NAPL. Recognizing the right side of (4-3) as being equivalent to (2-2), and substituting (4-4) into the left side, allows the expression of the retardation of c in water, R_c^w, in terms of the total constituent mass:

$$R_c^w = \frac{M_c}{\chi_c S_c^w (1 - S_N)} \tag{4-5}$$

The total constituent mass can be estimated from preflushing partitioning tracer data:

$$M_c^{pt} = \chi_c \rho_N S_N \tag{4-6}$$

or from BTCs measured during flushing:

$$M_c^{BTC} = \frac{m_0^c (1 - S_N)}{m_1^{np}} \tag{4-7}$$

Because the latter is a direct measure of the constituent mass, requiring no mass fraction conversions, this relation is preferred to the former, provided that dissolution data are available. Thus, in the simulations reported here, the retardation of c in water was determined by substituting (4-7) into (4-5):

$$R_c^w = \frac{m_0^c}{m_1^{np} \chi_c S_c^w} \tag{4-8}$$

Flushing Agent Effects on R

Cosolvents. The log-linear effect of the addition of organic solvents to water on the solubility of hydrophobic organic chemicals (HOC) has been well documented (e.g., Yalkowsky and Roseman, 1981; Pinal et al., 1990). The log-linear model states that the solubility of an HOC, here represented by a NAPL constituent, c, in a cosolvent mixture, S_c^m, is related to the aqueous solubility of the constituent as follows:

$$S_c^m = S_c^w 10^{\sigma f_c} \tag{4-9}$$

where f_c is the volume fraction of cosolvent and σ is a measure of the cosolvency power of the solvent and is determined from experimental measurements using (4-9). A similar relationship has also been observed for the equilibrium sorption coefficient of HOCs, here represented by K_N, (Rao et al., 1985; Nkedi-Kizza et al., 1985):

$$K_N^m = K_N^w 10^{-\sigma f_c} \tag{4-10}$$

Thus, the increased polarity of cosolvent mixtures results in higher solubilities and lower sorption coefficients for HOCs. Log transformation of (4-10) and substitution of (2-2) results in the following expression for cosolvency effects on R:

$$\log(R^m - 1) = \log(R^w - 1) - \alpha\beta\sigma f_c \tag{4-11}$$

where α and β are empirically determined parameters that account for the interactions between the cosolvent and the soil, and between the cosolvent and water, respectively (Rao et al., 1990). Here these interactions were assumed to be insignificant and values of one were used for both coefficients.

For ternary cosolvent mixtures, the cosolvent effects on R can be described by

$$\log(R^m - 1) = \log(R^w - 1) - (\sigma_1 f_{c_1} + \sigma_2 f_{c_2}) \qquad (4\text{-}12)$$

where the subscripts 1 and 2 refer to the two cosolvents, here ethanol and n-pentanol. Equation 4-12 can then be simplified:

$$\log(R^m - 1) = \log(R^w - 1) - \sigma^*(f_{c_1} + f_{c_2}) \qquad (4\text{-}13)$$

where σ^* is a weighted-average cosolvency power:

$$\sigma^* = \frac{\sigma_1 f_{c1} + \sigma_2 f_{c2}}{f_{c1} + f_{c2}} \qquad (4\text{-}14)$$

SPME. A given volume of SPME solution can be considered as some fraction, ϕ^μ, of micellar structures as depicted in Figure 2-1, with the remainder water. The total solubility of NAPL constituent c in a SPME solution can then be expressed as:

$$S_c^T = S_c^w + S_c^\mu \qquad (4\text{-}15)$$

where the superscript μ here refers to the micellar fraction of the aqueous volume. In contrast to cosolvent addition, and the log-linear increases in solubility described by (4-9), NAPL solubilization by microemulsions is more closely approximated by a linear model (e.g., Martel and Gélinas, 1996, Figure 11). Thus, the analogous linear form (4-9) for microemulsions is:

$$S_c^\mu = \phi^\mu \sigma^\mu S_c^w \qquad (4\text{-}16)$$

where σ^μ is a measure of the microemulsion solubilization capacity and is determined by substituting (4-16) into (4-15) . For the SPME study, the surfactant and alcohol comprised 5.5 wt% of the precursor solution (i.e., $\phi_0 = 0.055$), however, a normalized ϕ ($\phi = \phi^\mu/\phi_0$) was used to calculate σ^μ in the following equation and ϕ was thus set equal to one throughout this analysis:

$$\sigma^\mu = \frac{S_c^T}{S_c^w} - 1 \qquad (4\text{-}17)$$

If it is assumed that partitioning between the nonaqueous phase and the water and micellar fractions of the aqueous phases is linear, as described by the following:

$$S_c^N = K_N^w C_c^w = K_N^\mu C_c^\mu \qquad (4\text{-}18)$$

then substitution of concentration for solubility in (4-17) and combination with (4-18) results in the following expression for the effect of microemulsions on NAPL-water partitioning:

$$\frac{K_N^w}{K_N^\mu} = 1 + \phi \, \sigma^\mu \qquad (4\text{-}19)$$

Finally, substitution of (2-2) into (4-19) results in the following expression that was used in the numerical simulations to calculate the SPME effects on retardation:

$$R_c^\mu - 1 = \frac{R_c^w - 1}{1 + \phi \, \sigma^\mu} \qquad (4\text{-}20)$$

where, again, a value of one was used for ϕ.

Flushing Agent Effects on Nonequilibrium Parameters

Cosolvents. Brusseau et al. (1991) presented data which indicated that the first-order desorption rate coefficient, k_2, increased in a log-linear fashion with cosolvent fraction. The relationship between the Damkohler number, related to k_2 by (2-13), and cosolvent effects, modified for a ternary solvent mixture as described above, is then (Augustijn et al., 1994):

$$\log \omega^m = \log \omega^w + 0.668 \sigma^* (f_{c_1} + f_{c_2})$$ (4-21)

Brusseau et al. (1991) also found that the fraction of instantaneous sites, F, decreased with increasing cosolvent fraction. Augustijn et al. (1994) proposed the following relationship for cosolvent fractions above 20%:

$$F^m = F^w - \frac{(F^w - 0.01)}{0.8} (f_c - 0.2)$$ (4-22)

SPME. As described by Figure 2-1, the mechanisms of microemulsification are suspected to be external to the NAPL and, thus, the nonequilibrium parameters are expected to be independent of the microemulsion content for SPME flushing:

$$k_2^\mu = k_2^w \qquad F^\mu = F^w$$ (4-23)

Numerical Modeling Results

Laboratory Column Studies

Dai (1997), expanding on similar work by Johnson (1996), flushed columns packed with contaminated soil collected from the Hill AFB UF/EPA cosolvent field site with two

cosolvent mixtures: 70% ethanol/30% water and 70% ethanol/10% *n*-pentanol/20% water, all by volume. The latter mixture was very similar to that used for the 1995 field study. Rhue et al. (1999) flushed a laboratory column that was packed with contaminated soil from the Hill AFB SPME field site using the same precursor solution from the 1996 field study.

In both laboratory studies, pre- and postflushing partitioning tracer tests were used to assess the NAPL removal effectiveness of the flushing solutions. The preflushing nonpartitioning tracer BTCs from both studies were fit with an analytical solution to the one-dimensional advection-dispersion equation (Lapidus and Amundson, 1956). Measured BTCs from all three columns are shown with the model fits in Figure 4-1. The fitted Peclet numbers, P, are listed in Table 4-1 with other parameters that were constant for each column.

The mass of each constituent removed during flushing, determined from numerical integration of constituent BTCs, is listed in Table 4-2, along with the R_c^w values calculated from (4-10). Dai (1997) determined cosolvency powers for the ethanol/water mixture from (4-9) using NAPL-contaminated soil collected from the 1995 Hill AFB field site. The cosolvency powers for *n*-pentanol that are listed in Table 4-2 were measured in the presence of 70% ethanol using NAPL collected from the 1995 Hill AFB field site (Dai, 1997). Values of σ^* for the ethanol/*n*-pentanol/water mixture were calculated for input to the model using (4-14). Values of σ^μ for the SPME study were calculated from (4-17), however Rhue et al. (1999) used *n*-dodecane solubilization as an indicator for NAPL solubilization and, thus, values of S_c^T were not measured for the other constituents. Therefore, total solubilities in the precursor solution of the other constituents were scaled to the n-dodecane value ($S^T = 104$ mg/L) as follows:
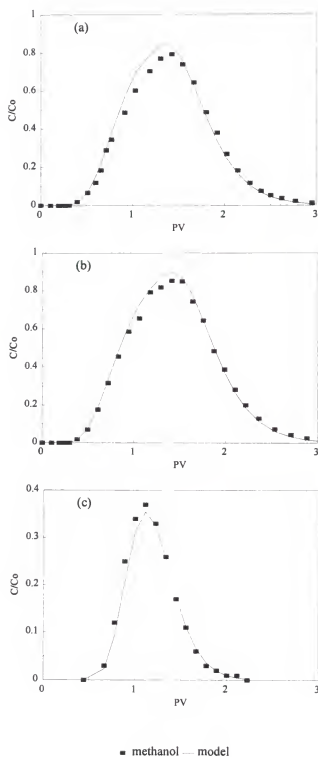
Figure 4-1. Preflushing nonpartitioning tracer BTCs with one-dimensional solute transport model fits for laboratory columns flushed with (a) 70% ethanol/30% water, (b) 70% ethanol/10% *n*-pentanol/20% water, and (c) SPME precursor solution.

Table 4-1. Hydrodynamic and nonequilibrium parameters for laboratory column cosolvent and SPME flushing experiments.

Flushing Solution	m_1^{np} (mL)	P	S_N	f_c/ϕ	F
70% Ethanol/30% Water	9.69	15	0.067	0.7	0.05
70% Ethanol/ 10% Pentanol/20% Water	9.89	20	0.070	0.8	0.05
SPME	10.36	36	0.060	1.0	0.8

Table 4-2. Nonequilibrium model input parameters for laboratory column cosolvent and SPME flushing experiments.

NAPL Constituent	m_0^c (mg)	[a] $\chi_c S_c^w$ (mg/L)	R_c^w	[b] σ / σ^μ	ω
Ethanol/Water					
1,2-dichlorobenzene	1.95	2.95E-1	6.82E+2	4.23	2.0E-2
1,3,5-trimethylbenzene	0.24	4.07E-3	6.12E+3	5.36	1.0E-3
n-undecane	6.73	5.62E-4	1.24E+6	8.35	2.5E-5
Ethanol/Pentanol/Water					
1,2-dichlorobenzene	1.97	2.95E-1	6.75E+2	3.97	2.0E-2
1,3,5-trimethylbenzene	0.20	4.07E-3	4.95E+3	6.65	1.0E-3
n-undecane	7.43	5.62E-4	1.34E+6	9.13	2.5E-5
SPME					
1,2,4-trimethylbenzene	1.64	2.50E-1	6.34E+2	2.60E+2	1.0
n-undecane	7.21	5.62E-4	1.24E+6	4.12E+5	1.0
n-dodecane	2.78	2.58E-5	1.04E+7	4.03E+6	1.0

[a] All solubilities, except 1,2,4-trimethylbenzene and n-dodecane, were determined from linear extrapolations of plots of log S_c^m vs ethanol fraction using NAPL-contaminated soil from the 1995 Hill AFB field site (Dai, 1997). Values for 1,2,4-TMB and n-dodecane determined using aqueous solubilities from Verschueren (1983) and mass fractions from Table 3-2. [b] Values for the ethanol/water mixture were measured from NAPL-contaminated soil from the 1995 Hill AFB field site, while values for the ethanol/n-pentanol/water mixture represent cosolvency power of n-pentanol in the presence of 70% ethanol and were measured from NAPL collected from the 1995 field site (Dai, 1997).

$$\sigma^{\mu} = \left(\frac{S_{dodecane}^{T}}{S_{c}^{w}} \right) \left(\frac{\chi_{c}}{\chi_{dodecane}} \right) - 1 \qquad (4\text{-}24)$$

The nonequilibrium parameters, F and ω, listed in Tables 4-1 and 4-2 were determined from fits of the model to measured BTCs and are discussed below.

Cosolvents. Breakthrough curves that were measured for 1,2-DCB, 1,3,5-TMB, and n-undecane during flushing with both cosolvent mixtures are shown in Figure 4-2. The results of these experiments indicated that the addition of a relatively small amount of a stronger solvent resulted in a significant reduction in the number of PVs required for nearly complete removal of the NAPL constituents.

The fits obtained using the bicontinuum nonequilibrium model are also plotted in Figure 4-2. The two nonequilibrium parameters, F and ω, generally control the BTC peak height and tail extent, respectively. The fraction of the NAPL that was instantaneously dissolved was assumed to be a function of the following variables: media geometry, NAPL distribution and morphology, and dissolution mechanism. Thus, because F was assumed to be independent of either the individual NAPL constituents or the cosolvent mixture, the value of F^{*} that was required to match the observed BTC peak heights was maintained for all constituents and for both cosolvent mixtures.

Initial estimates for the Damkohler number were obtained from the following empirical relationship between the equilibrium sorption coefficient, K, and the first-order rate coefficient that was presented by Augustijn (1993) based on earlier work by Brusseau and Rao (1989):

Figure 4-2. Measured and simulated BTCs from laboratory columns packed with contaminated soil from the 1995 Hill AFB field site and flushed with either 70% ethanol/30% water or 70% ethanol/10% *n*-pentanol/20% water.

$$\log k_2^w = 0.43 - 0.69 \log K \qquad (4\text{-}25)$$

where K_N was used here for K. However, the values of ω^w that produced the best fits to the data were approximately one order of magnitude lower than those estimated from (4-25). This phenomenon is discussed in greater detail below.

The ω^w values that were obtained from fitting the ethanol/water BTCs were also used to model ethanol/n-pentanol/water flushing. Thus, the model results for the ethanol/water experiment can be considered fits while the ethanol/n-pentanol/water model results are independent predictions. The model results matched the measured BTCs closely for both cosolvent mixtures, indicating that cosolvent-enhanced NAPL dissolution can be adequately represented by the bicontinuum sorption model of (2-9) and (2-10). These data also suggest that the cosolvent-enhanced dissolution of individual constituents from a multi-component NAPL can be modeled independently, provided that the appropriate σ values are used.

SPME. Breakthrough curves that were measured for 1,2,4-TMB, n-undecane, and n-dodecane during SPME flushing are presented in Figure 4-3. Because n-dodecane was the only constituent for which S_c^m was known *a priori*, F and ω were determined by fitting this BTC. Note that the value of F required to fit the SPME BTC peak heights was significantly higher than for cosolvent flushing (0.8 vs 0.05). Again, the same value of F was used for all constituents. However, here the best-fit value of ω for n-dodecane was also maintained for all constituents, whereas ω was different for each constituent for cosolvent flushing. The implications of this result are discussed below. The simulated and measured BTCs shown
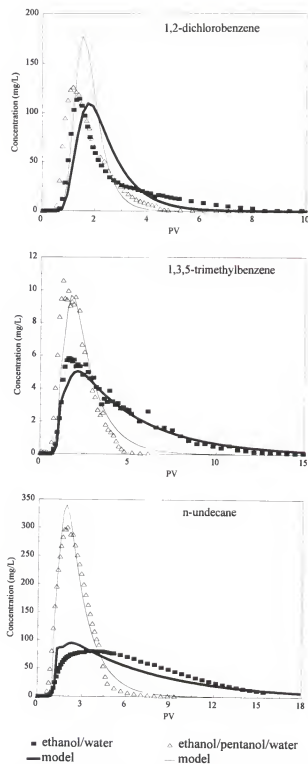
■ data   — nonequilibrium model
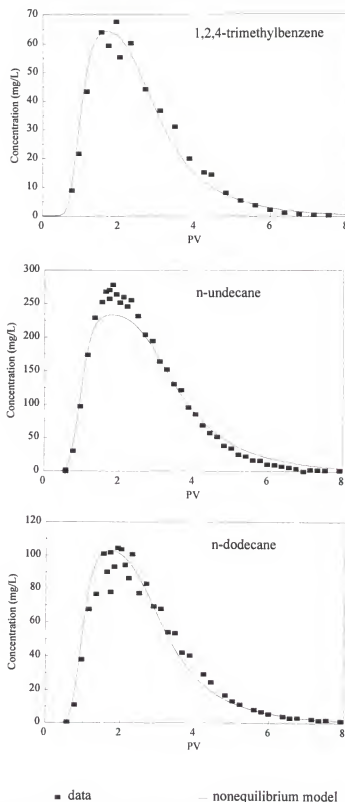
Figure 4-3.   Measured and simulated BTCs from laboratory columns packed with contaminated soil from the 1996 Hill AFB field site and flushed with the SPME precursor solution.

in Figure 4-3 agree closely, indicating that the two-site nonequilibrium desorption model can be used to model NAPL microemulsification.

    <u>Relationship between k_2 and K_N for cosolvents and microemulsions.</u> Values of k_2^w and K_N were calculated from ω^w and R_c^w for the cosolvent and SPME column studies using (2-13) and (2-2), respectively. These values are plotted on a log-log scale in Figure 4-4 along with the empirical relationship of Augustijn (1993), (4-25), determined from sorption of organic chemicals onto natural soils. For the SPME experiment, R_c^w values were calculated for all constituents listed in Table 3-2 (not all shown in Table 4-2) and $\omega^w = 1$ was used for each. For the cosolvent experiments, in addition to the data from Table 4-2, k_2^w and K_N values for o-xylene and n-decane from Dai (1997) are also included in Figure 4-4. The cosolvent data in Figure 4-4 followed a trend very similar to that predicted by the empirical approximation, except that the k_2^w values were approximately one order of magnitude lower for the dissolution of NAPL constituents than would have been predicted for the desorption of compounds with similar partitioning coefficients. This finding is consistent with observations made by Augustijn (1993), wherein sorption rate constants for benzene and toluene on an aged, coal tar contaminated soil from a manufactured gas plant site were found to be approximately one order of magnitude lower than those expected for natural sorbents. Augustijn (1993) hypothesized that the physical structure of the coal tar was relatively less open than that of soil organic matter, leading to more-restricted transport and lower rate constants for NAPL-contaminated soil than for soil organic matter.

    The good agreement between the slopes of the Augustijn (1993) regression line and that for the cosolvent data presented in Figure 4-2 indicates that the rate-limiting mechanism
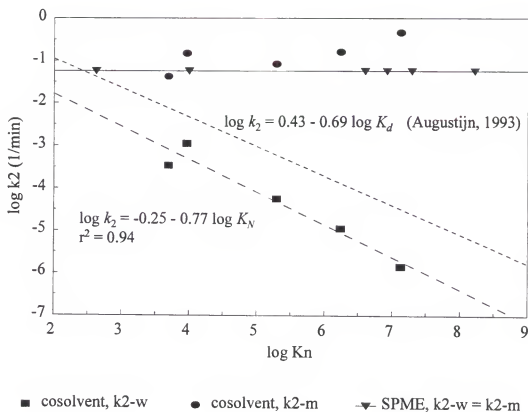
Figure 4-4. Correlation between first-order dissolution rate coefficient, k_2, and NAPL-water partitioning coefficient, K_N, for cosolvents and microemulsions. The correlation reported by Augustijn (1993) between desorption rate coefficient and soil-water distribution coefficient is also plotted for comparison.

for cosolvent-enhanced dissolution of multi-component NAPLs is similar to that of desorption. The elution of strongly hydrophobic constituents is more rate-limited than the dissolution of weakly hydrophobic constituents because: (1) the diffusion of the larger, and therefore more-hydrophobic, molecules through the organic phase is slower than that of smaller molecules, and (2) retardation within the organic phase is proportional to constituent hydrophobicity, causing delayed transport to the interface between the organic and aqueous phases for more-hydrophobic constituents.

The SPME k_2 values, however, were constant for all NAPL constituents and, thus, did not agree with the desorption regression. This result indicates that the rate-limiting mechanism for microemulsification is likely external to the organic phase and is, instead, more likely related to diffusion-limited constraints on access of the micelles to the interface between the organic and aqueous phases. The conclusion that k_2 is independent of the NAPL constituent is also consistent with the suggested mechanism of microemulsification (Figure 3-1), wherein droplets of the NAPL itself are encapsulated, as opposed to selective dissolution processes wherein individual NAPL constituent molecules are solubilized.

Finally, k_2^m values for the ethanol/n-pentanol/water cosolvent mixture are also plotted in Figure 4-4 for each NAPL constituent. These data are presented to illustrate that although the k_2^w values for aqueous dissolution are significantly lower than the corresponding SPME values, the log-linear relationship of (4-21) results in a dramatic reduction in the effect of mass transfer rate limitations in the presence of a relatively strong cosolvent.

<u>Field Studies</u>

The cosolvent and SPME field experiments were modeled using the solubilization and nonequilibrium parameters that were determined from the laboratory experiments. Therefore, the only additional parameters required to model the field experiments were those describing the field-scale hydrodynamics. The field-scale behavior of the flushing agents was modeled using the superposition of two transport equations, and the dissolution behavior was similarly modeled using the superposition of two solutions to (2-9) and (2-10). This approach is conceptually equivalent to considering each field test cell as a two-layer system. Thus, model predictions were obtained for each layer using identical input parameters except P, and the resulting BTCs were fractionally superposed.

<u>Cosolvent</u>. In order to minimize flow instabilities induced by contrasts in the bulk fluid properties between the flushing solution and the resident groundwater, a gradient injection program was implemented to deliver the cosolvent mixture over a period of approximately one PV (Jawitz, 1995; Rao et al., 1997). During the gradient injection, a binary ethanol/water solution was used. To avoid phase separation, n-pentanol was not introduced until one PV after the ethanol reached the targeted fraction in the injection fluid.

Both the graded injection of ethanol and the delayed injection of n-pentanol complicated modeling of the field cosolvent flushing experiment. Because of the gradient injection program, accurately describing the flushing solution front required the incorporation of a model that exhibited enhanced spreading beyond that which was representative of the aquifer material heterogeneity. Therefore, instead of using the preflushing nonpartitioning tracer BTC to describe the propagation of the flushing solution,

a fit to the ethanol elution profile was obtained using the superposition of two lognormal distributions. Because the ethanol BTCs from all three EWs were similar, a single fit was used (Figure 4-5). Equivalent P values for each BTC mode, calculated by equating the first two moments for the lognormal and ADE models (Table 2-1), are presented in Table 4-3 along with the fractional contribution, f, of the first mode.

The sequential injection of relatively weaker and stronger solvents resulted in enhanced chromatographic separation of the NAPL constituent BTCs (Rao et al., 1997; Sillan et al., 1998). Breakthrough curves presented by these authors indicated that the least hydrophobic constituents (e.g., xylenes and 1,2-DCB) were eluted by the ethanol/water cosolvent mixture, while the most hydrophobic constituents (e.g., n-undecane) were not removed until n-pentanol was injected. Therefore, the following modeling approach was implemented here. One representative NAPL constituent was selected from both the less-hydrophobic constituents (1,2-DCB) and the more-hydrophobic constituents (n-undecane). The elution of 1,2-DCB and n-undecane were modeled using the cosolvency powers measured for 70% ethanol/30% water and 70% ethanol/10% n-pentanol/20% water, respectively. Also, because the injection of n-pentanol was initiated after 1.82 d (corresponding to 1.37 PV, 1.86 PV, and 1.60 PV for EWs 1, 2, and 3, respectively), the arrival times of the modeled n-undecane BTCs were proportionately delayed.

The measured BTCs for 1,2-DCB and n-undecane from each EW are presented in Figure 4-6, along with the corresponding model predictions. The nonequilibrium model parameters are listed in Table 4-4. The model predictions match the data well, especially considering that all of the model input parameters except P were determined from laboratory
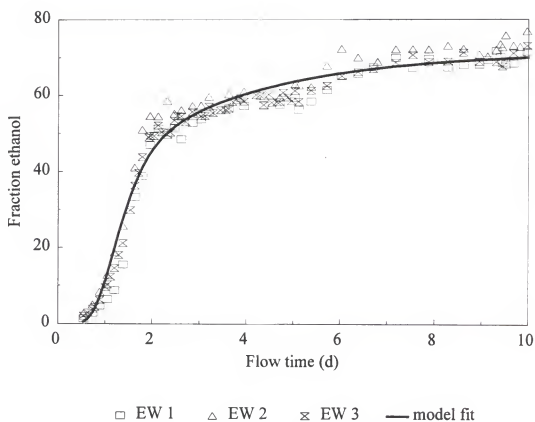
Figure 4-5. Ethanol elution profile at all three extraction wells (EWs) from the cosolvent field study, with a model fit from the superposition of two lognormal distributions.

Table 4-3. Hydrodynamic parameters for the cosolvent and SPME flushing field experiments.

Experiment	P_1	P_2	f
Cosolvent (same for all EWs)	15.3	2.65	0.60
SPME			
EW 1	19.3	4.09	0.65
EW 2	44.7	2.0	0.20
EW 3	23.4	1.68	0.45

Figure 4-6. Measured BTCs and nonequilibrium model predictions for the elution of 1,2-dichlorobenzene (1,2-DCB) and *n*-undecane from all three EWs of the cosolvent field study.

Table 4-4. Nonequilibrium model input parameters for selected NAPL constituents from the cosolvent and SPME flushing field experiments.

	Cosolvent		SPME	
Parameter	1,2-DCB	n-undecane	p-xylene	n-dodecane
ω^w	2.0E-2	2.5E-5	1.0	1.0
F^w	0.05	0.05	0.8	0.8
$\sigma^\dagger$	4.23	8.46	7.43E+1	4.03E+6
f_c / ϕ	0.72	0.82	1.0	1.0
R^w				
EW 1	6.81E+2	9.61E+5	1.65E+2	8.62E+6
EW 2	8.17E+2	1.27E+6	1.54E+2	1.06E+7
EW 3	1.07E+3	1.47E+6	1.59E+2	7.25E+6

$\dagger$ The cosolvency power for 1,2-DCB is from the 70%ethanol/30% water mixture, while the n-undecane value was determined from (4-14) using the values from Table 4-2 for both cosolvent mixtures. The σ value for n-dodecane is from Table 4-2, while the p-xylene data was calculated from (4-24) with $S_{p\text{-}xylene}^w = 198$ mg/L (Verscheuren, 1983).

measurements. At all three EWs, *n*-undecane elution began before the model predicted, largely because some *n*-undecane was removed by the ethanol/water solution.

SPME. The preflushing nonpartitioning tracer BTCs from all three extraction wells of the SPME field experiment were fit with the superposition of two lognormal distributions using the lognormal truncated moment approach (see Appendix B). The resulting equivalent P values and fractional contribution of the first mode are listed for each EW in Table 4-3. The measured BTCs and model predictions for 1,2,4-TMB and *n*-undecane are presented for each EW in Figure 4-7, and, again, the model predictions matched the data well.

Effect of Assuming Equilibrium Dissolution

The large degree of heterogeneity, and the correspondingly low P values, encountered at the field scale leads to the question of whether NAPL constituent BTC spreading is dominated by hydrodynamic considerations. Thus, the relative impacts of media heterogeneity, here characterized by P, and dissolution rate constant were considered. Presented in Figure 4-8 are selected constituent BTCs from the cosolvent and SPME laboratory column studies with corresponding model fits wherein it was assumed that dissolution was not rate-limited (i.e., $F^w = 1.0$). Similar BTCs for the field studies are presented in Figure 4-9. For cosolvent flushing, the NAPL constituents with relatively fast mass-transfer rates (i.e., high k_2^w values) were less affected by assuming equilibrium dissolution than those subject to slow mass transfer. For SPME flushing, which was subject to relatively weak nonequilibrium conditions, the effect of assuming equilibrium dissolution was smaller than that observed for cosolvent flushing. The combination of these effects

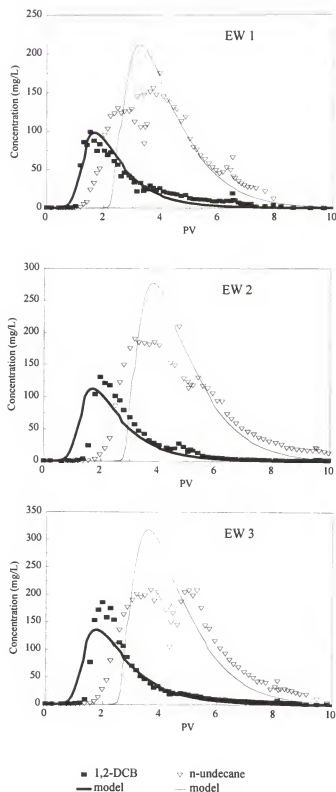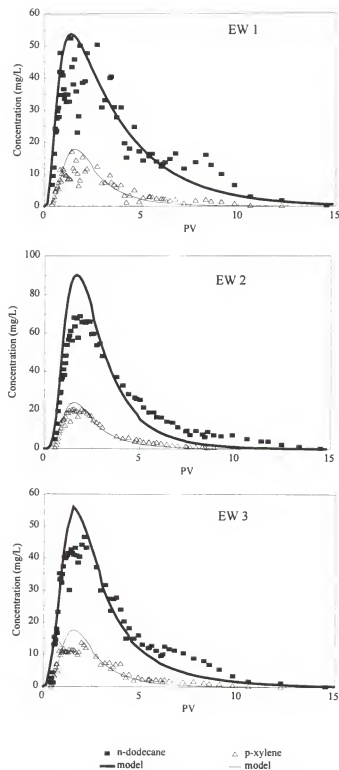Figure 4-7. Measured BTCs and nonequilibrium model predictions for the elution of *p*-xylene and *n*-dodecane from all three EWs of the SPME field study.
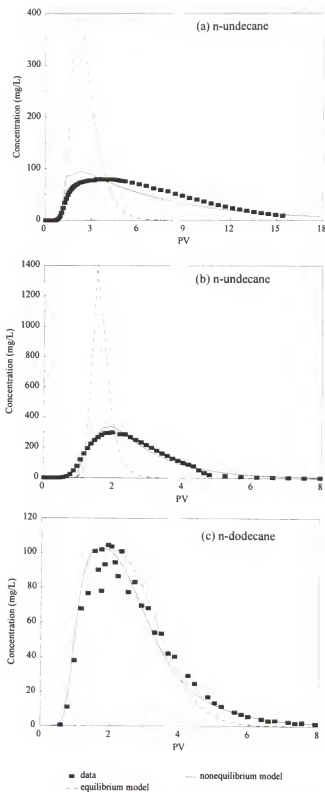
Figure 4-8. Measured BTCs compared to nonequilibrium and equilibrium model predictions for laboratory columns flushed with (a) 70% ethanol/30% water, (b) 70% ethanol/10% *n*-pentanol/20% water, and (c) SPME precursor solution.
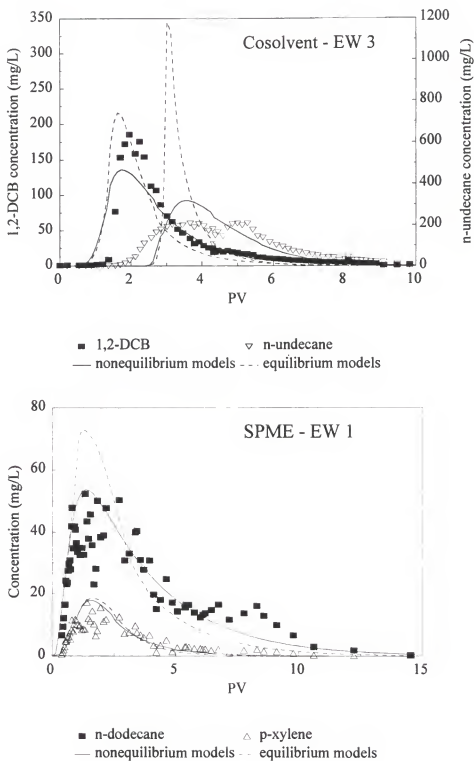
Figure 4-9. Measured BTCs compared to nonequilibrium and equilibrium model predictions from EW 3 and EW 1 for the cosolvent and SPME field experiments, respectively.

resulted in a poor fit to the field cosolvent flushing data for *n*-undecane when equilibrium dissolution was assumed, whereas errors associated with assuming equilibrium dissolution were much smaller for cosolvent flushing of 1,2-DCB and SPME flushing for all constituents.

Conclusions

The first-order rate constants estimated here for cosolvent-enhanced solubilization and single-phase microemulsification supported the conclusion that the NAPL solubilization mechanisms for these two processes were different. Solubilization of individual constituents by cosolvents was limited by the rate of diffusion or transport of the component through the organic phase, while the rate-limiting step for microemulsification was independent of the NAPL constituent and was likely external to the organic phase. In addition, cosolvent-enhanced solubilization was rate-limited for most of the NAPL (95%), while only 20% was rate-limited for microemulsification. Also, the solubilization rate constants are functions of both solvent strength and concentration in solution, but are likely functions only of access to the organic/aqueous phase interface for a given microemulsion precursor and are thus independent of the concentration of the precursor in solution. The data presented here have shown that by accounting for field-scale hydrodynamic variability, laboratory-measured nonequilibrium parameters can be used to accurately predict field-scale nonequilibrium NAPL solubilization. Finally, the effects of field-scale media heterogeneity are likely to dominate those of weakly rate-limited dissolution, and accurate characterization of the former may be sufficient for adequate prediction of field-scale NAPL solubilization.

CHAPTER 5
CONCLUSIONS

A method was described for the use of partitioning tracer BTC moments to ascertain information related to the spatial distribution of NAPLs within a given swept volume. The swept volume was considered as a bundle of streamtubes, some fraction of which were contaminated. Two different models were developed: In the first model, the NAPL saturation in each contaminated streamtube was assumed to be the same; in the second model, the NAPL saturations in the contaminated streamtubes were assumed to be distributed lognormally. One-dimensional numerical simulations validated that the parameters describing the distribution of NAPL saturations could be determined for both models using tracer BTC moments. In addition, two-dimensional numerical simulations were conducted to investigate the impact of a correlation between NAPL saturation and nonpartitioning tracer travel time, which was considered to be approximately inversely proportional to hydraulic conductivity. These simulations indicated that for correlated cases, tracer BTC moments could still be used to determine the fraction that was contaminated, but an adequate initial estimate of the correlation coefficient was required to determine the distribution of the NAPL within the contaminated zone.

Laboratory experiments were conducted to examine the underlying assumptions in the homogeneous binary NAPL distribution model. For the low-saturation cases

investigated, the ability to determine what fraction of the domain was contaminated was only marginally impacted by flow bypassing. Also, the effects of nonlinear partitioning did not seem to affect the results for the NAPL and tracers used. However, rate-limited partitioning was a factor, leading to excess spreading of the partitioning tracer BTC within the contaminated zone. This effect limits the ability to describe the NAPL spatial distribution within the contaminated zone without also accounting for nonequilibrium effects. However, the ability to determine the fraction of the domain that was contaminated was only marginally affected.

Tracer BTCs measured from two field experiments were used to estimate the NAPL spatial distribution at each site. The true distributions were unknown, but the estimated contaminated fractions were in qualitative agreement with data from soil cores. The distribution of saturations within the contaminated zone that was estimated at one of the sites was compared to a CDF created from the soil core data. The soil core CDF showed more variability than the distribution estimated from the tracer BTCs, supporting the finding from the numerical simulations that the point variability of a parameter is damped out by integration along a streamline.

These results are significant for the design of *in situ* flushing remediation systems because the delivery of flushing fluids to uncontaminated zones is both inefficient and expensive. More efficient and less expensive remediation designs can be implemented if the fraction of the swept zone that is uncontaminated can be ascertained. The determination of the NAPL saturation distribution within the contaminated zone is also useful; however,

estimates of the distribution parameters may be influenced by nonequilibrium tracer partitioning or possible correlations between NAPL saturation and hydraulic conductivity.

A field-scale *in situ* flushing NAPL source zone remediation experiment was described. The flushing solution consisted of a surfactant/alcohol mixture that was designed to solubilize the NAPL as a single-phase microemulsion. The performance of the field experiment was evaluated in terms of the remediation effectiveness and efficiency at two scales: the flushed-zone-average scale and the control plane scale. In addition, the efficiency of the SPME flood was compared to that of an earlier cosolvent flood at a similar site.

Soil core data indicated that approximately 90-95% of the most prevalent NAPL constituents were removed from the flushed zone by the SPME flood. A comparison of pre- and post-flushing partitioning tracer data indicated that about 72% of the measured NAPL volume was removed by the SPME flood. Integration of NAPL constituent BTCs measured at the EWs indicated 55-75% removal of the target NAPL constituents, when partitioning tracer data were used to estimate the initial amount of NAPL present; and 60-175% removal of two target constituents when soil core data were used to estimate the amount of NAPL initially present. Data from partitioning tracer and NAPL constituent BTCs measured at the MLSs were averaged at successive control planes, resulting in good agreement with the EW data. The implication of these results is that the SPME flood effectively removed the NAPL constituents of concern, but an insoluble anthropogenic residue may have been left behind.

The data presented here have demonstrated that neither cosolvent nor SPME flushing was markedly more efficient than the other. However, the numerical simulations of enhanced aquifer remediation supported the conclusion that the NAPL solubilization

mechanisms for these two processes were different. Solubilization of individual constituents by cosolvents was limited by the rate of diffusion or transport of the component through the organic phase, while the rate-limiting step for microemulsification was external to the organic phase and all constituents were eluted essentially simultaneously. Because the multilevel sampler data and numerical simulation results indicated that both technologies are subject to rate limitations, fluid flow rates and the resultant pore water velocities under which these technologies may be implemented are an important consideration. Greater NAPL removal efficiencies may be possible at lower flow rates than were used in these two studies, but the effect of longer flushing durations on total project costs must be considered.

Finally, the field data presented here have shown that accurate characterization of the hydrodynamic variability within a given swept volume facilitates both the characterization of the NAPL saturation distribution and the prediction of NAPL solubilization. Partitioning tracer higher moments can be used to estimate the fraction of the streamtubes that are contaminated and laboratory-measured nonequilibrium parameters can be used to predict field-scale nonequilibrium NAPL solubilization.

APPENDIX A
GENERAL EXPRESSION FOR THE MOMENTS OF THE PRODUCT
OF CORRELATED LOGNORMAL RANDOM VARIABLES

The product, A, of two lognormal random variables, X and Y, is also a lognormal

random variable (Jury and Roth, 1990):

$$A = XY \qquad \mu_A = \mu_X + \mu_Y, \ \sigma_A^2 = \sigma_X^2 + \sigma_Y^2 + 2\rho\sigma_X\sigma_Y \qquad \text{(A-1)}$$

For the general case of $X^a Y^b$, let us consider each random variable separately (e.g., X^a). For

$a = 2$, (A-1) indicates that the product of X and X is a lognormal random variable, B:

$$B = X \cdot X \qquad \mu_B = 2\mu_X, \ \sigma_B^2 = \sigma_X^2 + \sigma_X^2 + 2\sigma_X\sigma_X = 4\sigma_X^2 \qquad \text{(A-2)}$$

where $\rho = 1$ (i.e., perfect correlation between X and X). Extending this approach to the

product BX, equivalent to $a = 3$, produces another lognormal random variable, C:

$$C = BX = X^3 \qquad \mu_C = \mu_B + \mu_X = 3\mu_X, \ \sigma_C^2 = \sigma_B^2 + \sigma_X^2 + 2\sigma_B\sigma_X = 9\sigma_X^2 \qquad \text{(A-3)}$$

Thus, (A-1) can be iteratively applied with the following general form:

$$Z = X^a \qquad \mu_Z = a\mu_X, \ \sigma_Z = a\sigma_X \qquad \text{(A-4)}$$

Also according to (A-1), if $Z = X^a$ is a lognormal random variable, then the product $X^a Y^b$ is

also a lognormal random variable, P:

$$P = X^a Y^b \qquad \mu_P = a\mu_X + b\mu_Y, \ \sigma_P^2 = a^2\sigma_X^2 + b^2\sigma_Y^2 + 2\rho ab\sigma_X\sigma_Y \qquad \text{(A-5)}$$

The expected value of P can then be determined from the lognormal distribution first moment (Table 2-1):

$$\text{E}[P] = \text{E}[X^a Y^b] = m_1^P = \exp\left(a\mu_X + b\mu_Y + \frac{a^2\sigma_X^2 + b^2\sigma_Y^2 + 2ab\sigma_X\sigma_Y}{2}\right) \qquad \text{(A-6)}$$

which is equivalent to

$$\text{E}[X^a Y^b] = \exp\left(a\mu_X + \frac{a^2\sigma_X^2}{2}\right)\exp\left(b\mu_Y + \frac{b^2\sigma_Y^2}{2}\right)\exp\left(\frac{2ab\rho\sigma_X\sigma_Y}{2}\right) \qquad \text{(A-7)}$$

Finally, (A-7) can be simplified to the following general expression for the moments of the product of two correlated lognormal distributions:

$$\text{E}[X^a Y^b] = m_a^X m_b^Y \exp(ab\rho\sigma_X\sigma_Y) \qquad \text{(A-8)}$$

APPENDIX B
EXAMPLE APPLICATIONS OF LOGNORMAL DISTRIBUTION
TRUNCATED TEMPORAL MOMENT EXPRESSIONS

First Lord. How mightily sometimes we make us comforts of our losses!
Second Lord. And how mightily some other times we drown our grain in
tears!

All's Well That Ends Well

Accurate parameter estimation using the method of moments for incomplete lognormal distributions requires the solution of (2-55) through iterative regression for μ and σ. The regression criterion that was minimized when solving (2-55) was the root mean squared deviation, RMSD, between the measured and computed truncated moments:

$$\text{RMSD} = \left[\frac{1}{p} \sum_{i=1}^{p} \left(\frac{m_i^{\,m} - m_i^{\,c}}{m_i^{\,m}} \right)^2 \right]^{\frac{1}{2}} \tag{B-1}$$

where the superscripts m and c represent measured and computed values, respectively, and p is the number of moments used. Only two moment equations are required to provide estimates of μ and σ using (2-55) and (B-1), however, for cases where the model does not provide an exact fit to the measured data, inclusion of the third moment provides an additional constraint on the regression and places extra emphasis on the late-time data. Because accurate estimation of both lower and higher order moments requires consideration of both early- and late-time data (i.e., BTC peak and tail portions, respectively), the first

198

three temporal moments were used in (2-55) and (B-1). All nonlinear regressions presented here were performed using the optimizing routine from a spreadsheet software package (Corel Quattro Pro).

Superposition

The Nth normalized moment of a BTC formed from the superposition of n transport equation solutions can be expressed as follows:

$$m_{N_T} = \sum_{i=1}^{n-1} (F_i \, m_{N_i}) + (1 - \sum_{i=1}^{n-1} F_i) m_{N_n} \qquad n > 1 \qquad \text{(B-2)}$$

where F_i represents the fractional contribution from the ith portion of the domain. This approach is conceptually equivalent to representing the domain as a non-interacting layered system. Expansion of the general superposition relation of (B-2) for the TME of (2-55) results in the following bi-lognormal (Bi-LN) and tri-lognormal (Tri-LN) moment expressions ($n = 2$ and 3, respectively):

$$m_{N_T}(t_{max}) = f_1 \exp(N\mu_1 + N^2\sigma_1^2/2) \frac{1}{2}\left[\text{erf}\left(\frac{y(t_{max})_1 - N\sigma_1}{\sqrt{2}}\right) + 1\right]$$
$$+ (1 - f_1)\exp(N\mu_2 + N^2\sigma_2^2/2) \frac{1}{2}\left[\text{erf}\left(\frac{y(t_{max})_2 - N\sigma_2}{\sqrt{2}}\right) + 1\right] \qquad \text{(B-3)}$$

$$m_{N_T}(t_{max}) = f_1 \exp(N\mu_1 + N^2\sigma_1^2/2) \frac{1}{2}\left[\text{erf}\left(\frac{y(t_{max})_1 - N\sigma_1}{\sqrt{2}} \right) + 1 \right]$$

$$+ f_2 \exp(N\mu_2 + N^2\sigma_2^2/2) \frac{1}{2}\left[\text{erf}\left(\frac{y(t_{max})_2 - N\sigma_2}{\sqrt{2}} \right) + 1 \right] \quad \text{(B-4)}$$

$$+ (1 - f_1 - f_2) \exp(N\mu_3 + N^2\sigma_b^2/2) \frac{1}{2}\left[\text{erf}\left(\frac{y(t_{max})_3 - N\sigma_3}{\sqrt{2}} \right) + 1 \right]$$

where t_i was considered to be zero (this assumption was made for all cases considered here).

Nonlinear Regression and Exponential Extrapolation

The nonlinear regression (NLR) method involves the selection of the set of model parameters which minimizes the discrepancy between the measured data and a model. The selection of an appropriate criterion to quantify the model fit is a subject that has received considerable attention (e.g., Aitchison and Brown, 1957; Anderssen and White, 1970; Stedinger, 1980; Jury and Sposito, 1985). The criterion used by Helms et al. (1999) to fit incomplete BTC data was to minimize the sum of the squares of the differences between the measured and computed concentration values, or the sum of the squared residuals (SSR). However, the SSR quantifies absolute concentration differences and is thus biased towards higher concentration values. The RMSD criterion, which quantifies relative differences, was used here, where C was replaced by m in (B-1). The RMSD criterion, however, may be biased towards portions of the BTC characterized by very steep slopes, such as during the initial rise in the frontal limb. Therefore, frontal limb data points of $C/C_0 < 0.001$ were excluded from the regressions performed here.

Model parameters are determined using the exponential extrapolation method by matching the complete moment expressions determined from (2-56) to the sums of the numerically integrated moments of the incomplete BTC, $m_N(0, t_{max})$, and the moments of an exponential extrapolation of the BTC tail data, $m_N(t_{max}, \infty)$:

$$m_N = m_N(0, t_{max}) + m_N(t_{max}, \infty) \tag{B-5}$$

The moment equations for the exponentially extrapolated fraction are presented elsewhere (Helms et al., 1999).

Synthetic Data Set Examples

The synthetic cases presented here were created to represent a range of BTC complexity. The simplest synthetic BTC was generated from the dimensionless form of the Lapidus and Amundson (1952) solution to the one-dimensional, flux-averaged ADE for a pulse input of solute in a semi-infinite domain that was presented by van Genuchten and Alves (1982). The second synthetic case was generated through the superposition of three ADE analytical solutions (Tri-ADE) in order to represent a more complicated flow domain. The superposition was performed as described by (B-2), with m_N replaced by the relative concentration, $C(t)/C_0$. Finally, the third synthetic BTC was created using the two-site nonequilibrium advection-dispersion transport model (Nkedi-Kizza et al., 1984). This model was selected because of its ability to describe both physical and chemical nonequilibrium solute transport, characterized by a first-order mass transfer step, while producing the desired BTC characteristics representative of field-scale transport, namely a relatively sharp peak followed by an elongated tail. The governing equations for this model, (2-9) and (2-10),

were solved using the numerical code UFBTC (Jessup and Rao, 1990). The first three pulse-corrected, normalized temporal moment equations for both the equilibrium and nonequilibrium ADEs are presented in Table 2-1.

Each synthetic BTC was treated as a pulse input of $t_0 = 0.15$ pore volumes (PV). Also, each synthetic BTC was truncated at the time corresponding to either $C/C_0 = 0.001$, a value which may be a practical limit for many tracer experiments with C_0 values on the order of 1000 mg/L and analytical detection limits on the order of 1 mg/L (see Chapter 3; Annable et al., 1998), or $t = 5$ pore volumes (PV), depending on which occurred sooner. For each synthetic case, the true values of the first three complete temporal moments were compared to the estimated values obtained from numerical integration of the truncated BTC, exponential extrapolation, NLR, and TMEs. The measured truncated moments were normalized by the true complete zeroth moments. Similarly, NLR of (2-14) was performed using the true complete t_0 values. The values for the complete moment estimates from the NLR and TME methods were determined from the lognormal moment equations shown in Table 2-1 using the optimized lognormal parameters. The error in the complete moment estimates was determined from the RMSD between the estimated and true values for the first three moments. Also, BTCs generated with the model parameters estimated from each method were compared to the synthetic data for each case.

Case 1: Single ADE. The synthetic BTC shown in Figure B-1a was created from the ADE analytical solution with $P = 15$ and $R = 2$. Truncation at a relative concentration of 0.001 corresponded to $t = 4.8$ PV and the arrival of 99.6% of the input mass.
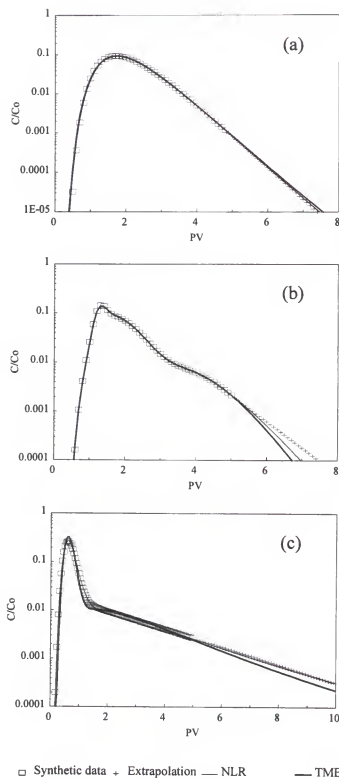
Figure B-1. Truncated synthetic BTCs with lognormal NLR and TME fits and exponential extrapolation for (a) single ADE, (b) superposition of three ADEs, and (c) nonequilibrium ADE models.

The true moments, determined from the equations presented in Table 2-1 using the parameters given above, are compared to the values determined from each estimation method in Table B-1. The three different RMSD criteria listed in Table B-1 represent the deviation between the model and the truncated data, the truncated moments of the model and the moments of the truncated data, and the complete moments of the model and the complete moments of the data, respectively. A comparison of the Complete Moments RMSD criteria indicates that the application of the ordinary method of moments to the incomplete data provided the least accurate estimates of the true moments, while NLR improved the estimates and the exponential extrapolation and truncated moment methods both provided very good estimates. The BTCs generated using the optimized NLR and TME model parameters both matched the data well and were nearly indistinguishable from each other (Figure B-1a).

Case 2: Tri-ADE. The parameters used to create the second synthetic BTC (Figure B-1b) are listed in Table B-2. Truncation at $t = 5.0$ PV corresponded to a relative concentration of 0.002 and the arrival of 99.2% of the input mass.

The example presented above (Case 1), and those presented by Helms et al. (1999), demonstrate that model parameters and complete moments for truncated synthetic BTCs can be recovered through the application of NLR or TME methods which incorporate either the same model that was used to generate the data, or mathematically similar models (e.g., lognormal and ADE). The purpose of the next two examples is to examine the utility of these moment estimation methods when using less appropriate models. Therefore, the Tri-ADE data set moments were estimated using single, bi-, and tri-lognormal NLR and TME methods, in addition to exponential extrapolation.

Table B-1. True and estimated moments and estimation errors for the synthetic examples.

Estimation Method	Moments			RMSD Criteria		
	m^1	m^2	m^3	Truncated Data	Truncated Moments	Complete Moments
Case 1: Single ADE						
Complete data	2.08	4.84	12.69	-	-	-
Incomplete, t_{max} = 4.8 PV	2.05	4.72	12.03	-	-	0.034
Extrapolation	2.08	4.84	12.71	-	-	0.001
NLR: Single LN	2.09	4.91	12.90	0.048	1.33E-2	0.014
TME: Single LN	2.08	4.85	12.76	0.090	1.37E-4	0.003
Case 2: Tri-ADE						
Complete data	1.93	4.41	12.13	-	-	-
Incomplete, t_{max} = 5.0 PV	1.89	4.15	10.67	-	-	0.079
Extrapolation	1.95	4.55	13.08	-	-	0.049
NLR: Single LN	2.02	4.53	11.25	0.496	6.40E-2	0.052
Bi-LN	1.99	4.80	14.64	0.123	9.21E-3	0.131
Tri-LN	1.94	4.43	12.24	0.019	1.28E-4	0.006
TME: Single LN	1.92	4.38	11.95	2.693	3.11E-3	0.011
Bi-LN	1.97	4.67	13.96	0.226	1.98E-5	0.094
Tri-LN	1.94	4.42	12.21	0.022	1.33E-5	0.004
Case 3: ADE Nonequilibrium						
Complete data	1.28	4.17	27.13	-	-	-
Incomplete, t_{max} = 5.0 PV	0.97	1.71	4.78	-	-	0.601
Extrapolation	1.28	4.22	27.81	-	-	0.016
NLR: Tri-LN	1.30	4.72	40.44	0.027	6.33E-4	0.293
TME: Tri-LN	1.22	3.76	25.23	0.215	3.65E-4	0.075

Table B-2. True and estimated model parameters for the synthetic examples.

				Model Parameters				
	ADE:	R_1	P_1	f_1	R_2	P_2	f_2	R_3	P_3
Estimation Method	LN:	μ_1	σ_1	f_1	μ_2	σ_2	f_2	μ_3	σ_3
Case 1: Single ADE									
True (ADE)		2.0	15.0	1.0	-	-	-	-	-
True (LN)		0.67	0.34	1.0	-	-	-	-	-
NLR - Single LN		0.68	0.34	1.0	-	-	-	-	-
TME - Single LN		0.67	0.34	1.0	-	-	-	-	-
Case 2: Tri-ADE									
True (ADE)		1.25	169	0.19	1.82	19.3	0.75	4.0	50.0
True (LN)		0.28	0.11	0.19	0.60	0.30	0.75	1.39	0.20
NLR: Single LN		0.65	0.32	1.0	-	-	-	-	-
Bi-LN		0.48	0.25	0.73	0.97	0.41	-	-	-
Tri-LN		0.27	0.12	0.20	0.60	0.30	0.73	1.37	0.21
TME: Single LN		0.56	0.42	1.0	-	-	-	-	-
Bi-LN		0.45	0.21	0.70	0.96	0.39	-	-	-
Tri-LN		0.28	0.12	0.20	0.60	0.30	0.73	1.37	0.20
Case 3: ADE Nonequilibrium									
NLR: Tri-LN		-0.44	0.31	0.60	-0.46	0.21	0.17	0.95	0.72
TME: Tri-LN		-0.45	0.25	0.41	-0.46	0.21	0.37	0.93	0.65

A comparison of the Truncated Data RMSD criteria in Table B-1 indicates that as the model complexity increased, the fit to the data improved for both the NLR and TME methods, with the NLR fits producing the smallest deviations. A similar trend was observed with the Truncated Moments RMSD criteria, with the TME method producing the smallest deviations. The Complete Moments RMSD criteria revealed that, for both the NLR and TME approaches, only the Tri-LN models produced more accurate estimates than the exponential extrapolation method, with the Bi-LN models providing worse estimates than would have been obtained from the application of the ordinary method of moments to the incomplete data. However, the Complete Moments RMSD criteria also indicate that, at each level of model complexity, better moment estimates were obtained from the TME method than from the NLR method. Only the Tri-LN model fits are shown in Figure C-1b, and again both the NLR and TME methods provided good fits to the data.

Case 3: Nonequilibrium ADE. The following dimensionless parameters were used to generate the third synthetic BTC (Figure B-1c): $P = 20$, $R = 1.2$, $\beta = 0.5$, and $\omega = 0.3$. These parameters were selected to create an asymmetric BTC characterized by an early peak and extensive tailing. Truncation at $t = 5.0$ PV corresponded to a relative concentration of 0.003 and the arrival of 95.8% of the input mass.

The Tri-LN models provided better fits to the synthetic data than did the single and Bi-LN models, for both the NLR and TME methods, and thus only the Tri-LN results are shown in Table B-1 and Figure B-1c. Note that the TME method produced significantly better moment estimates than the NLR method. However, because the nonequilibrium model is based on a first-order mass transfer assumption, the tail portion of the synthetic BTC is

well approximated by an exponential decay, and the exponential extrapolation method thus produced the best estimates of the true moments.

Conclusions

As BTC data measurement durations become infinite and relative concentrations approach zero, moment estimates obtained from numerical integration approach the true moment values. However, in many real applications experiment durations are limited and BTCs are truncated, leading to erroneous results when the ordinary method of moments is applied. Thus, the use of truncated moment expressions is suggested. The TME method was compared to other moment estimation methods which also require the selection of a model in order to extrapolate beyond the measured data. For all cases presented here, the models selected to fit the data were similar to, but not exactly the same as the models used to generate the data. In every case, the TME method provided better moment estimates than did the NLR method, even when an inappropriate model was applied. However, the accuracy of the TME method may be constrained by the temporal discretization between data points, or, more seriously by the presence of gaps in the measured data. Finally, while it is emphasized that the best moment estimates are obtained when the selected model exhibits features similar to those observed in the measured data (e.g., exponential extrapolation is likely to be the most accurate moment estimation approach in systems dominated by first-order processes), the lognormal distribution truncated moment approach may nonetheless be preferred for many applications because of its analytical simplicity and computational ease compared to other process-based models of solute transport.

APPENDIX C
PARAMETERS REQUIRED TO CALCULATE NAPL REMOVAL
EFFICIENCIES FOR THE COSOLVENT AND SPME FIELD STUDIES

Table C-1. Cosolvent flushing EW BTC moments and soil concentrations for selected NAPL constituents.

NAPL Constituent	Mass Fraction [a] (mg/g)	EW BTC Moments		Soil Concentrations	
		m_0 [a, b] (kg)	m_1 [b] (kL)	$\bar{X}_{pre}$ [c] (mg/kg)	$\bar{X}_{post}$ [d] (mg/kg)
DCB	0.61	0.442	5.45	34.1	3.32
1,3,5-TMB	0.083	0.128	6.74	NM	NM
n-decane	0.52	0.621	7.16	46.7	6.15
n-undecane	1.60	1.207	7.97	NM	NM

NM, not measured in the cosolvent cell. [a] From Rao et al. (1997). [b] Flux-averaged values for all three EWs. [c] $n = 64$ samples from within the flushed zone. [d] $n = 71$.

Table C-2. SPME and cosolvent soil parameters and flux-averaged EW swept volumes and NAPL saturations.

Parameter		SPME	Cosolvent
Average porosity		0.14	0.20 [b]
NAPL density	(g/cm³)	0.88	0.85
Assumed bulk density	(g/cm³)	1.7	1.7
[a] m_1^{np}	(kL)	2.01	1.77 [b]
[a] $S_{N_{pre}}$		0.061	0.054 [b]
[a] $S_{N_{post}}$		0.017	0.010 [c]

[a] Flux-averaged values for all three EWs. [b] From Annable et al. (1998). [c] From Sillan (1999). The additional parameters required for the SPME study are listed in Tables 3-2 and 3-3 (mass fractions of individual constituents in the NAPL and zeroth and first moments of constituent BTCs measured during flushing).

REFERENCES

Abbaszadeh-Dehghani, M., and W.E. Brigham, Analysis of well-to-well tracer flow to determine reservoir layering, *J. Pet. Tech.* (October), 1753-1762, 1984.

Abdul, A.S., T.L. Gibson, C.C. Ang, J.C. Smith, and R.E. Sobczynski, In-situ surfactant washing of polychlorinated biphenyls and oils from a contaminated site, *Ground Water*, *30* (2), 219-231, 1992.

Abernethy, S.G., D. Mackay, and L.S. McCarty, "Volume fraction" correlation for narcosis in aquatic organisms: The key role of partitioning, *Environmental Toxicology and Chemistry*, *7* (6), 469-481, 1988.

Abu-Dayya, A., and N.C. Beaulieu, Outage probabilities in the presence of correlated lognormal interferers, *IEEE Trans. Veh. Technol.*, *43* (1), 164-173, 1994.

Aitchison, J., and J.A.C. Brown, *The Lognormal Distribution*, Cambridge University Press, Cambridge, 1957.

Annable, M.D., J.W. Jawitz, P.S.C. Rao, D.P. Dai, H.K. Kim, and A.L. Wood, Field evaluation of interfacial and partitioning tracers for characterization of effective NAPL-water contact areas, *Ground Water*, *36* (3), 495-502, 1998a.

Annable, M.D., P.S.C. Rao, K. Hatfield, W.D. Graham, A.L. Wood, and C.G. Enfield, Partitioning tracers for measuring residual NAPL: Field-scale test results, *J. Environ. Eng.*, *124* (6), 498-503, 1998b.

Atkinson, K., *Elementary Numerical Analysis*, John Wiley & Sons, New York, 1985.

Augustijn, D.C.M., Chemodynamics of complex waste mixtures: Applications to contamination and remediation of soils and aquifer media, Ph.D. dissertation, University of Florida, Gainesville, FL, 1993.

Augustijn, D.C.M., R.E. Jessup, P.S.C. Rao, and A.L. Wood, Remediation of contaminated soils by solvent flushing, *J. Environ. Eng.*, *120* (1), 42-57, 1994.

Ballet, F., and F. Candau, Water-oil solubilization by long chain polyoxyethylene nonionic surfactants, *Coll. Polymer Sci.*, *259*, 548-552, 1981.

Baran, J.R., Jr., G.A. Pope, W.H. Wade, and V. Weerasooriya, Microemulsion formation with chlorinated hydrocarbons of differing polarity, *Environ. Sci. Technol.*, *28* (7), 1361-1366, 1994.

Barton, A.F.M., *Alcohols with Water*, Pergamon Press, New York, 1984.

Bellin, A., A. Rinaldo, W.J.P. Bosma, S.E.A.T.M. van der Zee, and Y. Rubin, Linear equilibrium adsorbing solute transport in physically and chemically heterogeneous porous formations. 1. Analytical solutions, *Water Resour. Res.*, *29* (12), 4019-4030, 1993.

Bosma, W.J.P., A. Bellin, S.E.A.T.M. van der Zee, and A. Rinaldo, Linear equilibrium adsorbing solute transport in physically and chemically heterogeneous porous formations. 2. Numerical results, *Water Resour. Res.*, *29* (12), 4031-4043, 1993.

Brandes, D., and K.J. Farley, Importance of phase behavior on the removal of residual DNAPLs from porous media by alcohol flushing., *Water Env. Res.*, *65* (7), 869-878, 1993.

Brenner, H., The diffusion of longitudinal mixing in beds of finite legnth: Numerical values, *Chem. Eng. Sci.*, *17*, 229-243, 1962.

Brusseau, M.L., R.E. Jessup, and P.S.C. Rao, Nonequilibrium sorption of organic chemicals: Elucidation of rate-limiting processes, *Environ. Sci. Technol.*, *25* (1), 134-142, 1991.

Brusseau, M.L., and P.S.C. Rao, Sorption nonideality during organic contaminant transport in porous media, *CRC Crit. Rev. Environ. Control*, *19*(1), 33-99, 1989.

Chen, W., and R.J. Wagenet, Solute transport in porous media with sorption-site heterogeneity, *Environ. Sci. Technol.*, *29* (11), 2725-2734, 1995.

Chevalier, L.R., S.J. Masten, R.B. Wallace, and D.C. Wiggert, Experimental investigation of surfactant-enhanced dissolution of residual NAPL in saturated soil, *Ground Water Monitoring and Remediation*, *17* (4), 99-107, 1997.

Consortini, A., and G. Conforti, Detector saturation effect on higher-order moments of intensity fluctuations in atmospheric laser propagation measurement, *J. Opt. Soc. Am. A*, *1* (11), 1075-1077, 1984.

Corey, A.T., *Mechanics of Immiscible Fluids in Porous Media*, Water Resources Publications, Littleton, Colorado, 1986.

Cvetkovic, V., G. Dagan, and H. Cheng, Contaminant transport in aquifers with spatially variable hydraulic and sorption properties, *Proc. R. Soc. Lond. A*, *454*, 2173-2207, 1998.

Cvetkovic, V.D., and A.M. Shapiro, Mass arrival of sorptive solute in heterogeneous porous media, *Water Resour. Res.*, *26* (9), 2057-2067, 1990.

Dagan, G., *Flow and Transport in Porous Formations*, Springer-Verlag, New York, 1989.

Dai, D., Solubility and partitioning behavior of organic compounds in complex NAPL mixtures, Ph.D. dissertation, University of Florida, Gainesville, FL, 1997.

Delay, F., G. Porel, and O. Banton, An approach to transport in heterogeneous porous media using the truncated temporal moment equations: Theory and numerical validation, *Transport in Porous Media*, *32*, 199-232, 1998.

Demmy, G., Solute transport in heterogeneous porous formations, Ph. D. dissertation, University of Florida, Gainesville, FL, 1999.

Demmy, G., S. Berglund, and W. Graham, Injection mode implications for solute transport in porous media: Analysis in a stochastic Lagrangian framework, *Water Resour. Res.*, *35* (7), 1965-1973, 1999.

Fahim, M.A., and N. Wakao, Parameter estimation from tracer response measurements, *Chem. Eng. J.*, *25*, 1-8, 1982.

Falta, R.W., S.E. Brame, C.M. Lee, J.T. Coates, C. Wright, S. Price, P. Haskell, and E. Roeder, A field test of NAPL removal by high molecular weight alcohol injection, in *Non-Aqueous Phase Liquids (NAPLs) in Subsurface Environment: Assessment and Remediation*, pp. 257-268, ASCE, Washington, D. C., 1996.

Farley, K.J., R.W. Falta, D. Brandes, J.T. Milazzo, and S.E. Brame, Remediation of hydrocarbon-contaminated groundwaters by alcohol flooding, Hazardous Waste Management Research Fund, Institute of Public Affairs, University of South Carolina, Columbia, South Carolina, 1993.

Fountain, J.C., R.C. Starr, T. Middleton, M. Beikirch, C. Taylor, and D. Hodge, A controlled field test of surfactant-enhanced aquifer remediation, *Ground Water*, *34* (5), 910-916, 1996.

Freeze, R.A., and J.A. Cherry, *Groundwater*, Prentice Hall, Englewood Cliffs, New Jersey, 1979.

Gelhar, L.W., *Stochastic Subsurface Hydrology*, Prentice Hall, Englewood Cliffs, NJ, 1993.

Grubb, D.C., and N. Sitar, Evaluation of technologies for in-situ cleanup of DNAPL contaminated sites, *EPA/600/R-94/120*, R. S. Kerr Environmental Research Laboratory, U. S. EPA, Ada, OK, 1994.

Haas, C.N., Moment analysis of tracer experiments, *J. Environ. Eng.*, *122* (12), 1121-1123, 1996.

Helms, A.D., Jr., Moment estimates for imperfect breakthrough data: Theory and application to a field-scale partitioning tracer experiment, M.E. Thesis, University of Florida, Gainesville, FL, 1997.

Helms, A.D., K. Hatfield, and W.D. Graham, Moment estimates for imperfect breakthrough data, *J. Contam. Hydrol.*, In review, 1999.

Huh, C., Interfacial tensions and solubilizing ability of a microemulsion phase that co-exists with oil and brine, *J. Colloid Interface Sci.*, *71*, 408, 1979.

Imhoff, P.T., S.N. Gleyzer, J.F. McBride, L.A. Vancho, I. Okuda, and C.T. Miller, Cosolvent-enhanced remediation of residual dense nonaqueous phase liquids: Experimental investigation, *Environ. Sci. Technol.*, *29* (8), 1966-1976, 1995.

James, A.I., W.D. Graham, K. Hatfield, P.S.C. Rao, and M.D. Annable, Optimal estimation of residual non-aqueous phase liquid saturations using partitionng concentration data, *Water Resour. Res.*, *32* (12), 2621-2636, 1997.

Jawitz, J.W., Unstable miscible displacements in unconfined porous media: Implications on the efficiency of in-situ flushing aquifer remediation, M.E. Thesis, University of Florida, Gainesville, FL, 1995.

Jawitz, J.W., M.D. Annable, and P.S.C. Rao, Miscible fluid displacement stability in unconfined porous media: Two-dimensional flow experiments and simulations, *J. Contam. Hydrol.*, *31*, 211-230, 1998a.

Jawitz, J.W., M.D. Annable, and P.S.C. Rao, Using interwell partitioning tracers and the method of moments to estimate the spatial distribution of non-aqueous phase contaminants in aquifers, in *GQ 98 Conference Proceedings, Groundwater Quality: Remediation and Protection*, pp. 422-425, IAHS Publ. no. 250, Tübingen, Germany, 1998b.

Jawitz, J.W., M.D. Annable, P.S.C. Rao, and R.D. Rhue, Field implementation of a Winsor Type I surfactant/alcohol mixture for in situ solubilization of a complex LNAPL as a single-phase microemulsion, *Environ. Sci. Technol.*, *32* (4), 523-530, 1998c.

Jawitz, J.W., M.D. Annable, R.K. Sillan, and P.S.C. Rao, In situ flushing for remediation of aquifer contaminant source zones: Evaluating performance using a control plane approach, in *Contaminated Site Remediation Conference*, pp. 455-462, Centre for Groundwater Studies, CSIRO Land and Water, Fremantle, Western Australia, 1999.

Jawitz, J.W., R.D. Rhue, M.D. Annable, and P.S.C. Rao, Laboratory and Field Evaluation of Single-Phase Microemulsions (SPME) for Enhanced In-Situ Remediation of Contaminated Aquifers, Advanced Applied Technology Demonstration Facility (AATDF) Final Report, Contract R115-D23100095, University of Florida, Gainesville, FL, November, 1997a.

Jawitz, J.W., R.K. Sillan, M.D. Annable, and P.S.C. Rao, Methods for determining NAPL source zone remediation efficiency of *in-situ* flushing technologies, in *In Situ Remediation of the Geoenvironment: Proceedings of the Conference*, edited by J.C. Evans, pp. 271-283, ASCE, Minneappolis, MN, 1997b.

Jessup, R.E., and P.S.C. Rao, UFBTC: A software package for simulation of nonreactive and reactive solute transport in homogeneous porous media during steady 1-D flow, unpublished software, Soil and Water Science Department, University of Florida, Gainesville, FL, 1990.

Jin, M., A study of nonaqueous phase liquid characterization and surfactant remediation, PhD dissertation, University of Texas at Austin, Austin, TX, 1995.

Jin, M., M. Delshad, V. Dwarakanath, D.C. McKinney, G.A. Pope, K. Sepehrnoori, C.E. Tilburg, and R.E. Jackson, Partitioning tracer tests for detection, estimation, and remediation performance assessment of subsurface nonaqueous phase liquids, *Water Resour. Res.*, *31* (5), 1201-1211, 1995.

Johnson, G.R., Solvent flushing of a LNAPL contaminated soil: Comparison of two cosolvent mixtures and the effects of weathered contamination on cosolvent flushing efficiency, M.E. thesis, University of Florida, Gainesville, FL, 1996.

Jury, W.A., Simulation of solute transport using a transfer function model, *Water Resour. Res.*, *18* (2), 363-368, 1982.

Jury, W.A., and K. Roth, *Transfer Functions and Solute Movement through Soil*, Birkhäuser Verlag, Boston, 1990.

Jury, W.A., and G. Sposito, Field calibration and validation of solute transport models for the unsaturated zone, *Soil Sci. Soc. Am. J.*, *49*, 1331-1341, 1985.

Kabala, Z.J., and G. Sposito, Statistical moments of reactive solute concentration in a heterogeneous aquifer, *Water Resour. Res.*, *30* (3), 759-768, 1991.

Kafarov, V.V., V.G. Vygon, and L.S. Gordeev, Statistical estimates of the parameters in mathematical models describing the hydrodynamic structure of flows, *Theoretical Foundations of Chemical Engineering*, *2* (2), 228-235, 1968.

Kreft, A., and A. Zuber, On the physical meaning of the dispersion equation and its solutions for different initial and boundary conditions, *Chem. Eng. Sci.*, *33*, 1471-1480, 1978.

Kueper, B.H., and E.O. Frind, Two-phase flow in heterogeneous porous media. 1. Model development, *Water Resour. Res.*, *27* (6), 1049-1057, 1991.

Lake, L.W., *Enhanced Oil Recovery*, Prentice Hall, Englewood Cliffs, New Jersey, 1989.

Lapidus, L., and N.R. Amundson, Mathematics of adsorption in beds IV. The effect of longitudinal diffusion in ion exchange chromatographic columns, *J. Phys. Chem.*, *56*, 984-988, 1952.

Luthy, R.G., D.A. Dzombak, C.A. Peters, M.A. Ali, and S.B. Roy, Solvent extraction for remediation of manufactured gas plant sites, *EPRITR-101845*, Electric Power Research Institute, Palo Alto, CA, 1992.

Martel, R., and P.J. Gélinas, Surfactant solutions developed for NAPL recovery in contaminated aquifers, *Ground Water*, *34* (1), 143-154, 1996.

Martel, R., P.J. Gélinas, J.E. Desnoyers, and A. Masson, Phase diagrams to optimize surfactant solutions for oil and DNAPL recovery in aquifers, *Ground Water*, *31* (5), 789-800, 1993.

McCray, J.E., and M.L. Brusseau, Cyclodextrin-enhanced in situ flushing of multiple-component immiscible organic liquid contamination at the field scale: Mass removal effectiveness, *Environ. Sci. Technol.*, *32* (9), 1285-1293, 1998.

Montgomery Watson Inc., Hill Air Force Base, Utah, Phase I Work Plan for Eight Treatability Studies at Operable Unit 1, Montgomery Watson, Salt Lake City, UT, 1995.

Nelson, N.T., and M.L. Brusseau, Field study of the partitioning tracer method for detection of dense nonaqueous phase liquid in a trichloroethene-contaminated aquifer, *Environ. Sci. Technol.*, *30* (9), 2859-2863, 1996.

Nkedi-Kizza, P., J.W. Biggar, H.M. Selim, M.T. van Genuchten, P.J. Wierenga, J.M. Davidson, and D.R. Nielsen, On the equivalence of two conceptual models for describing ion exchange during transport through an aggregated oxisol, *Water Resour. Res.*, *20* (8), 1123-1130, 1984.

Nkedi-Kizza, P., P.S.C. Rao, and A.G. Hornsby, Influence of organic cosolvents on sorption of hydrophobic organic chemicals by soils, *Environ. Sci. Technol.*, *19* (10), 975-979, 1985.

Nkedi-Kizza, P., P.S.C. Rao, and A.G. Hornsby, Influence of organic cosolvents on leaching of hydrophobic organic chemicals through soils, *Environ. Sci. Technol.*, *21* (11), 1107-1111, 1987.

Ouyang, Y., R.S. Mansell, and R.D. Rhue, A microemulsification approach for removing organolead and gasoline from contaminated soil, *Journal of Hazardous Materials*, *46*, 23-35, 1996.

Pennell, K.D., L.M. Abriola, and W.J. Weber, Jr., Surfactant enhanced solubilization of residual dodecane in soil columns, *Environ. Sci. Technol.*, *27*, 2332-2340, 1993.

Pennell, K.D., G.A. Pope, and L.M. Abriola, Influence of viscous and buoyancy forces on the mobilization of residual tetrachloroethylene during surfactant flushing, *Environ. Sci. Technol.*, *30* (4), 1328-1335, 1996.

Peters, C.A., and R.G. Luthy, Coal tar dissolution in water-miscible solvents: Experimental evaluation, *Environ. Sci. Technol.*, *27* (13), 2831-2843, 1993.

Pinal, R., P.S.C. Rao, L.S. Lee, P.V. Cline, and S.H. Yalkowsky, Cosolvency of partially miscible organic solvents on the solubility of hydrophobic organic chemicals, *Environ. Sci. Technol.*, *24* (5), 639-647, 1990.

Powers, S.E., L.M. Abriola, and W.J.J. Weber, An experimental investigation of nonaqueous phase liquid dissolution in saturated subsurface systems: Steady state mass transfer rates, *Water Resour. Res.*, *28* (10), 2691-2705, 1992.

Puerto, M.C., and R.L. Reed, A three-parameter representation of surfactant/oil/brine interaction, *Soc. Pet. Eng. J.*, *23*, 669-682, 1983.

Rao, P.S.C., M.D. Annable, R.K. Sillan, D. Dai, K.H. Hatfield, W.D. Graham, A.L. Wood, and C.G. Enfield, Field-scale evaluation of *in-situ* cosolvent flushing for remediation of an unconfined aquifer contaminated with a complex LNAPL, *Water Resour. Res.*, *33* (12), 2673-2686, 1997.

Rao, P.S.C., L.S. Lee, and R. Pinal, Cosolvency and sorption of hydrophobic organic chemicals, *Environ. Sci. Technol.*, *24* (5), 647-654, 1990.

Rao, P.S.C., L.S. Lee, and A.L. Wood, Solubility, sorption, and transport of hydrophobic organic chemicals in complex mixtures, *EPA/600/M-91/009*, R. S. Kerr Environmental Research Laboratory, U. S. EPA, Ada, OK, 1991.

Rhue, R.D., P.S.C. Rao, and M.D. Annable, Single-phase microemulsification of a complex light-nonaqueous phase liquid: Laboratory evaluation of several mixtures of surfactant/alcohol solutions, *J. Env. Qual.*, *28* (4), 1035-1144, 1999.

Robin, M.J.L., E.A. Sudicky, R.W. Gillham, and R.G. Kachanoski, Spatial variability of strontium distribution coefficients and their correlation with hydraulic conductivity in the Canadian Forces Base Borden aquifer, *Water Resour. Res.*, *27*, 2619-2632, 1991.

Rosen, M.J., *Surfactants and Interfacial Phenomena*, John Wiley & Sons, New York, 1989.

Sabatini, D.A., R.C. Knox, and J.H. Harwell, Surfactant-Enhanced DNAPL Remediation: Surfactant Selection, Hydraulic Efficiency, and Economic Factors, *EPA/600/S-96/002*, National Risk Management Research Laboratory, U.S. EPA, Ada, OK, 1996.

Safak, A., Statistical analysis of the power sum of multiple correlated log-normal components, *IEEE Trans. Veh. Technol.*, *42* (1), 58-61, 1993.

Sangster, J., Octanol-water partition coefficients of simple organic compounds, *J. Phys. Chem. Ref. Data*, *18* (3), 1111-1229, 1989.

Schwartz, S.C., and Y.S. Yeh, On the distribution function and moments of power sums with log-normal components, *Bell Sys. Tech. J.*, *61* (7), 1441-1462, 1982.

Schwarzenbach, R.P., P.M. Gschwend, and D.M. Imboden, *Environmental Organic Chemistry*, John Wiley & Sons, New York, 1993.

Shah, D.O., Surface Phenomena in Enhanced Oil Recovery, pp. 874, Plenum Press, New York, 1981.

Shiau, B.-J., D.A. Sabatini, J.H. Harwell, and D.Q. Vu, Microemulsion of mixed chlorinated solvents using food grade (edible) surfactants, *Environ. Sci. Technol.*, *30* (1), 97-103, 1996.

Sillan, R.K., Field-scale evaluation of in situ cosolvent flushing for enhanced aquifer remediation, Ph.D. dissertation, University of Florida, Gainesville, FL, 1999.

Sillan, R.K., M.D. Annable, P.S.C. Rao, D. Dai, K. Hatfield, W.D. Graham, A.L. Wood, and C.G. Enfield, Evaluation of in situ cosolvent flushing dynamics using a network of spatially distributed multilevel samplers, *Water Resour. Res.*, *34* (9), 2191-2202, 1998.

Soerens, T.S., D.A. Sabatini, and J.H. Harwell, Effects of flow bypassing and nonuniform NAPL distribution on the mass transfer characteristics of NAPL dissolution, *Water Resour. Res.*, *34* (7), 1657-1673, 1998.

Stedinger, J.R., Fitting log normal distributions to hydrologic data, *Water Resour. Res.*, *16* (3), 481-490, 1980.

Tompson, A.F.B., Numerical simulation of chemical migration in physically and chemically heterogeneous porous media, *Water Resour. Res.*, *29* (11), 3709-3726, 1993.

Tompson, A.F.B., R. Ababou, and L.R. Gelhar, Implementation of the three-dimensional turning bands random field generator, *Water Resour. Res.*, *25* (10), 2227-2243, 1989.

Valocchi, A.J., Validity of the local equilibrium assumption for modeling sorbing solute transport through homogeneous soils, *Water Resour. Res.*, *21* (6), 808-820, 1985.

Valocchi, A.J., Spatial moment analysis of the transport of kinetically adsorbing solutes through stratified aquifers, *Water Resour. Res.*, *25* (2), 273-279, 1989.

van Genuchten, M.T., and W.J. Alves, Analytical solutions of the one-dimensional convective-dispersive solute transport equation, *USDA-ARS Tech. Bull. 1661*, U.S. Government Printing Office, Washington, D.C., 1982.

van Genuchten, M.T., and P.J. Wierenga, Solute dispersion coefficients and retardation factors, in *Methods of Soil Analysis: Part 1 Physical and Mineralogical Methods*, edited by A. Klute, pp. 1025-1054, Soil Science Society of America, Madison, WI, 1986.

van Valkenburg, M.E., Solubilization and mobilization of perchloroethylene by cosolvents in porous media, Ph.D. dissertation, University of Florida, Gainesville, FL, 1999.

Verschueren, K., *Handbook of Environmental Data on Organic Chemicals*, Van Nostrand Reinhold, New York, 1983.

West, C.C., and J.H. Harwell, Surfactants and subsurface remediation, *Environ. Sci. Technol.*, *26* (12), 2324-2330, 1992.

Wise, W.R., NAPL characterization via partitioning tracer tests: quantifying effects of partitioning nonlinearities, *J. Contam. Hydrol.*, *36*, 167-183, 1999.

Wise, W.R., D. Dai, E.A. Fitzpatrick, L.W. Evans, P.S.C. Rao, and M.D. Annable, Non-aqueous phase liquid characterization via partitioning tracer tests: a modified Langmuir relation to describe partitioning nonlinearities, *J. Contam. Hydrol.*, *36*, 153-165, 1999.

BIOGRAPHICAL SKETCH

James William Jawitz was born in Orlando, Florida, in 1970. He grew up in North Miami Beach, Florida, and graduated from North Miami Beach Senior High in 1988. He attended the University of Florida and received a bachelor's degree with honors in environmental engineering in December 1992. In 1993 he moved to Atlanta, Georgia, and began working as a civilian environmental engineer for the United States Air Force at Dobbins Air Reserve Base. Shortly thereafter, he was awarded a fellowship from the United States Department of Energy to attend graduate school. After his brief career as a federal employee, he returned to the University of Florida to pursue a master of engineering degree in August of 1993. After graduation redux in 1995, he was enticed to stay at the University of Florida to continue toward a Ph.D. Following his third, and final, graduation from the University of Florida, he plans to remain in Gainesville as a postdoctoral fellow for at least one semester, ensuring an even dozen seasons of Gator football and a fourth, and perhaps final, year of Dr. Death intramural football.

I certify that I have read this study and that in my opinion it conforms to acceptable standards of scholarly presentation and is fully adequate, in scope and quality, as a dissertation for the degree of Doctor of Philosophy.

Michael D. Annable, Chair
Associate Professor of Environmental
Engineering Sciences

I certify that I have read this study and that in my opinion it conforms to acceptable standards of scholarly presentation and is fully adequate, in scope and quality, as a dissertation for the degree of Doctor of Philosophy.

P. Suresh C. Rao, Co-chair
Graduate Research Professor of Soil and
Water Science

I certify that I have read this study and that in my opinion it conforms to acceptable standards of scholarly presentation and is fully adequate, in scope and quality, as a dissertation for the degree of Doctor of Philosophy.

R. Dean Rhue
Professor of Soil and Water Science

I certify that I have read this study and that in my opinion it conforms to acceptable standards of scholarly presentation and is fully adequate, in scope and quality, as a dissertation for the degree of Doctor of Philosophy.

William R. Wise
Associate Professor of Environmental
Engineering Sciences

I certify that I have read this study and that in my opinion it conforms to acceptable standards of scholarly presentation and is fully adequate, in scope and quality, as a dissertation for the degree of Doctor of Philosophy.

Kirk Hatfield
Associate Professor of Civil Engineering

This dissertation was submitted to the Graduate Faculty of the College of Engineering and to the Graduate School and was accepted as partial fulfillment of the requirements for the degree of Doctor of Philosophy.

August 1999

_____
Dean, College of Engineering

_____
Dean, Graduate School